LUND UNIVERSITY

Wireless Channel Modeling and Reconstruction in Massive MIMO Systems

Fedorov, Aleksei

2019

Document Version:
Publisher's PDF, also known as Version of record

Link to publication

Citation for published version (APA):
Fedorov, A. (2019). *Wireless Channel Modeling and Reconstruction in Massive MIMO Systems*. [Doctoral Thesis (compilation), University of Otago]. Univeristy of Otago.

Total number of authors:
1

General rights
Unless other specific re-use rights are stated the following general rights apply:
Copyright and moral rights for the publications made accessible in the public portal are retained by the authors and/or other copyright owners and it is a condition of accessing publications that users recognise and abide by the legal requirements associated with these rights.
• Users may download and print one copy of any publication from the public portal for the purpose of private study or research.
• You may not further distribute the material or use it for any profit-making activity or commercial gain
• You may freely distribute the URL identifying the publication in the public portal

Read more about Creative commons licenses: https://creativecommons.org/licenses/

Take down policy
If you believe that this document breaches copyright please contact us providing details, and we will remove access to the work immediately and investigate your claim.

LUND UNIVERSITY

PO Box 117
221 00 Lund
+46 46-222 00 00

Wireless Channel Modeling and Reconstruction in Massive MIMO Systems

Aleksei Fedorov

a thesis submitted for the degree of

Doctor of Philosophy

at the University of Otago, Dunedin,

New Zealand.

30 January 2019

Ийэбэр

Abstract

The past few years have witnessed dramatic growth in the number of wirelessly connected devices, which will continue to increase in the future. Following this trend, the capacity of the wireless networks has been enhanced to provide high-quality service to tens of billions of devices. At the same time, in response to the network enhancement, each device unashamedly requests more and more throughput to support high-data-consuming applications such as video calls, high-definition video streaming, and online multiplayer video games. This undoubtedly indicates that the demand for high wireless throughput and numerous new connections will keep increasing in the near future. In addition, the development of new technologies such as virtual/augmented reality, self-driving cars, remote surgery, and other latency-critical applications has caused concern regarding the network response latency. Thus, next-generation wireless networks have to satisfy three main requirements: i) high throughput; ii) simultaneous service to many users; and iii) low latency. Massive multiple-input multiple-output (MIMO) technology, where a base station (BS) equipped with a large antenna array is capable of serving many users simultaneously in the same time-frequency domain, has been developed to mitigate these requirements except the last. However, massive MIMO technology has to overcome the challenges related to the channel estimation (CE) overhead, which inevitably increases the communication latency, to become the absolute leader in the list of promising technologies for next-generation wireless communication. This dissertation focuses on developing solutions that are aimed to mitigate massive MIMO CE challenges. The dissertation consists of three main parts: massive MIMO channel modeling, user localization in massive MIMO networks, and full downlink channel reconstruction.

The first part (Chapter 3) discusses an approach for modeling spatially consistent channels in massive MIMO networks. The main focus is put on

describing specular reflections of wireless signals from arbitrarily inclined surfaces by taking into account the signals' polarizations and the spatial distributions of massive MIMO antennas. The proposed approach has been validated through simulating signal transmissions in a realistic environment model based on Google Maps. Results show the importance of incorporating a spherical wave propagation model and the consideration of detailed 3D characteristics of the surroundings in the simulation of massive MIMO channels.

The second part (Chapter 4) introduces a solution for localizing users in massive MIMO networks. The main focus is on designing algorithms that are capable of estimating the positions of users using only uplink signals by exploring the advantages of the spherical wave propagation model proposed in the first section. The designed localization schemes have been evaluated through both simulation and proof-of-concept experiments. Simulation results show that the schemes can achieve decimeter-level localization accuracy using 64 and more antenna elements for distances up to 300 meters. The proof-of-concept experiment justifies the feasibility of user localization based on the estimation of the spherical shape of the incoming wavefront.

The third part (Chapter 5) investigates the problem of reconstructing the full downlink channel from incomplete uplink channel measurements in massive MIMO systems. This problem arises in the next-generation networks, where connected devices have multiple transmitting and non-transmitting antennas. To achieve high throughput, channels for non-transmitting antennas have to be reconstructed. This section presents ARDI, a scheme that builds a bridge between the radio channel and physical signal propagation environment to link spatial information about the non-transmitting antennas with their radio channels. By inferring locations and orientations of the non-transmitting antennas from an incomplete set of uplink channels, ARDI can reconstruct the downlink channels for non-transmitting antennas. The performance evaluation results demonstrate that ARDI is capable of accurately reconstructing full downlink channels when the signal-to-noise ratio is higher than 15dB, thereby expanding the channel capacity of massive MIMO networks.

Acknowledgements

First of all, I would like to thank my supervisors – Dr. Haibo Zhang and Dr. Yawen Chen – for their professional guidance, encouragement and comprehensive supervision, which they have provided throughout my time as a student. It was an honour to be their student. I'm grateful to Dr. Haibo Zhang for his constructive suggestions and constant availability, even on weekends and on holidays, which were vital for the completion of the papers presented in this thesis.

I would like to thank all members of Computer Science department, especially Dr. Andrew Trotman, Dr. Zhiyi Huang, Dr. David Eyers, and Dr. Alistair Knott who were kind in sharing their time and discussing my ideas and oral presentations; PhD and Master's students Feiyang Liu, Rassoul Mesbah, Abbas Arghavani, Shenghuan Zhang, Johnny Flame Lee for their support and friendship. I want to thank Dr. Paul Crane for helping me with proofreading my papers and thesis.

I also thank people who were not part of the Computer Science Department but who helped me out with technical and theoretical issues, including Aubrey Miller from the School of Surveying, and Prof. Colin Fox and Dr Tim Molteno from the Department of Physics.

I would like to express my sincere gratitude to Prof. Lev Rappoport, and Dr Vladimir Lyashev for their valuable advice, productive discussions and suggestions.

I'm very thankful to my family for their continued support, patience, and encouragement. I thank my mother for her great patience and understanding when I was so far away from her. Especially, I would love to thank my wife, Galina, for her unconditional support, love, and encouragement, and who had to listen and discuss my research ideas with me on those late evenings. I thank my children for giving me motivation. Without my family, I would not have come this far.

I would like to thank my wonderful and generous friends without whom my fruitful journey to New Zealand would not have been possible: Alexandr Artemiev, Vladimir Cheremisin, Alexandr Sidorenko, Dr. Broneslav Kiselman, Dr. Dmitriy Minenkov, Dr. Andrey Fedchun, Prof. Anatoly Vershinin, Dr. Anton Andreev, and Vladislav Permyakov.

Finally, I would like to thank the University of Otago, not only for providing the scholarship that allowed me to undertake this research, but also for giving me the opportunity to attend international conferences and for providing such useful information and support services for students.

Colophon

Parts of the work presented in this thesis have already appeared in peer reviewed publications:

- A. Fedorov, H. Zhang, Y. Chen (2017). "Geometry-based modeling and simulation of 3D multipath propagation channel with realistic spatial characteristics". In *IEEE International Conference on Communications (ICC)*, Paris, pp. 1-6. doi: 10.1109/ICC.2017.7997381
- A. Fedorov, H. Zhang, Y. Chen (2018), "User Localization Using Random Access Channel Signals in LTE Networks with Massive MIMO". In *27th International Conference on Computer Communication and Networks (ICCCN)*, Hangzhou, pp. 1-9. doi: 10.1109/ICCCN.2018.8487359
- A. Fedorov, H. Zhang, G. Sidorenko, B. Yang (2019), "Full Downlink Channel Reconstruction using Incomplete Uplink Channel Measurements in Massive MIMO networks". In *18th International IFIP TC6 Networking Conference*, Warsaw, pp. 1-9. doi: 10.23919/IFIPNetworking.2019.comingsoon

Contents

1 Introduction **1**

1.1 Evolution of Cellular Mobile Wireless Networks 3
1.2 Wireless Communication Channels 4
1.3 Approaches to Enhance Channel Capacity 6
1.3.1 Expansion of the Bandwidth 7
1.3.2 Magnifying the Transmission Power 7
1.3.3 Reduction of Interference 8
1.4 Massive MIMO Technology 8
1.5 Channel Estimation and its Challenges in Massive MIMO 11
1.5.1 Channel Estimation in Multi-Antenna Systems 11
1.5.2 Downlink Channel Feedback 14
1.5.3 Channel Reciprocity 15
1.5.4 Channel Prediction 16
1.5.5 Channel Reconstruction 17
1.5.6 Channel Scarcity in Next-Generation Communication 18
1.5.7 Summary on Channel Estimation 20
1.6 Research Problems and Contributions 20
1.7 Thesis Structure 25

2 Background and Literature Review **27**

2.1 Evolution of Wireless Communication Theory 27
2.1.1 Stochastic Channel Models:
Why Channel Estimation Became a Bottleneck 29
2.2 Channel Models for Next-Generation Networks 32
2.2.1 Cluster-Based Channel Models 32
2.2.2 Geometry Based Channels Models 33
2.2.3 Summary on Channel Models 34
2.3 Transition to Deterministic Channel Paradigm 37
2.4 Channel Inference in Massive MIMO Networks 38
2.4.1 Estimation of Directions of Arrival 40
2.4.2 Estimation of Multipath Propagation Components 41
2.4.3 Estimation of Location 44
2.4.4 Estimation of Antenna Orientation 45
2.5 Summary 47

3 Channel Modeling **49**
3.1 Introduction . . . 49
3.2 Specular Reflection of a Signal from an Arbitrary Inclined Surface . . . 51
3.2.1 Reflection from an Arbitrary Plane . . . 52
3.2.2 Perpendicular and Parallel Components of Polarization . . . 55
3.2.3 Extension to a Rough Surface . . . 57
3.3 Simulation of massive MIMO Reception . . . 57
3.3.1 Sorting Antenna Elements . . . 59
3.3.2 Calculation of Time Differences . . . 59
3.3.3 Spherical Wave Propagation . . . 60
3.4 Simulations . . . 60
3.4.1 Simulation Setup . . . 61
3.4.2 Simulation Results . . . 64
3.5 Conclusion . . . 68

4 User Localization **69**
4.1 Introduction . . . 69
4.2 Background on LTE RACH Synchronization . . . 71
4.3 SWP-Based Channel Modeling . . . 73
4.4 Localization for the Single LoS Path Case . . . 75
4.4.1 Phase Estimation . . . 75
4.4.2 LoS Localization During RACH Synchronization . . . 79
4.4.3 Combating with Phase Noise . . . 80
4.4.4 Eliminating Carrier Frequency Offset and Initial Phase Offset . 82
4.5 Localization for the Multipath Case . . . 84
4.5.1 Channel Model in Frequency Domain . . . 85
4.5.2 RACH OFDM Measurements . . . 87
4.5.3 Localization as an Optimization Problem . . . 88
4.6 Performance Evaluation . . . 89
4.6.1 Simulation Setup . . . 89
4.6.2 Simulation Results . . . 90
4.6.3 Proof-of-Concept Experiment . . . 94
4.7 Conclusion . . . 96

5 Downlink Channel Reconstruction **97**
5.1 Introduction . . . 98
5.2 Overview of ARDI . . . 100
5.3 Antenna Orientation Reconstruction . . . 102
5.3.1 Single-Path LoS Case . . . 103
5.3.2 Multi-Path Case . . . 108
5.3.3 Constrained Least Square Method . . . 111
5.4 UE Orientation Reconstruction . . . 113
5.4.1 Recovery of the Global Orientations and Locations of M Antennas 116
5.5 Full Downlink Channel Reconstruction . . . 117
5.5.1 Channel Modeling . . . 117
5.5.2 Parameter Estimation for Transmitting Antennas . . . 119

5.5.3 Parameter Estimation for Non-transmitting Antennas 120
5.5.4 Feasibility for FDD and TDD Modes 122
5.6 Performance Evaluation 122
5.6.1 Simulation Setup 122
5.6.2 Results on Antenna Orientation Reconstruction 124
5.6.3 Results on Full Downlink Channel Reconstruction 125
5.7 Conclusion 128

6 Conclusion and Future Work **129**
6.1 Conclusion 129
6.2 Limitations 131
6.3 Future Work 132
6.4 Final Words 132

Bibliography **133**

List of Tables

2.1 Comparison of different channel models. SC - Stochastic Channel, GC - Geometry based Channel 36

List of Figures

1.1 Demand for Internet traffic by device type. (Cisco, 2018) 2
1.2 Connection growth by devices. (Cisco, 2018) 2
1.3 Wireless communication channel. 4
1.4 A conventional cellular network with a number of cells. Each base station services a certain cell (Björnson *et al.*, 2017). 6
1.5 The signal strength in different directions in dB. (a) Single antenna transmission; the signal is omnidirectionally transmitted by creating interference in all directions. (b) Conventional MIMO system with eight antennas; a wide signal beam is formed and directed towards the UE, but significant side lobes create substantial interference in specific directions. (c) Massive MIMO system with 32 antennas; the signal beam is narrower than in the conventional MIMO system, but small interference is still leaking out to the sides. (d) Massive MIMO system with 128 antennas; the beam is very narrow like a directed laser beam, and interference in other directions become insignificant. 9
1.6 The ability of massive MIMO to create a number of non-interfering beams towards users. (a) 32-antenna massive MIMO creates wider beams that allow simultaneous servicing of fewer users than with (b) 128-antenna massive MIMO (Flordelis *et al.*, 2015). Note, the total amount of power is the same as for the single antenna transmission. . . 10
1.7 Multi-antenna system. 12
1.8 Definition of uplink and downlink signals. 13
1.9 Time, frequency, and code division domains. 15
1.10 Definition of time division duplex and frequency division duplex modes. 16
1.11 Layout of the thesis and the relationship between different parts. The intersections of the Background with the four contributions indicate how much the topics have been studied by other researchers (in my personal opinion). 26

2.1 Difference between plane wave propagation and spherical wave propagation assumptions: all paths from UE antenna to BS antenna elements cover the same distance with the same angle of arrival in (a), but cover different distances and have different angles of arrivals in (b). 29
2.2 The Gate of Europe in Madrid of Spain are twin inclined office buildings. During propagation, the signals between BS and UE are reflected by the twin office buildings. 33

2.3 Disadvantages of MUSIC- and ESPRIT-like methods in determination of directions of arrival. (a) Consider two signal paths emerging from 102° and 84° as shown. (b) Depicts the signal components of individual paths across direction of arrival. (c) Power profile is constructed based on uplink frequencies. (d) Power profile is constructed based on downlink frequencies. 40
2.4 OFDM signal. Orthogonal subcarriers can be shared among up to four users, or can be used by one user. Flexible resource allocation. 42
2.5 Definition of UE's orientation relative to the global coordinate system O_G. Red arrows indicate transmitting antennas, orange arrows indicate non-transmitting antennas. 46

3.1 The effect of deep fading when the reflected copies of the signal in superposition give a strongly attenuated signal regardless the power of the transmitted signal. The inclination of the wall changes the reflected path. 51
3.2 Illustration of the Law of Reflection. 52
3.3 (a) Reflection of the signal inside the plane S_2. (b) Polarization changes according to the observed direction $\boldsymbol{e}_r$. 54
3.4 Spherical coordinates relative to the antenna coordinate system. 56
3.5 Close range observation of the Gates of Europe. The walls of the buildings are not ideally flat. The roughness effect has to be considered in channel generation. 58
3.6 (a) The geometry of an antenna array. (b) Calculation of time delays according to the receiving sequence. 59
3.7 The model of the Gate of Europe. The solid line is the LoS, and the dash-doted lines represent reflections from inclined walls. 62
3.8 The considered three scenario with different angles of inclination. . . . 63
3.9 The impact of orientations of communicating antennas; different types of waves, and different number of antenna elements at the BS. Orientation $\boldsymbol{p}_{\mathrm{UE}}$ has three states: vertical, horizontal, and 45°. The number of the BS's antenna elements varies between 4, 16 and 100 elements with all elements having a vertical orientation. 66
3.10 The impact of the number of antenna elements and different types of wave propagation models in the Gate of Europe scenario. The BS has vertically oriented antennas, and the UE has 45° antenna inclination. The number of antenna elements varies between 4, 16 and 100. 67

4.1 Procedure of RACH synchronization. 72
4.2 RACH signal generation. 72
4.3 RACH signal reception. 73
4.4 Communication between a UE and an LTE BS with massive MIMO. . 74
4.5 Illustration of signal shifting in continuous and discrete time domains. . 75
4.6 The results of RACH synchronization are depicted for three antenna elements in 3D and in a complex plane. The correlation spikes define phase shifts, which can be measured according to Eqn. (4.7). 77
4.7 Phase shift at different antenna elements. 78

4.8 Phase shifts at antenna elements alongside the antenna array. 79
4.9 The massive MIMO hardware. 80
4.10 (a) Histogram of the measured phase noise; (b) Power spectral density of the measured phase noise. 81
4.11 Reception of a multipath signal, S_1 and S_2 are the location search areas. 85
4.12 Single-path: RMS of the localization error for the Bancroft (BC) and refined (FK) results. 91
4.13 Single-path: RMS of the AoA estimation error for the Bancroft (BC) and refined (FK) results. 91
4.14 Multipath: RMS of multipath localization error. 93
4.15 The Otago University Massive MIMO testbed that is capable of emulating simultaneous reception of up to 16 antennas. Yellow dots on the right side indicate the positions of MIMO antenna elements, on the left side indicate positions of the UE. 94
4.16 Experimental results: sorted phases obtained from the RACH synchronization procedure. 95
4.17 Experimental results: the estimation of two locations with different number of antenna elements. 96

5.1 (a) The impact of the mutual orientations of the transmitting antenna (T_x) and the receiving antenna (R_x) on the channel. (b) Reconstructing the full channel by inferring propagation parameters and orientations in ARDI. 99
5.2 The BS is observing channels $|\mathbf{H_1}|$ and $|\mathbf{H_2}|$ from the two transmitting antennas depicted in red. Using the observation, ARDI links the propagation environment with the channel and becomes capable of inferring channels for non-transmitting antennas depicted in orange. 101
5.3 Communication between a UE and a BS. 101
5.4 Steps for reconstructing the full downlink channel. 102
5.5 Definition of the effective lengths and the electric field projections. . . . 103
5.6 Definition of projections $\boldsymbol{p}_r$ and $\boldsymbol{p}_\theta$ to $\boldsymbol{e}_r^{tx}$ and $\boldsymbol{e}_\theta^{tx}$, respectively. 106
5.7 Definition of vectors in the case of reflection. 109
5.8 The orientation of a UE in the global coordinate system O_G. 113
5.9 (a) Derivation of the reflection plane from a transmitting antenna location and its image location. (b) Mobility of UE, its antennas' orientation and location. 120
5.10 Example with estimated and inferred channels for a user equipment with four antennas two of them are transmitting in the LTE TDD transmission mode. 121
5.11 Simulation environment for signal propagation. 123
5.12 Accuracy of the antenna orientation estimation. 125
5.13 CDF of the antenna orientation estimation. 126
5.14 Accuracy of the DL channel reconstruction. 127

6.1 Channel and environment domains. Notations are taken from Chapter 5. 130

Chapter 1

Introduction

Wireless technologies have significantly enhanced human capabilities. Smart phones influence every aspect of our daily lives: from finding our location in remote parts of the planet through to real-time communication with friends on the other side of the world. Smartphones have become indispensable. With the help of wireless health monitoring devices, doctors can follow the health conditions of their patients while they are not even in the hospital area. Parents can track the breathing of their children using technology that can count the breathing rate based on radio waves propagation (Adib *et al.*, 2015). Rescuers can delegate dangerous missions to robots that are wirelessly controlled, and so avoid injury.

In recent years, data traffic (both mobile and fixed) has grown exponentially due to the dramatic growth of smartphones, tablets, laptops, and many other wireless data-consuming devices. The demand for wireless data traffic will continue to grow in the future, primarily due to emerging mobile video services and the global penetration of high throughput networks for smartphones, such as long term evolution (LTE) and LTE-Advanced (Cisco, 2018; Qualcomm, 2013; Ericsson, 2016). Figure 1.1 shows the global Internet traffic growth by devices, which indicates that the increase of smartphone data traffic alone will be more than sevenfold between 2017 and 2022, and will reach 175 exabytes (EB) per month by 2022. The traffic from wireless and mobile devices will account for 71 % of the total data traffic. The majority of the Internet content will be generated by high-definition real-time video streaming from smartphones, which means that networks should provide not only high-volume traffic but also high throughput. The demand for high-throughput traffic adds a tremendous load to the wireless network.

From the other side, there is an emerging high load that comes from the demand for

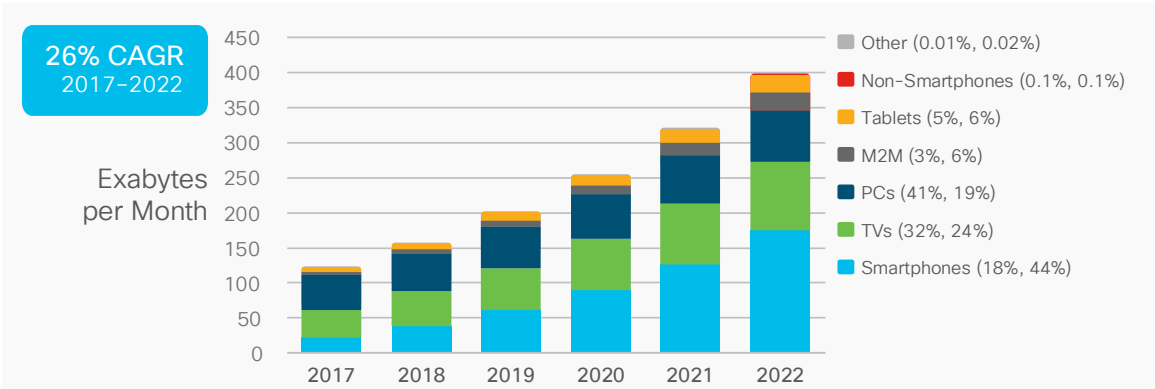

Figure 1.1: Demand for Internet traffic by device type. (Cisco, 2018)

connections of an even higher number of machine-type devices. This trend is caused by the development of the Internet-of-things (IoT) that connects devices such as home appliances, industrial robots, and other infrastructural devices to the Internet. The overall number of connected devices will be more than three times the global population by 2022, but half of this number will be occupied by machine-to-machine (M2M) connections as illustrated in Figure 1.2. There will be 14.6 billion M2M connections by 2022. The global M2M traffic will grow more than sevenfold, from 3.7 EB per month in 2017 (3 % of global traffic) to more than 25 EB by 2022 (6 % of global traffic). The amount of traffic will be growing faster than the number of connections because of the increase in deployment of video applications on M2M connections and the increased use of applications, such as telemedicine, video surveillance, and smart-car navigation systems, which require higher throughput connection with lower latency.

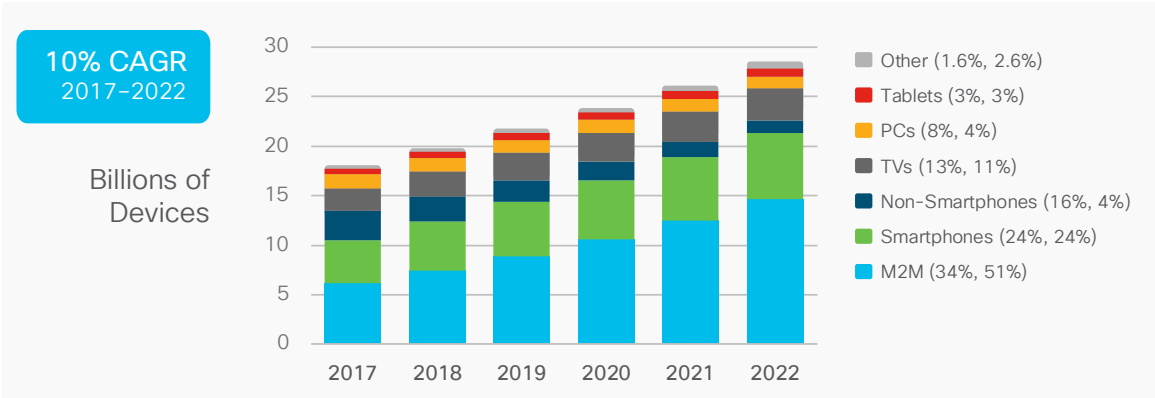

Figure 1.2: Connection growth by devices. (Cisco, 2018)

Meeting the growing demand for more connections and higher throughput requires the development of new technologies and solutions. This thesis focuses on developing

efficient solutions to improve the throughput and reduce the delay of wireless communication.

1.1 Evolution of Cellular Mobile Wireless Networks

Wireless communication systems became an integral part of our lives especially during the last two decades. Currently, we are moving from 4G or the fourth generation wireless communication systems to 5G wireless communication systems. So, the focus of the thesis is in advancing 4G networks to make 5G networks possible. Any improvement in 4G can be considered as a contribution to 5G.

Wireless communication started its extensive penetration of the consumer market approximately in the mid-1990s depending on the country. The first widely used generation was 2G. It began its market penetration at the beginning of the 1990s and quickly earned the confidence of customers, and so enabled the future development of wireless communication technology. 2G was mainly aimed at providing voice communication wirelessly with an approximate data rate of 100 kbps.

Consumers quickly understood that wireless communication is convenient not only for phone calls but also for browsing the Internet, and thus, a demand for high throughput wireless communication occurred. The market pushed telecom operators to transition to the next-generation of communication. This third generation communication took its place a little while after the start of 2G. The first deployment of 3G networks started in Japan in 1998. In addition to voice communication, the primary aim of 3G was Internet surfing with an approximate data rate of 10 Mbps.

Consumers wanted to have not only voice calls and Internet browsing but also video calls and online gaming. The demand for higher throughput pushed the development of wireless communication technology further. Around 2009, the fourth generation communication or LTE started its market penetration. Currently, it is the most used wireless communication standard. The main focus of 4G is in consumer entertainment such as video and online gaming services. The published approximate data rate is 100 Mbps.

The 4G wireless systems gave an excellent platform for the development of the paradigm of "smart" things such as "smart" toasters, "smart" watches, "smart" cars, and other "smart" things like rescue and surgical robots. The key idea of the paradigm is to connect everything to the network wirelessly and to control it, whether manually, automatically, or "smartly" with the help of artificial intelligence. In the case of com-

paratively simple things such as toaster or watches, 4G is capable of supporting the "smart" paradigm. However, 4G cannot satisfy the requirements for mission-critical applications such as self-driving cars, remote surgery, or virtual/augmented reality. These new applications form new requirements for the next generation of 5G communication.

The 5G wireless communication standard poses many new challenging tasks for engineers and scientists. The data rate has to be increased ten times, reaching 1 Gbps; the latency has to be reduced ten times from 50 milliseconds in 4G to 5 milliseconds in 5G; the network coverage has to be almost everywhere on Earth, and so on. Although the development of 5G is still at the exploratory stage, several key physical layer technologies can be highlighted as promising in enabling the increase of throughput: massive MIMO (Björnson *et al.*, 2017) and millimeter wave technology (Rappaport *et al.*, 2015).

1.2 Wireless Communication Channels

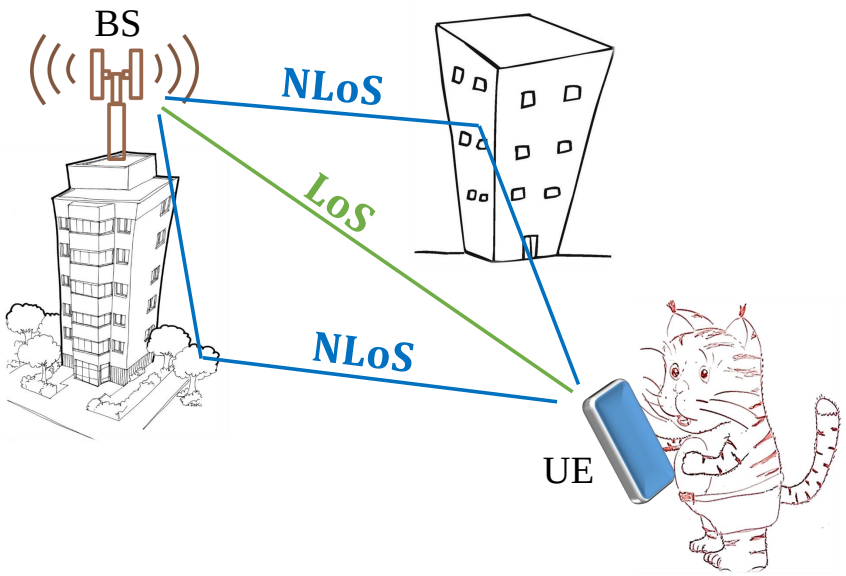

Figure 1.3: Wireless communication channel.

As illustrated in Figure 1.3, a wireless communication system typically contains a base station (BS) transmitting to a user equipment (UE) that can be a cell phone, smartphone, laptop, smart vehicle, or another connected device. To increase the network's coverage, a BS is usually mounted in a very high position like a tall tower or building. The UE and BS communicate wirelessly via electromagnetic signals (waves modulated by frequency, amplitude or phase). However, unlike traditional wired line

communication systems where electrical signals propagate on a wire, in wireless communication systems the radio environment is "open". In addition to the direct line-of-sight (LoS) propagation, there are also several retarded non-line-of-sight (NLoS) copies of the signal that arise in the environment, as illustrated in Figure 1.3. These copies arise due to the interaction of electromagnetic waves with different objects of the propagation environment such as buildings, landscapes, trees, cars, and other moving objects. The copies arrive at the BS not just via a single path but via multiple paths. Hence, such complex propagation is known as multipath propagation through an environment. The copies are known as NLoS paths.

Overall, the wireless propagation environment is very different from the wired propagation environment because in addition to the direct LoS path between the BS and UE there are many paths that are caused by different electromagnetic phenomena such as reflection, scattering, diffraction, and refraction. Each electromagnetic wave that arrives at the UE antenna, covering different distances, is subject to attenuation because of interaction with the environment. Since the distances are different, the delays are different, which means that the phases of the waves arriving at the UE are different. Multipath propagation can result in both constructive or destructive interference due to the different attenuation and signal delays experienced at the UE side. Constructive interference is where two signals add together to produce a stronger signal; conversely, destructive interference is where the signals add together and produce a weaker signal (and possibly reduce it to zero).

In addition to the interference caused by multiple paths, there is also interference from other sources such as other wireless communication devices, including neighbouring BSs. The interference from external devices (where the devices do not belong to the network) can be considered as additional background noise since the network has no idea about their origin and cannot control them. On the other hand, the interference from cellular BSs has a known pattern and, more importantly, is to some extent controllable. With "smart" resource scheduling, the network can minimize the interference from other BSs. However, the cellular BSs operate at relatively close frequency bands and inevitably create energy leakage to neighbouring bands, which is treated as inter-cell interference. Depending on the conditions, the interference can significantly degrade the capacity of the wireless channel. For example, as illustrated in Figure 1.4, the edge UEs suffer more from such inter-cell interference because the signal reception from the servicing BS can be weaker than from the neighbouring BS.

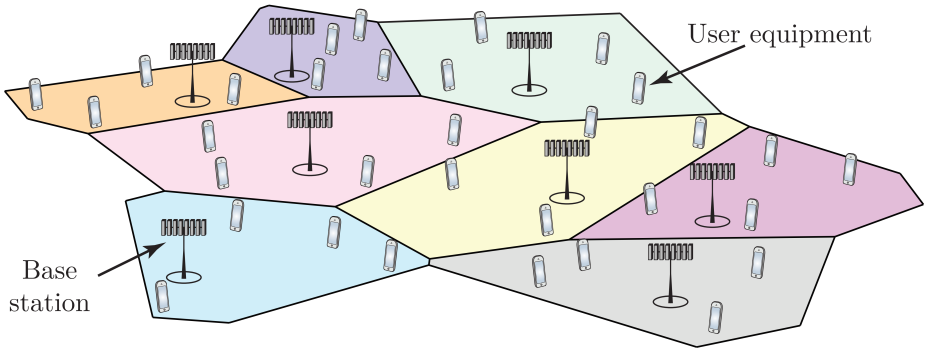

Figure 1.4: A conventional cellular network with a number of cells. Each base station services a certain cell (Björnson *et al.*, 2017).

1.3 Approaches to Enhance Channel Capacity

Since the primary aim of a wireless channel is to provide communication, the main characteristic of a wireless channel is its capacity C, which indicates how much information, in bits per second, can be transmitted through the channel (Shannon, 1948). The channel capacity shows the theoretical upper bound of the throughput at which information can be reliably transmitted through the given channel. In other words, if the signal's data rate is smaller or equal to the theoretically achievable throughput, then the receiver can decode the signal with an arbitrarily low error probability, provided that the length of the signal tends to infinity. Hence, the channel capacity indicates how much throughput can be gained from the given channel.

The demand for newer communication technology can be narrowed down to the request for higher throughput because a higher throughput enables new applications for entertainment and professional services, and opens opportunities for other new wireless-based technologies (Figures 1.1 and 1.2). Consequently, it is worth designing solutions that enable channel capacity enhancement. In the case of interference from other sources, the channel capacity can be lower bounded as follows (Björnson *et al.*, 2017):

$$C \geq B \log_2 \left(1 + \frac{p_s |h|^2}{p_v + \sigma^2}\right) \text{[bit/s/user]} \tag{1.1}$$

where B is the bandwidth, and p_s is the power of the transmitted signal, h is the channel response coefficient, p_v is the interference power, and σ^2 is the variance of the receiver noise.

From Eqn. (1.1), it is clear that the channel capacity, and consequently the through-

put, can be increased by expansion of the bandwidth B, or increasing the transmission power p_s, or by reduction of interference p_v. Most likely, all three ways of increasing the throughput will be implemented in 5G communication. We assume that we cannot influence the receiver's thermal noise σ^2, since it is defined by a user's hardware, which is different for different UEs. Therefore σ^2 represents an average noise variance relative to which the network's throughput is analyzed.

1.3.1 Expansion of the Bandwidth

The bandwidth B can be expanded by moving to higher frequencies up to visible light ranges known as millimeter wavelength (mmWave) ranges (Emerson, 1997). For example, to improve the throughput, LTE has also moved to LTE-Advanced and increased the bandwidth from 20 MHz up to 100 MHz (Sesia *et al.*, 2011). In the same way, in 5G, a significant bandwidth expansion is expected in the transition to mmWave bands technology (e.g., range from 30–300 GHz) (Heath *et al.*, 2016; Rappaport *et al.*, 2015). In mmWave, the bandwidth is expected to be around 500 MHz to 2000 MHz. The move to mmWave technology, in general, reduces the communication range due to the high attenuation properties of millimeter-wavelength electromagnetic waves, but smart use of directed antennas or steerable antenna arrays help to overcome the attenuation problems (Rappaport *et al.*, 2013). However, due to unsophisticated mmWave hardware, any further increase of the bandwidth is considered an open question at present, which again limits further improvement of the throughput.

1.3.2 Magnifying the Transmission Power

According to the International Commission on Non-Ionizing Radiation Protection, the power of transmission cannot be increased above than 4 watts/kg (ICNIRP, 2018). However, there are many emerging health-related organizations that are concerned with wireless radiation (Hardell, 2017). This trend indicates a further reduction of emission in future wireless communication networks. Hence, future wireless communication networks will not be able to increase their transmission power to achieve higher throughput. It is therefore not feasible to anticipate an increase of throughput via a power increase. An alternative is to increase the reception power $p_s|h|^2$ by making networks denser through adding more BSs. Increasing the network density makes the distances between the BSs and the users shorter, and hence the signals experience less attenuation, which increases the reception power without magnifying the transmission

power. The densification of networks is considered one of the promising directions in 5G to increase network throughput. Together with the mmWave technology, which well suits the idea of network densification due to high attenuation of signals, these two approaches will likely increase the density of the future networks. Soon, regardless of the mmWave technology implementation, the distances between BSs will be down to several dozens of meters, while at present, there are several hundreds of meters between BSs in dense urban areas (Björnson *et al.*, 2017; Fedorov *et al.*, 2018). However, excessive densification may lead to an increase of inter-cell interference p_v. This factor will limit the process of densification at some point, meaning that alternative ways of throughput enhancement have to be developed.

1.3.3 Reduction of Interference

Densification of networks and expansion of bandwidth have historically dominated the development of networks for a long time. With present technology, these solutions seem to be approaching a saturation point where any improvement is increasingly complicated and expensive. Nonetheless, both approaches can incorporate multi-antenna systems for both UEs and BSs. There is scope for the reduction of interference by exploiting multi-antenna systems, known as multiple-input and multiple-output (MIMO) antenna systems, and massive MIMO systems if the antenna arrays consist of a large number of antennas (more than 32). The use of multi-antenna systems decreases the interference due to the virtue of beamforming and spatial multiplexing techniques. Since the addition of antennas does not rely on the technology, massive MIMO systems can be immediately used in the BSs that are already in place. The next section shows why Massive MIMO is considered the most promising technology for inter-cell interference reduction in future cellular networks.

1.4 Massive MIMO Technology

In massive MIMO systems, an antenna array with individually controlled antennas can dynamically direct signals in a required direction (Veen and Buckley, 1988; Swales *et al.*, 1990; Lorenz and Boyd, 2005). This is one of the primary features of massive MIMO systems, which is called beamforming, allows reducing interference p_v in Eqn. (1.1). The further examples in Figure 1.5 and Figure 1.6 show the advantages of the beamforming technique in massive MIMO systems. The figures have been plotted in Matlab and represent the strength of the delivered signal depending on the position

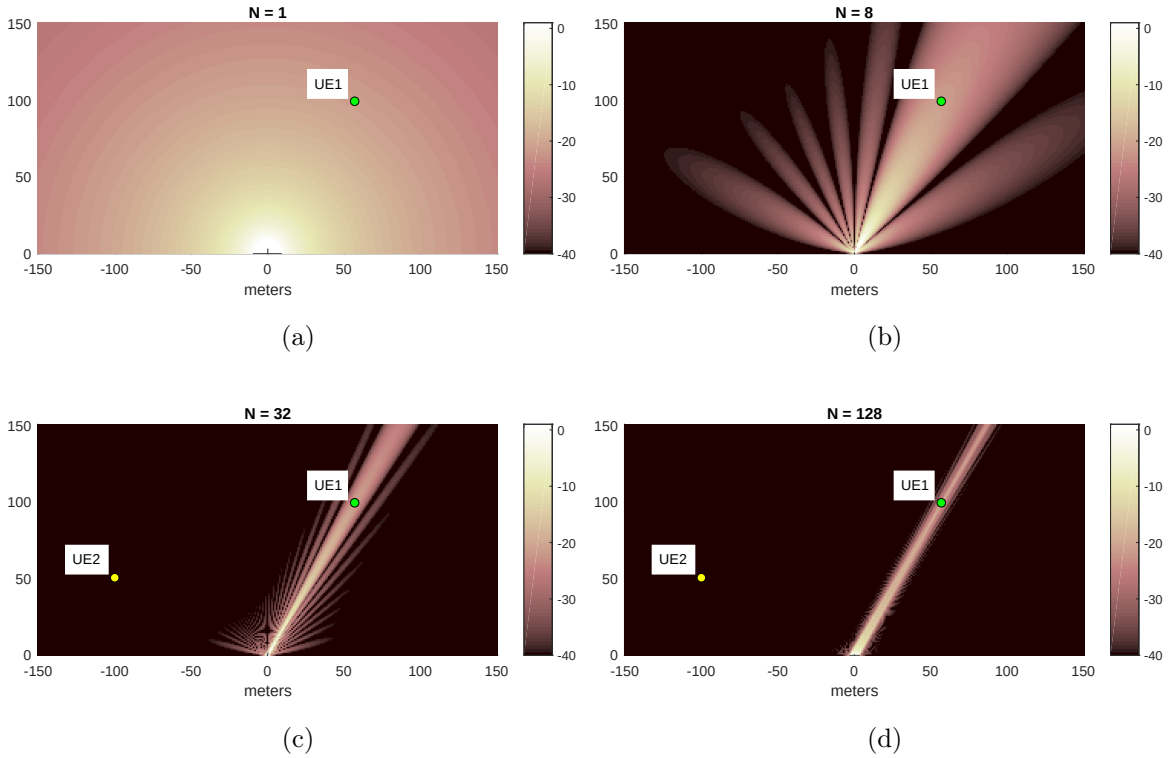

Figure 1.5: The signal strength in different directions in dB. (a) Single antenna transmission; the signal is omnidirectionally transmitted by creating interference in all directions. (b) Conventional MIMO system with eight antennas; a wide signal beam is formed and directed towards the UE, but significant side lobes create substantial interference in specific directions. (c) Massive MIMO system with 32 antennas; the signal beam is narrower than in the conventional MIMO system, but small interference is still leaking out to the sides. (d) Massive MIMO system with 128 antennas; the beam is very narrow like a directed laser beam, and interference in other directions become insignificant.

The beams are steered towards the UEs based on their angles relative to the BS (Veen and Buckley, 1988). As illustrated in Figure 1.5 (a), to deliver a signal to the UE, a single omnidirectional antenna BS emits the signal equally in all directions, which creates substantial interference in the neighbouring cells, especially in the case of dense networks. Conventional MIMO systems reduce the interference, as illustrated in Figure 1.5 (b), but the problem of these systems is the existence of significant side-lobes where signal power is still considerable (Keysight, 2016), and if another user from a neighbouring cell gets into a side lobe region, then the interference increases for this user. To make side lobes weaker, more antennas should be added. Thus, in the case of

32 antennas, side lobes becomes even smaller, but with 128 antennas the effect of side lobes are almost negligible, as illustrated in Figure 1.5 (c,d). Note, that overall transmission power stays the same for any number of antennas. The throughput increase is earned not from a transmission power increase but via the reduction in interference: all the power is concentrated in a narrow beam.

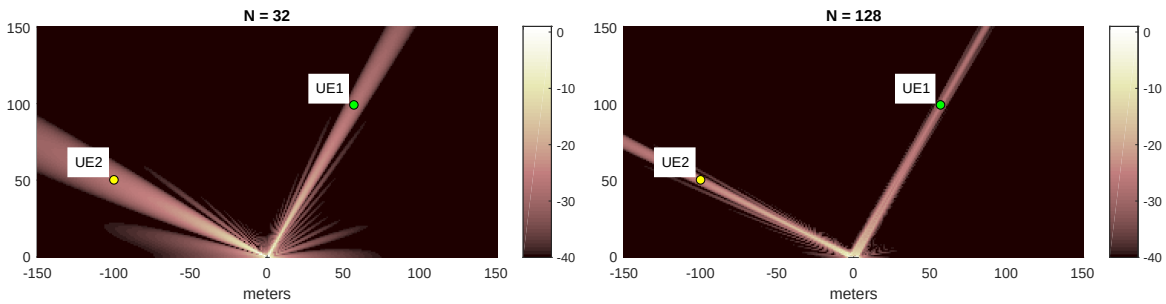

(a) (b)

Figure 1.6: The ability of massive MIMO to create a number of non-interfering beams towards users. (a) 32-antenna massive MIMO creates wider beams that allow simultaneous servicing of fewer users than with (b) 128-antenna massive MIMO (Flordelis *et al.*, 2015). Note, the total amount of power is the same as for the single antenna transmission.

The beamforming feature reveals a new ability for massive MIMO systems, that of radio resource re-use where the same radio resource can be used for a number of users. Let us consider another user within the same cell, UE2 in Figure 1.5 (c,d). In the same way as for UE1, the BS can create a second beam for the second user, as illustrated in Figure 1.6 (a,b) (Flordelis *et al.*, 2015). Since the two beams do not interfere with each other, the two users can receive the same amount of throughput as in independent signal transmission. Note, in Figure 1.6, two layers of signals are illustrated simultaneously in the plots. Thus, in this example, the ability of massive MIMO to re-use its resource can almost double the network's throughput. This is another very useful feature of massive MIMO systems, which makes the technology promising for the next-generation networks.

To be able to create focused beams towards users, a BS has to know the signal propagation channels between them. Thus, the BS has to measure the UEs' channels before beamforming. In wireless communication theory, the channel measurement operation is called the procedure of the channel estimation (CE), and this is one of the critical steps for establishing a wireless connection between communicating units (Cho *et al.*,

2010). Without knowledge of the propagation channel, the receiver cannot demodulate signals, and the transmitter cannot leverage the multi-antenna array benefits.

1.5 Channel Estimation and its Challenges in Massive MIMO

To establish a wireless connection, communicating units first have to measure channels between each other to know the distortion that signals experience during the transmission and to be able to recover the distorted signals. To measure the channels, the BS and UE have to perform the channel estimation procedure, during which a known signal from each end is used to calculate distortion coefficients (Sesia *et al.*, 2011; Cho *et al.*, 2010; Abu-Rgheff, 2007). Since the signal is known, the receiver can compare the received signal with the undistorted one and, based on this comparison, can calculate the distortion coefficients. Such signals are called training, reference or pilot signals (Marzetta, 2010).

To some extent, the channel can be considered as static if the communicating units and the surrounding environment are stationary, but if they move or the surrounding environment is changing, then the channel becomes dynamic. Due to the dynamic nature of the wireless channel, the communicating units have to measure the channel again and again, or periodically, which is time and energy consuming. Periodic measurement CE adds complexity as the more the environment changes, the more the channel varies, and consequently, the more frequently CE is required (Chen *et al.*, 2011; Mai *et al.*, 2007). The frequent CE becomes an issue mostly for the UE side since a mobile device is usually powered by a battery that has a limited capacity. Hence, it may discharge the battery very quickly and reduce the quality of the customer's experience. Reducing the power consumption of the CE on the UE side and the CE frequency are considered challenging tasks in the CE procedure (Hassanieh *et al.*, 2012; Fedorov *et al.*, 2015).

1.5.1 Channel Estimation in Multi-Antenna Systems

Increasing the number of antennas in the BS/UE also introduces complexity. In multiple antenna systems, channels h_{mn} between all pairs of antennas of the BS and UE have to be measured, as illustrated in Figure 1.7. Instead of estimating a single 1×1 channel, both BS and UE need to estimate $M \times N$ channels where the BS has N antennas and

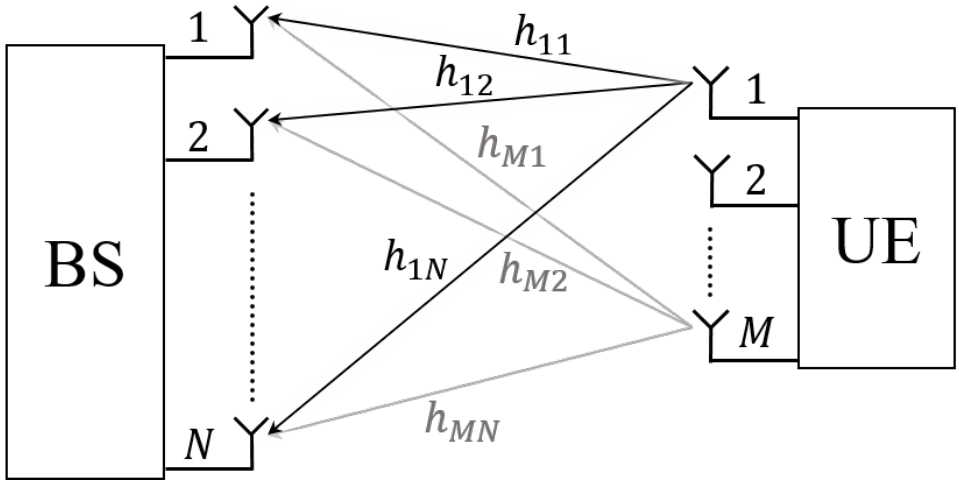

Figure 1.7: Multi-antenna system.

the UE has M (Ji *et al.*, 2017). The increase in the number of antennas on both sides is one of the main trends in achieving high-throughput connection in next-generation communication (Fleury *et al.*, 2002; Foschini and Gans, 1998; Chizhik *et al.*, 2000). The majority of communicating units will be operating through multi-antenna systems because such antennas significantly increase the throughput for the same amount of spectrum (Telatar, 1999; Shamai and Wyner, 1997a,b). In the modern communication field, such kinds of systems are called MIMO systems (Sesia *et al.*, 2011; Marzetta *et al.*, 2016; Björnson *et al.*, 2017), and if a huge number of antenna elements is used in a unit, for example $N > 32$, then such networks are called massive MIMO networks (Shepard *et al.*, 2012; Rusek *et al.*, 2013; Harris *et al.*, 2016).

The throughput is increasing due to the physical principles of the multi-antenna systems that allow reduction of the interference in (1.1), i.e., increasing the system's spectral efficiency (SE) (Ngo *et al.*, 2013; Vieira *et al.*, 2014; Larsson *et al.*, 2014). The number of channels is also increased according to the number of antennas (Hoydis *et al.*, 2013; Björnson *et al.*, 2016). This requires allocating a portion of the gained throughput for measuring the increased number of channels (Marzetta, 2010; Fodor *et al.*, 2017). The throughput increase is paid for by the usage of more complex and expensive hardware and by developing more advanced signal processing algorithms, including a more complicated procedure for CE. In multi-antenna systems, in addition to the frequent channel measurements as for the 1×1 channel, the CE procedure has to be done for a far greater number of antennas (Yang and Marzetta, 2013; Björnson *et al.*, 2014; Prabhu *et al.*, 2017).

The beamforming feature is capable not only of reducing the inter-cell interference,

but also providing constructive interference at the receiver side when the same signal constructively adds up at a receiver's antenna (Gao *et al.*, 2015). In contrast to the destructive interference that occurs in multipath propagation, in constructive interference the receiving antenna receives well-aligned copies of the transmitted signal that together give a signal with a higher signal-to-noise ratio (SNR). However, to form a proper beam that enables constructive interference on the UE's antennas, the BS needs to know $M \times N$ channels, otherwise, some signals may add up destructively, which nullifies all the effort directed to increase the throughput. With the knowledge of the distortion coefficients of $M \times N$ channels, the BS can adjust all signals before transmission through its antennas in such a way that the delivered signals create constructive interference at the receiver's antennas.

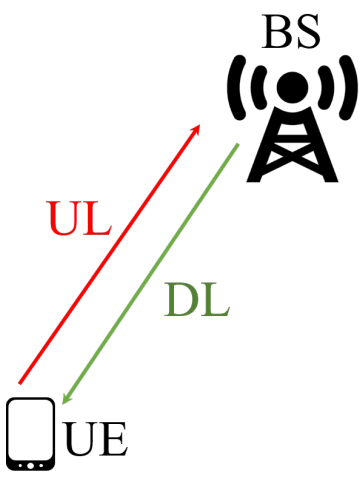

Figure 1.8: Definition of uplink and downlink signals.

As mentioned previously, BSs are mounted in elevated places, which means that signals go DOWN from BSs to users, and go UP from users' BSs (Sesia *et al.*, 2011). In order to avoid confusion in terminology, signals and channels are specified as follows: the signals that are transmitted from the UE are called Uplink uplink (UL) signals and the channels are called UL channels; the signals transmitted from the BS are called Downlink downlink (DL) signals and channels are called DL channels, as illustrated in Figure 1.8. Hence, a UE receives DL signals and measures DL channels, and a BS receives UL signals and measures UL channels.

1.5.2 Downlink Channel Feedback

Unlike in 1×1 systems, in MIMO systems, the CE has to take into account not only the distortion coefficients but also the interference state of the channel caused by the simultaneous transmission from a number of antennas. In other literature, the expanded information about the channel is called channel state information (CSI), but there is no need to specify the difference between CE and CSI in this dissertation. Before transmission, the transmitter needs to be sure that signals transmitted from its antennas do not create destructive interference at the receiver's antennas. This requires the transmitter to know both UL and DL channels. The main challenge in this scheme is to obtain the estimation of the opposite channel (Flordelis *et al.*, 2018; Ji *et al.*, 2017; Jiang *et al.*, 2015). For example, a BS needs to somehow obtain the estimation of a DL channel before signal transmission.

A simple approach is to send DL training signals to a UE, which estimates the DL channels on its M antennas and then feeds the information about the DL channels back to the BS. Such a feedback mechanism is known as DL feedback. The feedback information may contain either a full DL channel measurement, a sparse representation of the DL channel, or an indicator from a codebook that contains a limited number of states of DL channels. The transmission of the whole DL channel measurement is impractical since it can occupy a large part of the UL transmission. Due to this problem, a limited feedback approach has been adopted (Love *et al.*, 2008). Wireless systems with a relatively small number of antennas could quite successfully work with codebooks (Schulz, 2015; Love *et al.*, 2003; Love and Heath, 2005; Raghavan *et al.*, 2007). However, the increased number of antennas on the BS side expanded the volume of the codebooks, which made the approach ineffective in terms of computation and memory consumption. The main drawback of codebooks is that the limited number of states in a codebook cannot closely approximate the real channel (Flordelis *et al.*, 2018). Thus, the feedback technology has moved to the sparse representation of the measured channels, which successfully compresses the feedback data (Song *et al.*, 2010; Joung and Sun, 2014; Liu *et al.*, 2016).

Despite the approach where the UE estimates the full DL channel and sends it back to the BS not being preferable for next-generation communication, the estimation of $M \times N$ channels is time-consuming in itself. The BS needs to send signals from each of its N antennas separately to avoid mixing of signals on the UE's antennas. The signals can be separated either in the time domain, in the frequency domain, in a code domain where different orthogonal codes are allocated for different antennas of the BS,

or a combination of these approaches, as illustrated in Figure 1.9. In any case, the UE has to estimate all these DL channels by performing the CE procedure and then send the information about the DL channels back to the BS, which means that the UE increases its energy consumption due to the CE and feedback transmission, and hence, developing practical solutions for eliminating or reducing feedback is considered one of the most vital directions for massive MIMO systems (Björnson *et al.*, 2017).

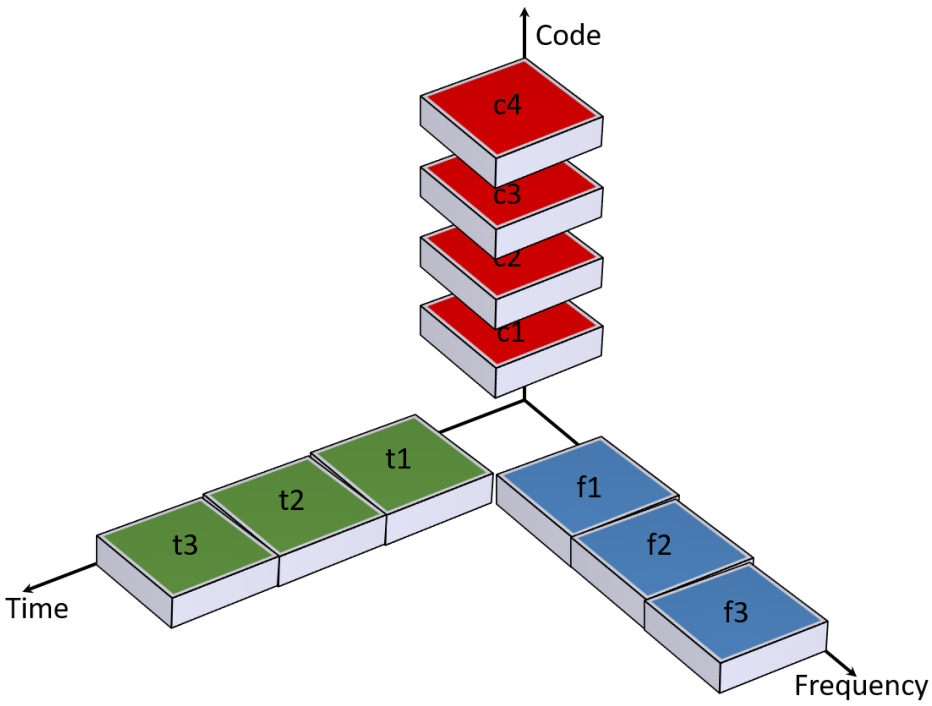

Figure 1.9: Time, frequency, and code division domains.

1.5.3 Channel Reciprocity

Another drawback of channel estimation at the UE side is that the BS may receive information about the outdated DL channel since the DL transmission of training signals takes some time, and in addition, the UL transmission of the feedback also requires some time (Zhou and Giannakis, 2004). This type of channel estimation approach is acceptable for low mobility scenarios due to slow variation of channels but is unacceptable for high mobility scenarios because the outdated channel may not have any similarity with the actual one. In order to overcome the power consumption and outdated channel problems, the idea of the reciprocity of channels has been adopted (Vieira *et al.*, 2017; Björnson *et al.*, 2017). The channel reciprocity simply means that

UL and DL channels are equivalent. Once channels become equivalent, the need to send the channel feedback disappears because the DL channel can be measured during the UL CE procedure. The channel reciprocity approach also reduces the UE's energy consumption since the UE does not need to estimate the channel and feed back the results to the BS. The major part of the CE is delegated to the BS side.

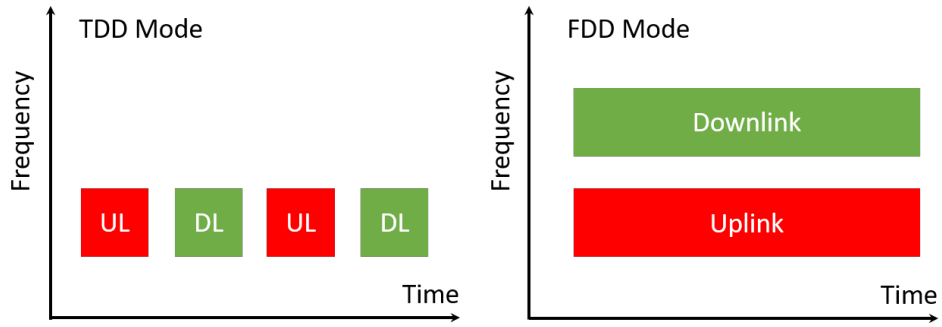

Figure 1.10: Definition of time division duplex and frequency division duplex modes.

Unfortunately, the idea of channel reciprocity suits only the time division duplex (TDD) mode of communication, used in Wi-Fi and some LTE networks. The TDD mode means that UL and DL signals occupy the same frequency band and are separated in the time domain, i.e., a BS and UE communicate sequentially, as illustrated in Figure 1.10. In the case of the frequency division duplex (FDD) communication mode, which is typical in LTE, the UL and DL channels occupy different frequency bands. The separation is in the frequency domain and this allows communication between the BS and UE simultaneously. The FDD mode potentially has higher throughput due to the feature of simultaneous communication. As illustrated in Figure 1.10, the area occupied by the DL transmission in the TDD mode is smaller than in the FDD mode, where coloured areas indicate the amount of transmitted data. Due to the frequency separation, the UL and DL channels significantly differ from each other, which means the channel reciprocity approach is not applicable (Vasisht *et al.*, 2016; Hugl *et al.*, 2002). Because of this, DL channel acquisition becomes even more challenging for the FDD mode. So, the question of developing practical solutions for channel feedback mechanisms remains unanswered for the FDD mode.

1.5.4 Channel Prediction

The majority of the existing prototypes of the next-generation networks are operating on the TDD mode (Shepard *et al.*, 2012; Rusek *et al.*, 2013; Harris *et al.*, 2016).

Although the channel reciprocity allows the DL channel to be obtained from the observation of UL signals, the measured channels are still delayed. From the moment of the UL signal transmission to the moment of the CE results calculation, the actual channel of the UE may significantly change due to mobility, and the estimated DL channel may become outdated (Duel-Hallen *et al.*, 2000; Duel-Hallen, 2007; Zhou and Giannakis, 2004). The outdated channels can severely reduce the throughput of a network (Harris *et al.*, 2017). For the high mobility and high throughput scenarios, the actuality of the channel estimation becomes vital. Unfortunately, the CE procedure always captures the past and never gives the actual channel. Taking this into account, an effective approach in massive MIMO systems is to predict the channel values at future times when they will be used. It is an appropriate moment in the evolution of wireless communication to move from *the channel estimation paradigm* to *the channel prediction paradigm*. The challenging question that arises here is how to predict the channel in massive MIMO systems.

Currently, there are some studies regarding channel prediction for massive MIMO systems, but their approaches are not standardized, and the results have to be evaluated through realistic test cases (Li *et al.*, 2017; Kashyap *et al.*, 2017; Adeogun *et al.*, 2015). Usually, channel prediction deals with predictions in the time domain, i.e., channel states are constructed to fit the channel in future moments. However, the same idea of predicting a channel can be used in the frequency (Kumar *et al.*, 2014; Palleit and Weber, 2010; Han *et al.*, 2018), code, and spatial domains. Since the question of how to predict channel in massive MIMO systems is still open, it is worthwhile investigating ways to enable the design of practical solutions for channel prediction.

1.5.5 Channel Reconstruction

The channel reconstruction topic is closely related to, or partially overlaps with, the channel prediction idea. The main purpose of the channel reconstruction approach is to recover a full channel from its incomplete observation. For example, in the orthogonal frequency division multiplexing (OFDM) transmission (Cho *et al.*, 2010; Sesia *et al.*, 2011), a channel can be measured on some subcarriers and then, using a solution for channel reconstruction, recovered for the remaining subcarriers. In the case of massive MIMO systems, because of the massive numbers of antennas on both the BS and UE sides, obtaining incomplete observation can be justified by the reduction in the computational complexity, hardware cost, or radio resource scarcity (Gkizeli and Karystinos, 2014; Sohrabi and Yu, 2016; Mohammadi and Ghannouchi, 2011). This

dissertation concentrates on designing a solution that reconstructs the full massive MIMO channel from incomplete observation caused by the incompleteness of the set of antennas that are capable of transmitting.

While the trend to increase the number of antennas at the UE side is evident (Samsung, 2018; Qualcomm, 2018), having more antennas for transmission on the UE side will not only increase the hardware complexity and consume more energy, but also make the pilot contamination problem even worse (Marzetta, 2010). The leading UE producers are making efforts to optimize the antenna design by limiting the number of antennas for transmission, that is, only using a subset of the antennas for transmission, and the others for receive-only. As a result, it is expected that in 5G, the number of transmitting antennas will be smaller than the total number of antennas on the UE side. Since only a subset of antennas is used for transmission, the BS can measure an incomplete channel. Hence, the available channel capacity becomes smaller than the capacity of the full channel where all UE antennas are involved in transmission.

To improve the capacity of the channel that is incompletely observed, new channel reconstruction approaches for non-transmitting antennas have to be investigated. The channel reconstruction solutions can become helpful for channel capacity enhancement due to their ability to complete the observed incomplete channels with the reconstructed ones. The main problem in channel reconstruction for a non-transmitting antenna is that the BS cannot obtain any observations about the non-transmitting antenna. Thus, it is a challenging task to construct an appropriate relation between the channel of a non-transmitting antenna and the channels of transmitting antennas. To reconstruct channels for non-transmitting antennas, the BS has to obtain information about the location of non-transmitting antennas, infer the propagation paths of potential signals as if they are transmitted by the non-transmitting antennas (Vasisht *et al.*, 2016; Palleit and Weber, 2010; Han *et al.*, 2018), and also estimate the orientations of the non-transmitting antennas.

1.5.6 Channel Scarcity in Next-Generation Communication

As mentioned above, the major part of the CE is performed at the BS side. To measure UL and DL channels at the BS side, the antennas of a UE send training UL signals that are separated either in frequency, time or code domains, as illustrated in Figure 1.9. To send training signals, each antenna occupies a time slot and a frequency bandwidth, and may use a specific code to reduce interference to other signals, depending on a communication protocol. Transmitting antennas need to use signals that do not

interfere with each other. It can be achieved if the signals are sent in different time slots or different frequency bands. The signals also do not interfere with each other if they are separated by orthogonal codes (Abu-Rgheff, 2007; Sesia *et al.*, 2011). The time window during which the UE can send training signals through its antennas is limited by the channel coherence time (Flordelis *et al.*, 2016). The numbers of available frequencies and orthogonal codes are also limited by communication protocols (Rappaport *et al.*, 2015; Cho *et al.*, 2010). Hence, with the increase in the number of transmitting antennas, the amount of available radio resources such as time, frequency, and codes becomes smaller.

At some point, the number of antennas can become large enough to create a scarcity of the available radio resource, such as available bandwidth, orthogonal codes, and time slots. The logic of the scarcity emergence can be explained with an example. Let us define TW as the channel's coherence time specified for a network, during which the channel is considered constant, and BW as the network's bandwidth. Let $TW \times BW$ be the available time–frequency resource, N_{code} be the maximum number of available codes, and $tb \times fb$ be the size of the smallest time–frequency resource that can be allocated to an antenna, then the maximum number of antennas that can be used without collisions cannot be greater than $N_{ant} = N_{code} \frac{TW}{tb} \frac{BW}{fb}$. In practice, protocols for radio communication use some redundancy in their resource allocation to increase the probability of successful reception. An antenna usually occupies a time–frequency resource that is bigger than the smallest resource, which means that the maximum number of antennas becomes smaller than N_{ant}.

To mitigate the problem of radio resource limitation, the idea of using a limited number of transmitting antennas on the UE side has been adopted (Molisch *et al.*, 2003; Theofilakos and Kanatas, 2006). Instead of transmitting using M antennas, a UE is forced to use a smaller number $m < M$ of antennas for transmission. The full set of antennas is used only for reception. The benefits of using fewer transmitting antennas are in the reduction of hardware cost due to cheaper receiver hardware, a more efficient usage of the available radio resource, and less energy consumption, caused by the reduction in the number of transmitting antennas. Everything looks good from the benefits perspective. However, the reduction in the number of transmitting antennas leads to a decrease in the throughput caused by the reduction of the channels' capacity (Telatar, 1999; Foschini and Gans, 1998; Chizhik *et al.*, 2000). Instead of having a full set of $M \times N$ channels for transmission, a network can exploit an incomplete set of $m \times N$ channels, which decreases the capacity. This happens because the BS cannot

observe the channels of non-transmitting antennas and consequently cannot obtain the full set of $M \times N$ DL channels. The channel capacity cannot be enhanced by only increasing the number of non-transmitting antennas. Hence, it is worth investigating channel reconstruction approaches to design a solution that enables the reconstruction of the channels for non-transmitting antennas.

1.5.7 Summary on Channel Estimation

Channel estimation is increasing in complexity due to advancements in wireless communication technologies. For some applications, especially related to the FDD mode, it is too complex and becomes an insurmountable obstacle to further developments, rendering future FDD massive MIMO technology improvements questionable. If an efficient solution for DL channel feedback cannot be found, then the FDD massive MIMO approach is not viable (Björnson *et al.*, 2016). The challenges described above regarding the procedure of CE can be summarized as follows:

- CE consumes excessive energy at the UE side;
- CE has an ineffective feedback mechanism;
- CE gives an outdated channel state instead of the actual state;
- CE cannot provide channel state information for non-transmitting antennas.

These challenges make current networks slow with regard to throughput and response latency, which has to be addressed to enable next-generation communication. This thesis attempts to develop solutions that mitigate the challenges of the relationship of the wireless channel with the propagation environment.

1.6 Research Problems and Contributions

The core of the CE problem is in its complexity, which increases with the advancement of communication technology. Notably, the complexity becomes too high in massive MIMO systems, threatening MIMO technology adoption. The main aim of the thesis is to investigate the relationship between the channel and the propagation environment to develop efficient schemes for channel derivation in massive MIMO systems, especially the reconstruction of channels for non-transmitting antennas of a UE based on the known spatial relationship between non-transmitting and transmitting antennas. This

means that in order to reconstruct channels for non-transmitting antennas, further steps have to be taken:

1. Create a spatially consistent channel model that is suitable for massive MIMO networks, especially under dense deployment;
2. Develop an algorithm that can estimate the locations of the communicating UEs based on the conventional network's signals;
3. Develop an algorithm that can estimate the orientations of the communicating UEs based on the conventional network's signals;
4. Design a scheme that can reconstruct the channels for non-transmitting antennas based on the location and orientation of the UEs.

The thesis follows the logic described and includes following contributions:

- **Creating a consistent massive MIMO channel simulation model**

  Since the designed solutions are intended to serve next-generation networks, they have to be evaluated on channel simulation models that take into account the recently explored phenomena of massive MIMO systems. **Firstly**, massive MIMO systems have a much higher spatial resolution than conventional MIMO systems (Raschkowski *et al.*, 2015). As a result, new wireless channel models have to be able to model the detailed space features of the surrounding environment. **Secondly**, recent experiments revealed that a common plane wave propagation (PWP) model is no longer suitable for massive MIMO due to the ability of a massive MIMO BS prototype to recognize the sphericity of an incoming wavefront (Zhang *et al.*, 2016; Vieira *et al.*, 2017), and thus new channel models also need to incorporate the spherical wave propagation (SWP) model to simulate more realistic and spatially consistent channels. **Thirdly**, to enable the channel prediction feature, new channel models must be able to simulate realistic 3D movements of UEs accurately. This requires very carefully simulating the change of signal polarization to make it consistent with the movement.

  In this piece of work, a massive MIMO channel simulation model was developed to satisfy the requirements listed above. The contributions are summarized as follows:

  1. A realistic environment from Google maps was incorporated into the massive MIMO channel simulation. To my knowledge, at that time, this was the

first channel model that could take into account and handle a geometrically accurate representation of a realistic environment.

2. The spherical waves propagation assumption has been incorporated into the massive MIMO channel simulation model. The simulation results have revealed the importance of incorporating the spherical propagation of signals and accurate representation of the environment in channel generation, especially for massive MIMO systems.
3. The phenomenon of electromagnetic wave reflection from an arbitrarily inclined surface by taking into account the wave polarization transformation has been carefully described. The reflection from an arbitrarily inclined surface has not been described in other existing channel models. The feature enables the proposed channel model to deal with complex-shaped objects and simulate a spatially consistent evolution of the simulated channel.
4. The results of channel simulation show the importance of considering the detailed 3D characteristics of the surroundings. Even slightly inclined walls can have significant influence on channels compared with models having only vertical and horizontal surfaces, due to different propagation paths, angles of reflection, and changes of polarization.

The research outcomes have been presented at the IEEE ICC 2017 conference in Paris, France (Fedorov *et al.*, 2017).

- **Localization of users based on the SWP model using only UL signals**

  In this contribution, the main focus is on developing practical solutions to localize users in areas with a high population density (e.g., urban areas during business hours and airports), where it is challenging to provide high-quality mobile communication due to the need to serve a large number of UEs using limited radio resources (time, frequency, code, as in Figure 1.9). Such areas are typically covered by many small cells with distance between adjacent BSs less than a few hundred meters (Björnson *et al.*, 2017; Alsharif *et al.*, 2017). In such scenarios, the SWP model can be adopted to locate UEs more accurately in massive MIMO systems because the linear dimensions of a massive MIMO array are large enough to distinguish the spherical shapes of the incoming wavefronts. Based on the SWP model, the difference in time delay experienced at different antenna elements of a BS can be described through small phase shifts between antenna measurements.

In this piece of work, a user localization algorithm that carefully processes the measured phase shifts has been developed. The algorithm leverages the advantages of spherical wave propagation since the spherical propagation allows simultaneously estimating the angle of arrival and the propagation distance from the user equipment to each antenna element in the BS. The contributions are summarized as follows:

1. A localization algorithm has been designed to localize UEs by using the very first signals that are sent during the random access channel (RACH) synchronization procedure in both single-path and multipath environments. To my knowledge, this is the first method that exploits RACH signals for localization. Since the RACH procedure is performed before the actual connection of a UE to the network, the location information obtained can be immediately used to optimize the allocation of radio resource and perform accurate beamforming.

2. In the case of single-path LoS communication, the localization problem has been formulated as the problem of the common sphere parameters estimation based on phase shifts between antenna measurements. The last can be solved using the Bancroft algorithm that has a closed-form solution.

3. In the case of multipath propagation, the localization problem has been formulated as a nonlinear data-fitting optimization problem that leverages the OFDM nature of UL signals to obtain more measurements for the joint estimation of the shapes of all the incoming signals.

4. Because of non-ideal synchronization between massive MIMO antennas, measurements always have relative phase noise that can significantly degrade the localization accuracy. A phase noise cancellation algorithm has been developed to improve this. The algorithm estimates phase noise in a massive MIMO antenna array and then removes it from the measurements, by which the accuracy can be improved by almost a factor of two.

5. A proof-of-concept experiment has been conducted to validate the feasibility of the localization algorithm in the single-path case using the Otago University massive MIMO prototype. For this purpose, I have built the Otago University massive MIMO prototype using two Ettus USRPs N210 and one 10 MHz reference NI OctoClock (Ettus, 2019).

The research outcomes have been presented at the IEEE ICCCN 2018 conference in Hangzhou, China (Fedorov *et al.*, 2018).

- **Reconstruction of channels for non-transmitting antennas**

  For a UE that has M antennas, from which only $m < M$ can transmit signals, the location information is not sufficient for reconstructing channels for the $M - m$ non-transmitting antennas. Due to this issue, in addition to location information, the UE orientation information must also be obtained. This information is used to derive the locations and orientations of non-transmitting antennas. Once the locations and orientations are known, the channels for non-transmitting antennas can be reconstructed.

  In this research, a novel channel reconstruction methodology has been developed that can reconstruct channels for non-transmitting antennas using an incomplete set of UL signals from the transmitting antennas. The contributions are summarized as follows:

  1. A solution for estimation of the orientation of a transmitting antenna has been developed that is suitable for both single-path and multipath propagation environments. The proposed solution is a closed-form solution and was developed from first principles using Maxwell's equations (Orfanidis, 2014). The main idea of the solution is informed by the strong relation between the voltage induced at a receiving antenna and the mutual orientation of two communicating antennas in 3D space. The solution reconstructs the orientation of a transmitting antenna based on the voltage measurements by exploring the above relationship.
  2. A voltage-extracting methodology has been developed. The methodology allows the extraction of voltages induced from the UL signals on distributed antenna elements of a BS during the CE procedure. Due to the spatial consistency of the massive MIMO channel simulation model, the spatially diversified voltage measurements and the consideration of SWP assumption allow the reconstruction of the orientation of the transmitting antenna.
  3. A realistic human gait has been incorporated to the simulation model to imitate consistent orientation change during a pedestrian walk. The primary purpose is to examine the ability of the algorithm to estimate orientation in an aggressive type of movement, which occurs, for example, when a UE is

located in a person's hand that is swinging back and forth. The results of simulation show that for high SNRs the orientation of transmitting antennas can be accurately estimated with less than 1° of error for SNRs higher than 25 dB.

4. The steps for the reconstruction of a full massive MIMO channel have been thoroughly described. The results of simulation experiments show that channels for non-transmitting antennas can be reconstructed with high accuracy for SNRs higher than 15 dB.

The research outcomes have been presented at the IFIP Networking 2019 conference in Warsaw, Poland.

1.7 Thesis Structure

The final channel reconstruction algorithm is built on three consecutive steps: creating a channel model for the evaluation of algorithms, designing a localization algorithm for DL channel reconstruction, and designing an antenna orientation estimation algorithm for reconstruction of non-transmitting antenna channels. Hence, the structure of the thesis is straightforward: Chapter 2 introduces the technical background of the area investigated, and material related to approaches and techniques for 3D channel simulation, localization of users based on uplink signals in wireless communication networks, and channel reconstruction; Chapter 3 gives a detailed description of how to model the massive MIMO reception and signals' interactions with objects within a propagation environment; Chapter 4 describes two localization algorithms designed to localize users in single-path and multipath propagation environments; Chapter 5 explains the steps for antenna orientation reconstruction and the methodology of channel reconstruction for non-transmitting antennas; finally, Chapter 6 contains the discussion of the work and the directions for future research.

Figure 1.11 illustrates the different parts of the thesis in a graph structure in order to provide a visualization of the thesis. The contribution chapters are depicted together with the background chapter to illustrate my personal vision of how much the corresponding research fields have been investigated by other researchers, indicated by the amount of overlap between the boxes. In contrast, the areas outside the background area signify the contribution volume that the dissertation presents. Thus, a couple of small contributions in well-studied areas such as channel modeling and localization

have enabled a couple of strong contributions such as the reconstruction of the orientation of a single transmitting antenna and channel reconstruction for a non-transmitting antenna.

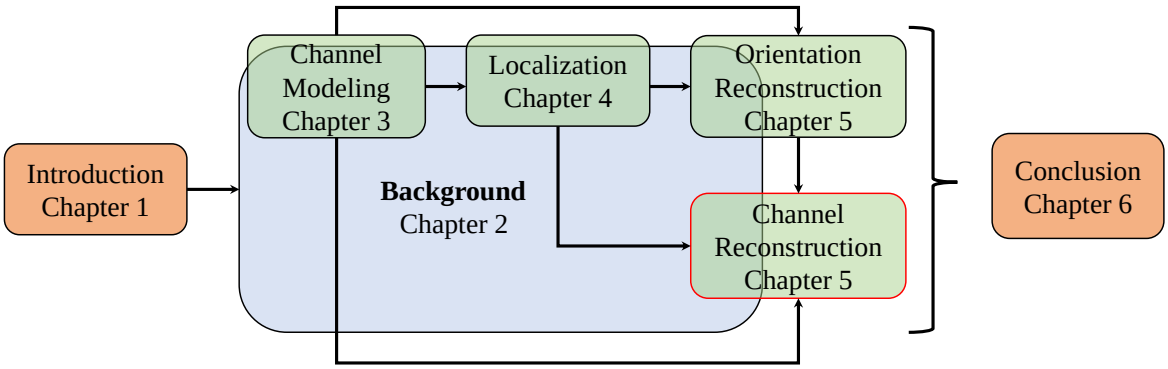

Figure 1.11: Layout of the thesis and the relationship between different parts. The intersections of the Background with the four contributions indicate how much the topics have been studied by other researchers (in my personal opinion).

Chapter 2

Background and Literature Review

The main contribution of this thesis is in proposing novel approaches to the description of wireless signal generation and propagation. In general, these novel approaches can be grouped into two significant areas:

1. incorporating the Spherical Wave Propagation (SWP) model in massive MIMO systems, which enabled the accurate localization of users on a single BS with a massive MIMO antenna;

2. incorporating the orientation of an antenna in signal generation and reception, which enabled the channel reconstruction for non-transmitting antennas via the estimation of orientations of transmitting antennas of a UE.

These two novelties have a direct implication on channel models. Once they are incorporated in the signal propagation, the channel model becomes spatially consistent.

Before going deep into the background study, I would like to share my vision as to why channel estimation became ineffective in current multi-antenna-based communication and will most likely become the bottleneck for the next generation of communication.

2.1 Evolution of Wireless Communication Theory

It is well known that the development of a theory occurs in spurts. At first, the knowledge of an area accumulates until it reaches maturity. At the mature stage, the theory generates technology based on available knowledge. Technology justifies the mature theory to some extent and additionally reveals far more new questions, for which the volume of accumulated knowledge is not enough to explain the new findings.

For example, Albert Einstein predicted gravitational waves in 1916, but it took almost a century for general relativity theory to become mature and to generate technology that can support the theory. In 2015, the LIGO laboratory confirmed the existence of gravitational waves and revealed many new, previously unseen observations regarding our universe and its evolution (Abbott *et al.*, 2016).

A similar process is occurring in wireless communication theory. The preparation for the 5G era has predicted many new benefits such as higher throughput, lower response time, connection everywhere, etc. Preliminary theoretical investigations also inform challenging questions regarding the deployment of next-generation networks, such as resource allocation, channel estimation, accommodation of a massive number of users, etc. The steps conducted can be considered an accumulation of knowledge in communication theory.

Currently, the technology is in the form of experimental prototypes. Across the world, large laboratories using experimental testbeds like massive MIMO (Shepard *et al.*, 2012; Rusek *et al.*, 2013; Harris *et al.*, 2016; Facebook, 2016; Huawei, 2017; Ericsson, 2018) and millimeter wave (mmWave) (Rappaport *et al.*, 2013; Qualcomm, 2018; Instruments, 2018; Facebook, 2016) prototypes have expanded the boundaries of communication theory. For example, the collaborative experiments of Docomo and Mitsubishi on a multi-antenna prototype have shown a significant increase in the throughput, to more than 25 GBps (DOCOMO, 2018), which was almost impossible in 2015; the collaborative experiments of Lund and Bristol Universities with massive MIMO prototypes have revealed that a standard assumption about plane wave propagation (PWP) is no longer suitable for massive MIMO antenna arrays, Figure 2.1 (a): the increasing number of antennas increases the linear dimensions of a massive MIMO antenna array, which expands its near-field region. For example, according to the Rayleigh distance (Zhou *et al.*, 2015), for a 100-antenna-elements massive MIMO and a signal carrier frequency of 2.6 GHz, the near-field distance can be expanded up to 600 meters. Nowadays, the distances between BSs are not more than a few hundreds of meters in dense urban areas (Björnson *et al.*, 2017), which means that potentially almost all UEs are located in the near-field region. If a signal is sent from the near-field region, then a massive MIMO can distinguish the spherical shape of the incoming signal. Hence, signal-processing algorithms that are intended to serve dense deployment areas have to incorporate a spherical wave propagation model to be able to handle near-field channels properly and, consequently, increase the throughput of the networks effectively (Rusek *et al.*, 2013; Harris *et al.*, 2016).

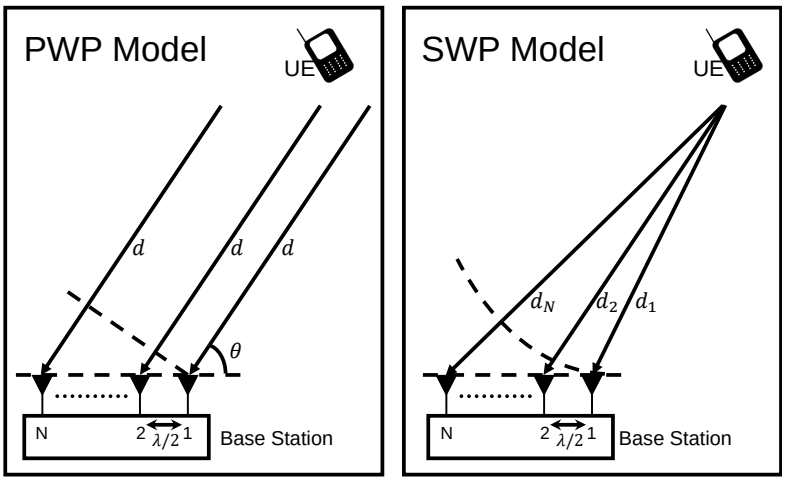

(a) (b)

Figure 2.1: Difference between plane wave propagation and spherical wave propagation assumptions: all paths from UE antenna to BS antenna elements cover the same distance with the same angle of arrival in (a), but cover different distances and have different angles of arrivals in (b).

The main conclusion from the experiments with prototypes is that the phenomena of signal propagation and wireless channels are still not thoroughly understood. For example, the question of how to model the interaction of signals with objects within the propagation environment is still open, and there is no standardized approach for taking it into account; the meaning of channel is treated as something that distorts signals and emerges only after a signal transmission. Although it is believed that the signal propagation environment defines the channel, there is no clear description of how the surrounding environment determines the channel, which parameters of the environment play a dominant role in the channel formation and how to take them into account.

2.1.1 Stochastic Channel Models: Why Channel Estimation Became a Bottleneck

Conventional wireless channel models contain statistics of specific parameters such as the number of propagation paths, time delays, angles of arrival and departure, coefficients of attenuation, etc., which are collected during real channel measuring campaigns. Such channels models are called stochastic channel models and include WINNER (Heino *et al.*, 2010), 3GPP-3D (Heino *et al.*, 2010), IMT-Advanced (ITU, 2009),

and Quadriga (Jaeckel *et al.*, 2014). The advantages of these models are that they describe a vast variety of environments and scenarios: outdoor, indoor and outdoor-to-indoor. Since the models contain realistic statistics from extensive measuring campaigns, the models are widely accepted and used by the communication society. Interestingly, the first models were designed initially for 2D propagation but then extended to handle 3D propagation; that is why they are not comprehensive in representing 3D features of signal propagation. For example, a proper reflection from an arbitrary surface and consecutive polarization change are not considered.

Overall, the main drawback of the stochastic approach, from the channel estimation point of view, is that each realization of a channel generates new parameters that are inconsistent regarding the channel evolution caused by the mobility of the propagation environment (Raschkowski *et al.*, 2015). This drawback influenced the procedure of CE in that the CE always estimates the channel after its realization, i.e., the CE measures the previous realization of the channel but not the actual one, which has to be realized during the next transmission. Due to the inconsistent channel evolution, the channel's realizations can be quite different, especially if the positions of UEs and BSs are changing with time. as a result, there is no opportunity to design a solution within the stochastic model's paradigm that could track the channel's evolution, and consequently, predict the channel. To develop channel prediction solutions, researchers usually use or estimate the statistics of the channel variation, which describe the exact behavior of a specific channel model but not a realistic channel, and which are hard to obtain in practice due to the non-stationary nature of a radio channel in reality. Such types of prediction solutions may fail in their predictions due to the channel's behaviour changes, which usually happens in practice (Raschkowski *et al.*, 2015).

In addition, all the considered stochastic channel models are not capable of supporting spherical waves, a crucial factor for developing channel tracking solutions. Unfortunately, stochastic models are "blindly" used by the majority of wireless communication researchers especially by beginner researchers who consider these models as ground truth. Instead of observing all features of the signal propagation, they are limited by the borders of these models. Hence, they are working with a limited number of tools, which does not allow them to design solutions with capabilities beyond the edges of the paradigm. From my point of view, this is the main reason for delays in the progress in channel prediction and channel inference approaches. Due to the wide usage of stochastic models, the approaches for inferring and predicting the actual state of the wireless channel have not been widely investigated. For these reasons, the

current procedures of channel estimation measure outdated states of channels, and one of the possible ways of increasing the CE accuracy is to perform the procedure more frequently, which may add a tremendous channel estimation overhead.

There have been some attempts to design channel prediction solutions, but most of them still suffer from inconsistent channel models. Thus, the approaches from the early 2000s suffer from oversimplified stochastic channel models that consider 2D mobility and constant channel parameters (Dong *et al.*, 2001; Cao and Wang, 2004; Wong and Evans, 2005). These studies do not predict channels across frequency bands, which is crucial in the FDD mode. The recently proposed channel prediction solutions still incorporate stochastic modeling approaches, but the channel models used are much more comprehensive. Thus, in a static point-to-point MIMO communication, the estimation of frequency-independent parameters of the UL propagation has allowed the prediction of the DL channel in a different frequency band (Palleit and Weber, 2010). A logical extension of this work is the reduction in the feedback transmission frequency in beamforming by predicting DL channels from the observation of UL channels (Vasisht *et al.*, 2016). The authors of this work have managed to tune signal beams towards UEs without any DL feedback. In both studies, the feasibility of channel prediction in different frequency bands has been experimentally justified; however, the mobility case and the ability to predict the channel state in the time domain have not been investigated.

The newest solutions on channel prediction cover mobility scenarios but still consider 2D scenarios without proper modeling of signal reflection and polarization change caused by the movement (Adeogun *et al.*, 2015; Kashyap *et al.*, 2017). In the first of these works, a well known Kalman filter approach is used to predict the channel (Adeogun *et al.*, 2015). The authors wanted to investigate the problem of the feedback frequency reduction using channel prediction. Based on simulation experiments, they conclude that prediction helps to increase the throughput in comparison with no prediction communication. In the second work, the authors used an ESPRIT approach to estimate multipath propagation components, which were then used to predict the future channel (Kashyap *et al.*, 2017). Although their solution successfully predicted the channel, the assumption that they used considers non-variable propagation parameters over a long time scale, which is quite unrealistic (Raschkowski *et al.*, 2015).

All in all, the development of effective channel estimation solutions has been negatively influenced by the widespread acceptance and use of the stochastic channel models, which are not comprehensive regarding spatial channel evolution. Thus, to

enable the development of effective channel estimation approaches, it is crucial to develop consistent channel models that are capable of accurately describing the evolution of the radio channel.

2.2 Channel Models for Next-Generation Networks

One of the ways to address the problem of outdated channel measurements is to design proper channel models that allow deriving the channel for any point in time including current and future points. To do this, the models have to incorporate deterministic elements of the channel. By leveraging the deterministic part of the propagation environment, the actual and future states of the channel can be partially inferred. Any determined object or determined movement within the propagation environment can be considered as a deterministic element of the channel. An object can be described by its geometry and physical parameters; a movement can be described by its velocity and direction. This dissertation aims to design an approach for channel modeling that can generate channels based on realistic environments (Figure 2.2), which can be taken from open-source maps such as Google Maps (Google, 2005) and OpenStreetMaps (OpenStreetMaps, 2004). In this way, I believe, the channel models can become flexible regarding setting communication scenarios (dense urban areas or hilly rural areas) and can become comprehensive in representing possible propagation features that are highly dependent on the area of consideration: radio channels in Moscow are quite different from radio channels in Dunedin, for example.

2.2.1 Cluster-Based Channel Models

There are some models that include a deterministic element in the channel generation COST2100 (Liu *et al.*, 2012), GEMV2 (Boban *et al.*, 2014), METIS (Raschkowski *et al.*, 2015). The primary aim of these models is to emulate a consistent channel evolution. A significant separation from the stochastic models has been achieved by incorporating reflecting clusters with fixed positions in COST2100 channel models. Each cluster has a region from which it is visible, i.e., the UEs located in the region can see the cluster. At first, COST2100 constructs a generic propagation environment around a BS, then simulates the movement of users within the environment. Simultaneous operation of two or more BSs becomes an issue for COST2100 because it generates a specific environment for each BS separately and the matching of several environments becomes a complex task. In addition, the mobility of UEs does not incorporate a

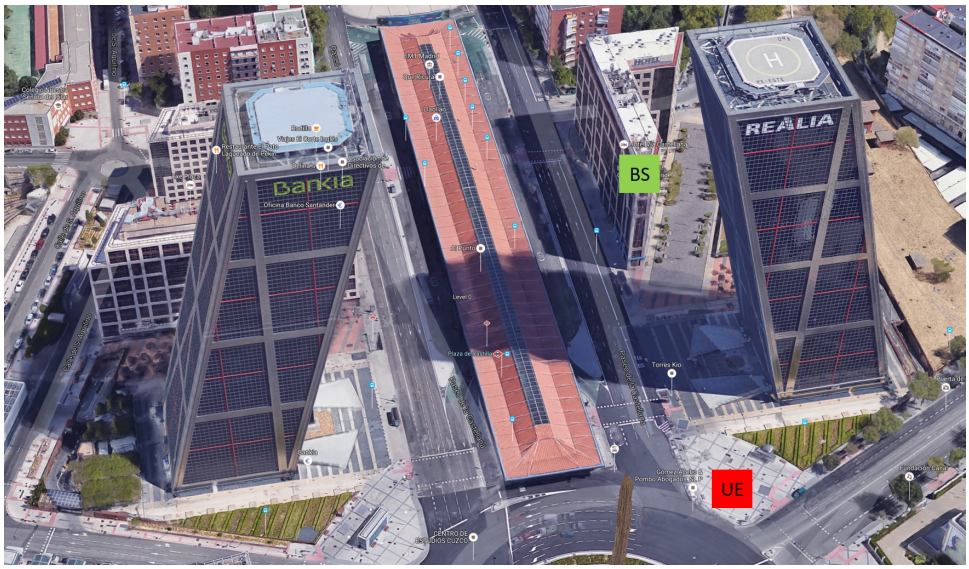

Figure 2.2: The Gate of Europe in Madrid of Spain are twin inclined office buildings. During propagation, the signals between BS and UE are reflected by the twin office buildings.

consistent polarization change. The polarization change behaviour is based on statistics that are taken from another channel model, whose construction is based on indoor channel measurements (Quitin *et al.*, 2010). Hence, this family of channel models is not appropriate for developing channel tracking solutions.

2.2.2 Geometry Based Channels Models

The other models, GEMV2 (Boban *et al.*, 2014) and METIS (Raschkowski *et al.*, 2015), are more geometry-based channel models. They can take into account 3D city models. The GEMV2 model is designed to simulate vehicular communication. It generates a channel based on information about vehicles, buildings and foliage outlines, which are taken from OpenStreetMaps and traffic video records. To avoid simulation complexity, GEMV2 works with a small area with a round-trip distance of less than 500 meters. Although the simulation results are consistent with the measurements (Boban *et al.*, 2014), the calculation of reflections is based on a 2D map, which can to some extent be acceptable for a flat area, but not for a hilly area. The model has to be further developed to handle 3D reflection phenomena.

The recent METIS (Raschkowski *et al.*, 2015) project gives a list of requirements regarding the modeling of a next-generation wireless channel, including accurate 3D modeling of the surroundings, antenna polarization, and the spread of spherical waves,

and proposes a new wireless model with the aim of improving the spatial consistency of the channel model. By experimentally measuring many signal propagation effects and comparing them with simulation results, the authors of METIS concluded that all the existing models are inadequate for 5G requirements and cannot cover the required scenarios and environmental influences. The majority of channel simulation methods described in this dissertation are adopted from this model.

The main drawback of METIS is that it is strictly limited to consideration of vertical walls, instead of inclined walls, to simulate the major interaction effects of signals with obstacles, such as specular reflection (Noerpel *et al.*, 1991) and changes of polarization (Fedorov *et al.*, 2019). Meanwhile, many objects of a real environment have complex shapes with inclined surfaces (e.g., Figure 2.2) that can have a significant impact on channel behaviour. Consequently, the generated channel may significantly differ from the real channel because polarization is very sensitive to the parameter of inclination, as the parallel and perpendicular components of polarization have different coefficients of reflection (Orfanidis, 2014; Landron *et al.*, 1996). Hence, METIS also requires the incorporation of a proper reflection feature that takes into account the inclination of the objects.

2.2.3 Summary on Channel Models

It is apparent from the discussion above that one of the challenges in designing new approaches for CE that estimates the actual state of the channel is to create channel models that are consistent regarding the channel evolution, environment description, and mobility modeling. The **first aim of this thesis** is to design a spatially consistent channel model that can take into account a realistic environment and arbitrary mobility within the environment to derive the channel's state at any moment of time. In the dissertation, the environmental consistency of the proposed channel model is achieved through a thorough derivation of the electromagnetic signal reflection phenomenon from an arbitrary inclined surface by taking into account the polarization of signals. The model incorporates Google Maps data into its simulation and validates the significance of considering the inclination of reflecting objects and an accurate geometrical representation of the surrounding medium. The model also incorporates the spherical wave propagation model, which becomes crucial in the channel generation especially for large antenna arrays because the difference between the channels generated by plane waves and spherical waves becomes obvious. The full description of the channel design is presented in Chapter 3. The full comparison of the discussed channel

models is listed in Table 2.1.

	Support 3D	Support Massive MIMO	Support Dual Mobility	Support Dynamic Modeling	Support Polarization Change	Support Spatial Consistency	Support SWP	Support Complex Shapes
IMT-Adv	no	no	no	no	no	no	no	no
WINNER+	yes	limited	no	no	no	no	no	no
3GPP-3D	yes	limited	no	no	no	no	no	no
COST2100	yes	limited	no	yes	limited	no	no	no
QuaDRiGa	yes	yes	limited	yes	limited	no	no	no
GEMV2	limited	no	yes	yes	limited	limited	no	no
METIS SC	yes	yes	limited	limited	limited	limited	no	no
METIS GC	yes	yes	yes	yes	limited	yes	yes	no
Proposed	yes	yes	yes	yes	yes	yes	yes	yes

Table 2.1: Comparison of different channel models. SC - Stochastic Channel, GC - Geometry based Channel

2.3 Transition to Deterministic Channel Paradigm

To overcome the challenging open questions in wireless channel estimation described in Section 1.5.7, entirely new approaches need to be developed in channel estimation theory. The primary objective of the thesis is to explore the relationship between the propagation environment and the radio channel. If the surrounding environment is known, then the channel becomes almost deterministic and depends on the position and action of UEs (Witrisal *et al.*, 2016). The description of the relationship between the propagation environment and the radio channel is an attempt to transition from the stochastic channel paradigm to the deterministic channel paradigm. In the massive MIMO networks, the radio channel becomes nearly deterministic due to the high spatial resolution of massive antenna arrays (Ngo and Larsson, 2017).

An analogy of this effect can be constructed from a biological example. A creature with a single photoreceptor cell (antenna) can recognize if there is light or not and its intensity while a creature with a massive number of photoreceptor cells (many antennas)realizes where the light comes from and its source if the creature is intelligent enough. In the case of the first creature, the environment is unknown, and the light has a random nature with its statistics, which can be collected if based on a long observation. If conditions in the environment change, the single-cell creature has to collect statistics again. On the other hand, the multi-cell creature to some extent sees the environment and can make some decisions, depending on the changes. Even if the single-cell creature is capable of making decisions, then these decisions will be taken much more slowly than in the case of the multi-cell creature due to less observation. In the same way, a BS equipped with a massive MIMO antenna can, to some extent, see the surrounding propagation environment through the radio channel and can definitely recognize sources of communications UEs (sources of light), and hence, for such types of BS, channels become determined by the environment and the positions of UEs.

The motivation of the transition to deterministic channel paradigm is that a channel can be treated as a deterministic function of an environment and a signal:

$$H = f(\mathrm{Env}, x_{\mathrm{UE}}, s). \tag{2.1}$$

Here H is the channel response, f is the deterministic channel function, Env is the environment, x_{UE} is the location of the UE, and s is the transmitted signal. The meaning of

the environment aggregates physicomechanical properties of the propagation medium and its 3D geometrical characteristics. The function f is describing different paths, through which a transmitted signal propagates in a multipath environment. Different paths originate from different electromagnetic phenomena such as reflection, scattering, diffraction, and refraction (Richter, 2005). Since each phenomenon has an explicit representation as a function of the user's location and the surrounding environment (Raschkowski *et al.*, 2015; Tse and Vishwanath, 2005), function f can be explicitly derived as a combination of these functions.

2.4 Channel Inference in Massive MIMO Networks

One of the primary benefits of the deterministic channel representation (2.1) is that if f, Env, and x_{UE} are known, then the channel can be calculated for any signal s even in the case of the frequency separation of the UL and DL signals, as illustrated in Figure 1.10. In an ideal situation, the CE procedure can be eliminated completely since channels can be calculated directly. If at some moment in the future, the coordinates of the user and the state of the surrounding environment are known via motion tracking (Rapoport *et al.*, 2010; Golovan and Cepe, 2016), then the future channel can be explicitly calculated based on (2.1). An explicit representation of the radio channel, such as (2.1), enables a clear and easy understanding of the idea of channel reconstruction and prediction, or in other words, channel inference. By using such an approach, BSs can track UE channels based on their spatial relations with the surrounding environment and infer (predict/reconstruct) channels for other positions, signals, and points in time. The deterministic channel paradigm can become helpful in answering the challenging questions regarding channel prediction and reconstruction listed in Section 1.5.7.

The issue with the deterministic channel paradigm is in obtaining information about f, Env, and x_{UE} for the channel function (2.1). This information can be obtained from a received UL signal, because the signal captures the propagation information during its travel from the user's position x_{UE} to the BS, and its interaction with the environment (Env). In fact, during propagation, wireless signals are distorted due to inevitable interactions with the propagation medium. The distortion can be treated as the capture of information about f, Env, and x_{UE}: after the signal's reception, the captured information can be extracted (Richter, 2005; Fleury *et al.*, 1999, 2002), and then the required channel (2.1) can be inferred. Consequently, the **second aim of the thesis** is to develop solutions for the extraction of propagation information from

received UL signals for further use in the DL channel inference.

There is extensive literature on inferring channels from limited or compressed feedback (Love *et al.*, 2008; Schulz, 2015; Love *et al.*, 2003; Love and Heath, 2005; Raghavan *et al.*, 2007; Song *et al.*, 2010; Joung and Sun, 2014; Liu *et al.*, 2016). All of these methods deal with the feedback mechanism. As was discussed in Chapter 1, all the feedback solutions are aimed at reducing the size of the information that is included into feedback but not the frequency of feedback transmission. Hence, a UE has to frequently measure the channel and send its state back to the servicing BS, which is time- and energy-consuming. There is also a constant interest in solutions that predict channels in the time domain (Dong *et al.*, 2001; Cao and Wang, 2004; Wong and Evans, 2005; Kashyap *et al.*, 2017; Duel-Hallen *et al.*, 2000; Duel-Hallen, 2007), which was discussed earlier in the thesis. All the listed channel prediction approaches do not predict/reconstruct channels in the frequency, code, or spatial domains.

Although there are concerns regarding the feedback overhead in FDD massive MIMO systems, some big companies like Ericsson, Samsung, and Huawei have already announced the deployment of their FDD massive MIMO networks (Ericsson, 2017; Samsung, 2017; Huawei, 2018). Since the FDD mode of communication has theoretically higher capacity than the TDD mode, as discussed in Chapter 1, many researchers are putting effort into achieving a practical solution that can overcome the problem of a large feedback overhead. The available solutions can be divided into two based on the approaches used: stochastic and deterministic.

The stochastic DL channel inference approaches exploit the special correlation properties of massive MIMO channels to infer the channels in different frequency bands. The main problem of all stochastic solutions is in the availability of long-term channel statistics, which are hard to obtain, and the consideration of very strong assumptions regarding the stochastic properties of channel matrices (Aleksiejunas, 2016; Han *et al.*, 2010). By using the stochastic properties, the author of the first work can decompose the channel correlation matrices in a way such that fading parameters in space, time and frequency domains become independent, which is not realistic (Raschkowski *et al.*, 2015; Björnson *et al.*, 2017).

On the other hand, the deterministic DL channel inference approaches exploit the estimated propagation parameters such as directions of arrival and departure, distances, attenuation coefficients, etc; currently there are many robust methods to estimate these propagation parameters (Richter, 2005; Fleury *et al.*, 1999; Li *et al.*, 2017; Kumar *et al.*, 2014; Fedorov *et al.*, 2018). The benefits of such approaches are that there is no need

to collect statistics about the channel: the channel inference can be performed in any environment as long as parameters are estimated accurately. However, the main problem of all deterministic solutions is that the quality of the inferred channel is highly dependent on the accuracy of the parameter estimations. That is why the main focus of these solutions is on achieving an accurate estimation of the propagation parameters. Further sections discuss deterministic approaches in DL channel inference.

2.4.1 Estimation of Directions of Arrival

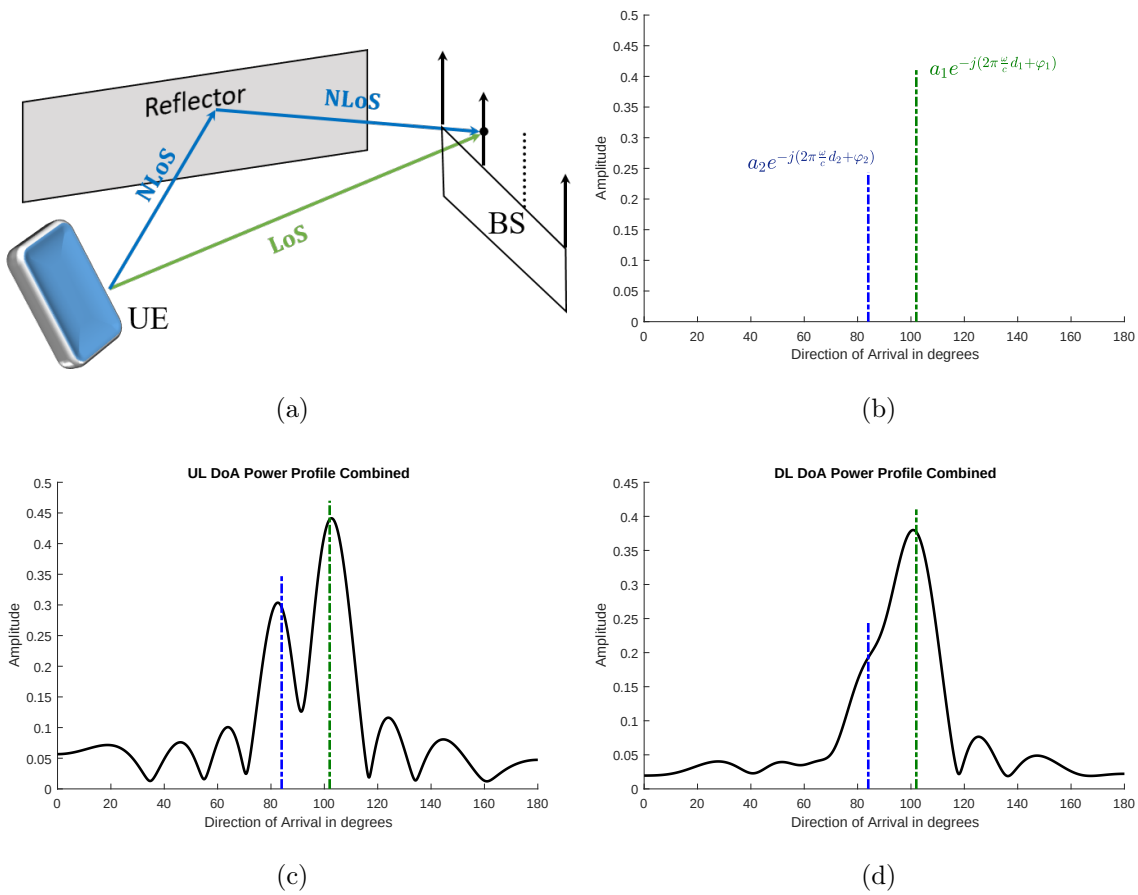

Figure 2.3: Disadvantages of MUSIC- and ESPRIT-like methods in determination of directions of arrival. (a) Consider two signal paths emerging from 102° and 84° as shown. (b) Depicts the signal components of individual paths across direction of arrival. (c) Power profile is constructed based on uplink frequencies. (d) Power profile is constructed based on downlink frequencies.

The deterministic DL channel inference approaches exploit the propagation reci-

procity idea where it is assumed that UL and DL signals propagate through the same paths. Unlike the channel reciprocity idea where signals experience the same channel distortions, here signals propagate through the same environment. Consequently, due to frequency separation, UL and DL signals are distorted differently. In (Palleit and Weber, 2009, 2010; Adeogun *et al.*, 2015), the authors demonstrated the usefulness of direction of arrival parameters for DL channel reconstruction in some special scenarios. They used MUSIC- and ESPRIT-like algorithms, which find directions of arrival based on spikes in the angular power profiles (Schmidt, 1986; Roy and Kailath, 1989; Swindlehurst *et al.*, 1992). It is known that angular power profile algorithms suffer from inaccurate direction determination in the case of multipath propagation (Vasisht *et al.*, 2016). As illustrated in Figure 2.3, the direction of arrival power profile has different shapes depending on the frequency band, which affects the estimation results. The direction mismatch influences the DL channel reconstruction accuracy.

The example in Figure 2.3 is plotted in Matlab by following the same approach described in (Vasisht *et al.*, 2016). For clarity, the power profile has been constructed for a BS with 8 antenna elements. The center frequencies for the UL and DL channels are 2.6 GHz – 30 MHz and 2.6 GHz + 30 MHz, respectively, 40 MHz separation. The LoS signal comes from the angle 102° with attenuation a_1 and phase φ_1; the covered distance is 100 meters. The reflected NLoS path has a direction of arrival of 84°, and attenuation a_2; phase φ_2, and distance $d_2 = 120$ meters. With the increase in the number of antennas, the width of the spikes become narrower, which increases the accuracy of direction estimation. However, adding more antennas does not help to overcome the method's weakness because for any resolution (for any number of antennas), there can exist closely located paths that reduce the accuracy of direction estimation. In practice, this significantly impairs the DL channel reconstruction performance (Vasisht *et al.*, 2016).

2.4.2 Estimation of Multipath Propagation Components

To overcome the direction mismatch, (Imtiaz *et al.*, 2014) used more advanced multipath component extraction optimization methods such as a SAGE-based algorithm (Fleury *et al.*, 1999, 2002). The authors did not aim to reconstruct the DL channel; instead they wanted to investigate the dissimilarity of UL and DL channels depending on the value of frequency separation of the two channels. According to their work, the number of propagation paths had the highest impact on the dissimilarity of UL and DL channels. Another well-known method that advances the multipath component

extraction is the use of RiMAX algorithms (iterative maximum-likelihood criterion) (Salmi *et al.*, 2009; Li *et al.*, 2017). In these works, the authors aimed to investigate robust methods in multipath component extraction rather than in DL channel inference. According to their results, the RiMAX algorithms are suitable for high-accuracy extraction of multipath components, and hence, can be helpful for DL channel reconstruction. The critical component of their approach is to expand the dimensionality of the measurements through leveraging the orthogonal frequency division multiplexing (OFDM) nature of signals (Sesia *et al.*, 2011). Orthogonal subcarriers become independent observation channels for obtaining measurements, and the number of measurements increases according to the number of subcarriers (Fedorov *et al.*, 2018).

OFDM is a convenient way to transmit signals in parallel using multiple orthogonal carriers, which are called subcarriers. The main advantage of the OFDM method is that signals can be transmitted with a lower sampling rate. Historically, the purpose of using orthogonal subcarriers was to combat the problem of intersymbol interference due to the lack of accurate time synchronization (Cho *et al.*, 2010; Alard and Lassalle, 1987), but now, due to software and hardware development, the advantages of the methods have broadened. The method is considered a key technology in 5G since OFDM can provide higher spectral efficiency than other modulation techniques and flexible resource allocation, as illustrated in Figure 2.4. In addition, it is sensitive to Doppler shift and frequency synchronization; that is why effective signal processing solutions have to be proposed to mitigate the disadvantages.

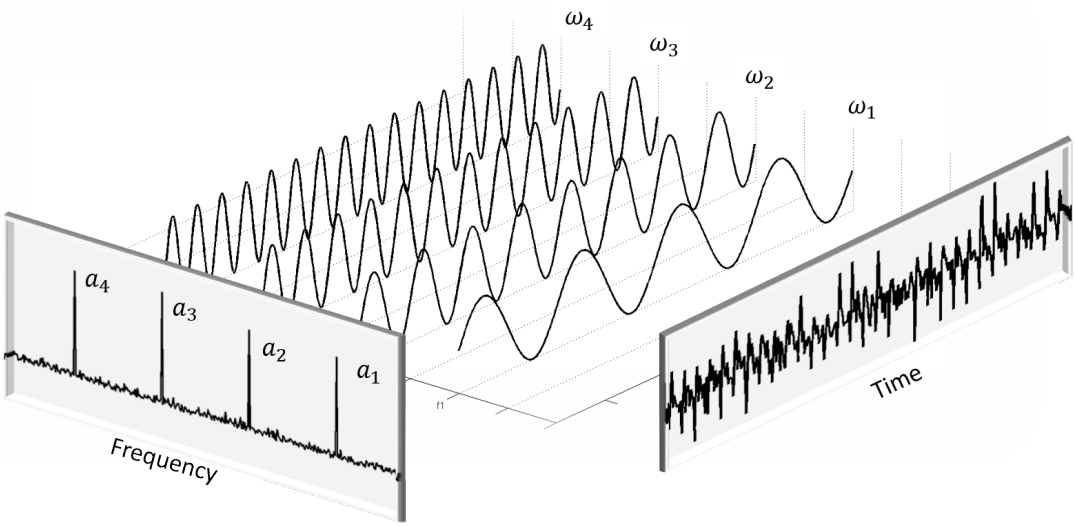

Figure 2.4: OFDM signal. Orthogonal subcarriers can be shared among up to four users, or can be used by one user. Flexible resource allocation.

The main issue with SAGE- and RiMAX-like algorithms is in their computational complexity. A number of research groups are working on alternative optimization methods that are less computationally complex. In (Vasisht *et al.*, 2016), an MIT team proposed a method that extracts propagation components by matching a comprehensive channel model with the channel measurements. By using observations from all OFDM subcarriers, their method can extract exact paths through which signals travel. The paths are parameterized via a frequency-independent amplitude, direction of arrival, and distance to the source. The main drawback of their method is that they model reflection coefficients as a frequency-independent attenuation coefficient multiplied by a frequency-dependent exponent $ae^{j\phi}$, which is not in agreement with the Fresnel reflection coefficient (Raschkowski *et al.*, 2015; Landron *et al.*, 1996; Fedorov *et al.*, 2017). Also, the algorithm has been developed by considering a BS with a conventional MIMO antenna system, which allowed them to design the solution under the PWP assumption.

A very recent solution on DL channel reconstruction has been proposed (Han *et al.*, 2018). Although this work was not available during my PhD research, this is an interesting study. The main contribution of this work is in introducing a Newtonized orthogonal matching pursuit algorithm that extracts multipath propagation delays and paths gains. Unfortunately, the authors did not consider the SWP assumption, which is an experimentally justified suitable propagation model for massive MIMO (Shepard *et al.*, 2012; Rusek *et al.*, 2013; Harris *et al.*, 2016).

All the considered DL inference solutions do not consider the more realistic SWP assumption. The common disadvantage for all methods is that they do not consider a truly mobile scenario with a consistent motion of UE and its polarization change. The majority of solutions provide solutions in 2D scenarios with non-changing polarization of transmitting and receiving antennas. For next-generation communication, providing high throughput in a mobility scenario is considered to be one of the critical requirements.

A logical evolution of DL channel reconstruction methods lies in the channel reconstruction for non-transmitting antennas. The question here is how to obtain multipath propagation parameters for non-transmitting antennas. As mentioned previously, the final aim of the thesis is to design a solution that is flexible in reconstructing and predicting channels for non-transmitting antennas in any domain: in the frequency domain (channel reconstruction), in the time domain (channel prediction), and in spatial or code domains (channel inference).

2.4.3 Estimation of Location

The main effort in the extraction of propagation information is put into finding the location of the UE since it is a convenient parameter, through which the problem of the propagation information extraction can be formulated as a well-known optimization problem (Vasisht *et al.*, 2015; Fedorov *et al.*, 2018, 2019). In other words, the localization of users and the extraction of environmental information can be performed jointly. In addition, the location information is useful for many other applications such as safety and servicing applications, yet the interest of the thesis is in the channel deviation (2.1) at any moment of time and any position.

The most promising application within the channel estimation topic that will be used in next-generation communication is beamforming (Figure 1.6). The beamforming technique allows a BS to create focused beams towards UEs, by which energy consumption and interference can be significantly reduced and radio resources can be reused to increase capacity (Vasisht *et al.*, 2016; Vieira *et al.*, 2017; Malkowsky *et al.*, 2017; Zhang *et al.*, 2016). In the conventional beamforming schemes, the beam's precoding is based on the DL channel feedback, which causes an extreme overhead to DL data communications. In some cases, especially in the multi-user FDD communication, the downlink channel feedback may exceed half of the overall traffic generated by the BS (Björnson *et al.*, 2016). To reduce the overhead, location-based DL channel inferring approaches have been proposed. For static UEs, with the knowledge of the location information, some of these approaches can perform accurate beamforming without the use of any channel feedback (Palleit and Weber, 2010; Vasisht *et al.*, 2016). However, all of these methods are constructed for conventional MIMOs and do not take into account propagation effects that are specific for massive MIMO systems with large antenna arrays. Consequently, the localization solutions for massive MIMO systems are highly desirable to enable efficient beamforming and interference cancellation.

There are many methods in UE location determination. Since the dissertation deals with channel estimation methods, and the position knowledge is required for channel description, only specific network-oriented localization methods are considered. All the existing localization methods can be broadly divided into three groups: UE-based, UE-assisted, or network-based (Cherian and Rudrapatna, 2013). In the UE-based methods, the UE obtains a location measurement and calculates its position. These methods are not considered in the dissertation because they add high computational load on the UE side and additional energy consumption in feeding back the location information to the network. In UE-assisted methods, the UE provides positioning measurements to the

network and the network uses those to calculate the position of the UE. These methods also require energy expenditure on measuring and transmitting additional positioning information to the network, which is why they are not considered in the dissertation.

The preferred methods are network-based where the network calculates the UE position without UE involvement. UEs act as usual while the BSs locate them from the users' UL signals. This means that UEs do not spend energy on localization and transmission of any additional information. Also, localization based on UL signals is quicker than the UE-based and UE-assisted methods since the additional information transmission step is omitted. There are also complex methods used by third parties and application providers, and proprietary methods based on GPS, Wi-Fi and others. The exchange of location information between the network and the third parties requires time, and consequently, extends the localization delay for the network, which is critical for channel prediction methods. As a result, only network-based localization methods are considered in the dissertation.

In the design of localization solutions, the central focus is put on areas with high population density (e.g., urban areas in business hours and airports), where it is challenging to provide high-quality mobile communication using limited radio resources, due to the need to serve a large number of UEs. Such areas are typically covered by many small cells with distances between adjacent BSs less than a few hundred meters (Björnson *et al.*, 2017; Alsharif *et al.*, 2017). In such scenarios, the SWP model can be adopted to locate UEs more accurately in massive MIMO systems because the linear dimensions of a massive MIMO array are large enough to distinguish the spherical shapes of the incoming wavefronts. Figure 2.1 compares the SWP model with the conventional PWP model. Due to the sphericity of an incoming wavefront, a BS with a massive MIMO antenna can estimate the center of the wavefront's sphere, which is the location of the UE that transmits the signal. Hence, the adoption of the SWP assumption allows a massive MIMO BS to estimate the direction and distance to the transmitting UE simultaneously.

2.4.4 Estimation of Antenna Orientation

During the finding of a UE's location x_{UE}, a massive MIMO BS extracts the propagation information f and Env, which gives opportunity to explicitly calculate the corresponding channel (2.1). However, in the case when a UE has more than one antenna, and some of them are not capable of transmitting signals due to a design solution or radio resource limitation, the location information becomes insufficient to

calculate channels. This is because the channels of transmitting and non-transmitting antennas become uncorrelated if the non-transmitting antennas have orthogonal orientations relative to the transmitting antennas (Orfanidis, 2014). Hence, the channels of the non-transmitting antennas cannot be inferred from the channels of transmitting antennas. Therefore, in addition to the location information, the information about the orientation of antennas also has to be incorporated into the channel function (2.1).

Due to a fixed design of user equipment (smartphones, laptops, cars, etc.), the orientations of non-transmitting antennas can be derived from the orientation of the UE, which is defined by the orientation of the transmitting antennas. As illustrated in Figure 2.5, the orientation of the UE can be defined by the directions of the two red transmitting antennas. It is assumed that among the transmitting antennas at least two are not parallel. Hence, the updated version of (2.1) can be derived as follows:

$$H = f(\text{Env}, x_{\text{UE}}, \Omega, s), \tag{2.2}$$

where Ω is the orientation matrix of the UE in the global coordinate system, as illustrated in Figure 2.5.

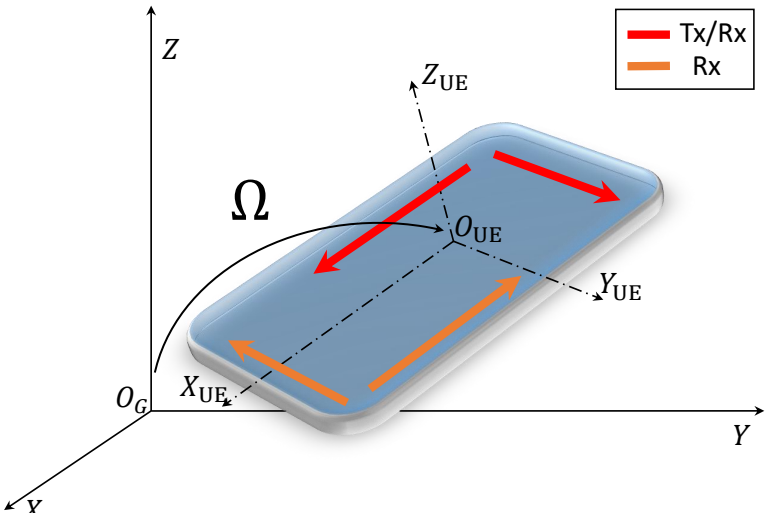

Figure 2.5: Definition of UE's orientation relative to the global coordinate system O_G. Red arrows indicate transmitting antennas, orange arrows indicate non-transmitting antennas.

The solution for antenna orientation reconstruction is motivated by the strong relationship between the voltage induced at a receiving antenna and the mutual orientation of two communicating antennas. The key idea of our solution is to reconstruct the orientation of a transmitting antenna based on the voltage measurements by exploring

the relationship above. For a BS with a massive MIMO antenna, the voltages induced from the uplink signals can be measured on the distributed antenna elements. The spatially diversified voltage measurements allow reconstruction of the orientation of the transmitting antenna. Based on these orientations, the BS defines the orientation Ω of the UE. Based on the orientation of the UE, the orientations of the non-transmitting antennas are then reconstructed. Finally, using extracted information f, Env, x_{UE}, and Ω, the BS becomes capable of reconstructing channels for the non-transmitting antennas.

In this thesis, I present ARDI (**A**ntenna orientation **R**econstruction and **D**ownlink channel **I**nference), a scheme that can reconstruct the full DL channel based on incomplete UL channel measurements. The heart of ARDI is the reconstruction of UE antenna orientation at the BS based only on UL signals. In fact, the channel response is closely related to the mutual orientations of transmitting and receiving antennas. The design of ARDI has been based on this observation. It allows the BS to use channel response as a measurement and calculate the orientation of the transmitting antennas of the UE based on the electromagnetic signal propagation model. Since the layout of the antennas at a UE is assumed to be known, as it is related to the UE model, the orientations and other propagation parameters for the non-transmitting antennas can be inferred. Based on the inferred propagation parameters the full downlink channel can be reconstructed.

ARDI is the first scheme that can reconstruct the orientation of an antenna based on a single electromagnetic impulse in both single-path and multipath propagation environments. A closed-form solution for antenna orientation reconstruction in both propagation environments has been derived. Although there are some works on antenna array orientation reconstruction (Sinclair, 1950; Shahmansoori *et al.*, 2018; Talvitie *et al.*, 2017), none of them can reconstruct the orientation of a single antenna or reconstruct the orientation of a UE based on two transmitting antennas. Also, the proposed solution is the first that can infer channels for non-transmitting antennas at any domains.

2.5 Summary

This chapter provides an overview of the current state of the radio channel modeling theory. Although the understanding of the wireless signal propagation phenomenon has been dramatically expanded by observations from experimental campaigns using

advanced massive MIMO and mmWave hardware, the implementation of the knowledge obtained in practice is minimal. For example, the majority of the signal processing algorithms designed for massive MIMO systems do not take into account the spherical propagation of wireless signals, which can be beneficial for massive MIMO algorithms such as user localization and user motion tracking. Also, the chapter sheds light on related works regarding channel reconstruction approaches, and discusses their pros and cons. Finally, the chapter ends with the formulation of the problem of channel reconstruction for non-transmitting antennas and gives a high-level description of the proposed solution, which is based on antenna orientation reconstruction.

Chapter 3

Channel Modeling

In this chapter, approaches for modeling massive MIMO channels are described. The phenomenon of reflection of wireless signals from an arbitrary inclined rough surface is thoroughly investigated by taking into account the signals polarization and spatial distribution of massive MIMO antenna elements. The difference between plane and spherical wave propagation models is analyzed.

3.1 Introduction

The wireless signal propagation environment is very complex in terms of accurate modeling. It is a challenging task to take into account all factors such as shapes of landscapes, buildings, moving objects and trees/foliage. Even though field experiments are more appropriate for validating new concepts and approaches on wireless communication than simulation tests, field tests are commonly costly and time-consuming. Hence, new concepts in wireless communication are generally first validated through simulation, which demands the simulation models to be realistic enough to provide all required effects of a real propagation environment.

In the wireless communication field, similar to the graphics field (Wyvill and Trotman, 1990, 1992), the approach of ray tracing is widely used to model the geometry-based multipath propagation channel. The approach takes into account the geometrical and physical conditions of the propagation environment where a transmitted signal undergoes reflection, diffraction, and scattering from different objects (Noerpel *et al.*, 1991). While the multipath signal propagation enables communication when the LoS direction is blocked, it also has other effects including destructive and constructive interference and phase shifting of the signal. The destructive effects can have harmful

impacts on the power of the received signal and make the signal undecodable due to low SNR. Hence, it is vital to develop a simulation module that could model such effects, which in turn allows the development of efficient solutions to deal with the effects.

Existing 3-Dimensional multipath models can be generally divided into two groups: Stochastic Channel (SC) models (Jaeckel *et al.*, 2014; Heino *et al.*, 2010; the 3rd Generation Partnership Project, 2015; ITU, 2009) and Geometry-based Channel (GC) models (Liu *et al.*, 2012; Quitin *et al.*, 2010; Boban *et al.*, 2014; Raschkowski *et al.*, 2015) which also can incorporate stochastic parameters. The SC models have comparatively low complexity, but do not consider specific environment features, whereas a local medium is the main determining factor of a channel. Therefore, SC models are not suitable to validate new concepts such as beamforming and radio resource reuse that require specific characteristics of a local environment to deal with spatial properties of a channel. The GC models consider the impact of surrounding infrastructures, but they consider only simple shapes of objects described using vertical and horizontal planes. Meanwhile, many objects in a real environment have complex shapes with inclined surfaces (e.g. Figure 2.2) that can have a crucial impact on channel behavior. By considering simple objects shapes, the GC models limit the number of available propagation scenarios. For example, a radio channel for a hilly area may have specific features, which cannot be modeled using simple vertical and horizontal shapes. Consequently, the modeled channel may significantly differ from the real channel due to the inaccuracy of the environment representation. These facts became a motivation for developing new channel modeling methods that enable generating realistic channels.

The goal of this work is to examine the significance of consideration of geometrically accurate representation of the propagation environment in the simulation of a radio channel. The difference in the channel generation under the SWP and PWP assumptions is also examined. To achieve the goals, channels are generated for the same environment (Kio Torres area on Figure 2.2) but under different conditions (simple and accurate geometrical representations, under SWP and PWP assumptions) and then compared. The difference between the channels can be seen from the example shown in Figure 3.1. The BS receives two copies of the signal from the UE: one comes through LoS, and the other is reflected from the wall. Suppose, the wavelength of the signal is $\lambda = 12$ cm (the carrier's frequency $F_c = 2.6$ GHz, which is typical for LTE systems (Wikipedia contributors, 2019b)). If the lengths of the paths differ by about 6 cm or $6 + 12 \cdot k$ cm, where $k \in \mathbb{Z}$, the two copies in superposition give a strongly attenuated signal, an effect known as a deep fading effect. A small inclination of the

wall changes the length of the reflected signal's path (dashed lines in Figure 3.1). Even if the change of the length within 12 cm, it can totally change the channel from the deep fading to the doubling of the power of the received signal. The example shows that the accurate representation of an environment is crucial for channel simulation.

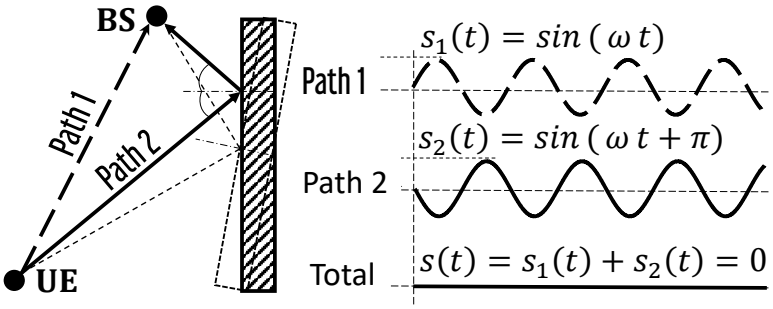

Figure 3.1: The effect of deep fading when the reflected copies of the signal in superposition give a strongly attenuated signal regardless the power of the transmitted signal. The inclination of the wall changes the reflected path.

The next section describes an approach in modeling the reflection of signals from an arbitrary inclined surface by taking into account the polarization of signals. The incorporation of Google Maps data into the simulation model validates the necessity to consider inclined walls. Simulation results show significant differences between the channel with inclined walls and the channel with vertical walls. Comparison of spherical and plane wave propagation assumptions reveals an interesting observation that the difference in channel generation under the two assumptions is small for small antenna arrays and is significant for big antenna arrays.

3.2 Specular Reflection of a Signal from an Arbitrary Inclined Surface

In this section, the model of the specular reflection of a signal from an arbitrary inclined surface is presented. For the sake of simplicity, the description is started from the consideration of a smooth surface and then extended to a rough surface. It is assumed that all reflections are modeled according to the Law of Reflection and the ray tracing approach, i.e. the angle between an incident ray and the normal vector of the reflection surface is equal to the angle between the reflected ray and the normal vector, and the reflection is proceeding in the plane perpendicular to the reflection surface. Reflections with two or more bounces are not considered because, in most practical cases, the

energy of a transmitted signal sharply drops after the second reflection according to the Fresnel coefficients of reflection (Landron *et al.*, 1996; Raschkowski *et al.*, 2015). The modeling is explained using uplink signals (from the UE to the BS as illustrated in Figure 1.8) because the reflections of uplink and downlink signals can be modeled similarly.

Notations: Throughout the thesis, I use $(\cdot)$ to denote the operation of a scalar product and $(\times)$ to represent the operation of a vector product. The operation of transpose is represented with superscript T, the operation of Hermitian transpose is represented with superscript H and **bold** notations represent vectors.

3.2.1 Reflection from an Arbitrary Plane

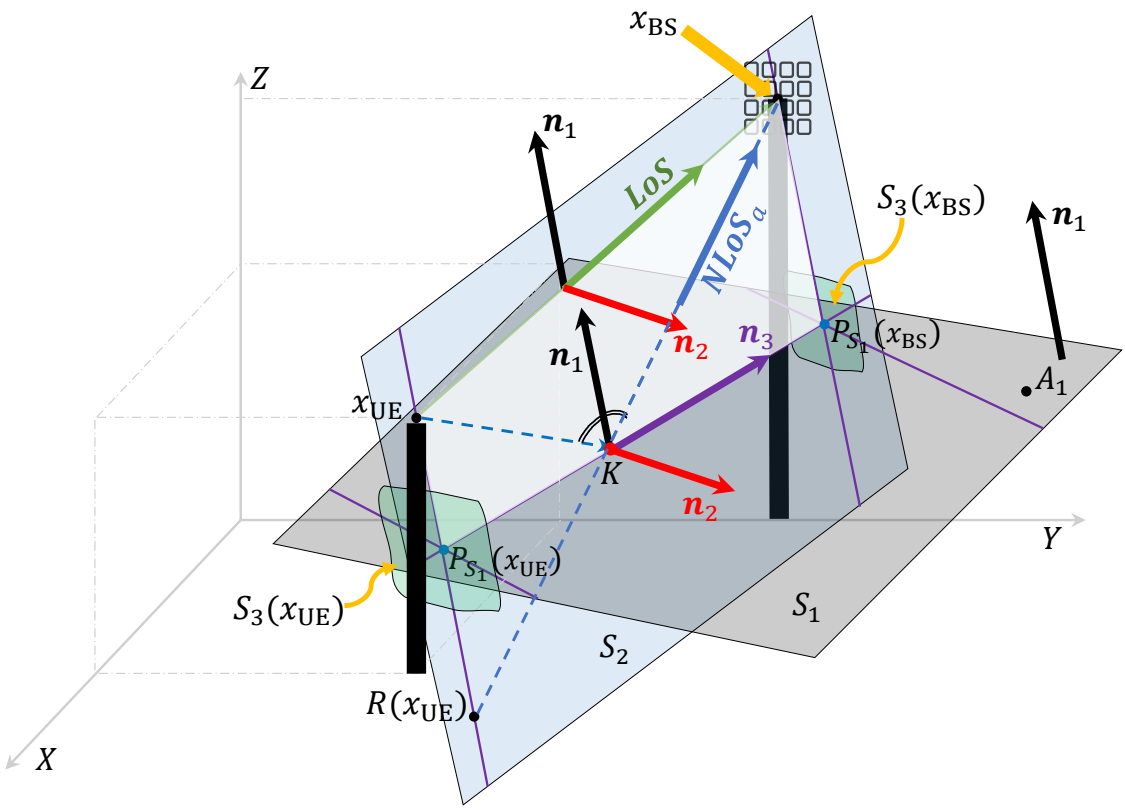

Figure 3.2: Illustration of the Law of Reflection.

As illustrated in Figure 3.2, plane S_1 is the reflection plane, plane S_2 is perpendicular to S_1, and point K is the reflection point. Suppose UE is the transmitter and BS is the receiver with antenna coordinates x_{UE} and x_{BS}, respectively.

Each plane can be defined by its normal vector and a point, through which the plane goes. In the remaining sections of this chapter, all normal vectors are assumed to be unit vectors. Suppose plane S_1 has the normal vector $\boldsymbol{n}_1 = (n_{11}, n_{12}, n_{13})^T$ and a point $A_1 = (x_1, y_1, z_1)^T$. Hence, it can be represented as follows:

$$\boldsymbol{n}_1^T \begin{pmatrix} x \\ y \\ z \end{pmatrix} - \boldsymbol{n}_1^T A_1 = 0, \quad \begin{pmatrix} x \\ y \\ z \end{pmatrix} \in \mathbb{R}^3. \tag{3.1}$$

As shown in Figure 3.2, the unit length direction vector of a LoS path can be defined as follows:

$$\boldsymbol{LoS} = \frac{x_{\mathrm{BS}} - x_{\mathrm{UE}}}{d_{LoS}}, \tag{3.2}$$

where $d_{LoS} = \|x_{\mathrm{BS}} - x_{\mathrm{UE}}\|$ is the Euclidean distance between UE and BS. Since S_1 and S_2 are perpendicular to each other and the points x_{UE}, x_{BS} and K are on S_2, the normal vector $\boldsymbol{n}_2$ of the plane S_2 is the cross product of $\boldsymbol{LoS}$ and $\boldsymbol{n}_1$, that is:

$$\boldsymbol{n}_2 = \frac{\boldsymbol{LoS} \times \boldsymbol{n}_1}{\left\|\boldsymbol{LoS} \times \boldsymbol{n}_1\right\|},$$

and plane S_2 can be defined as follows:

$$\boldsymbol{n}_2^T \begin{pmatrix} x \\ y \\ z \end{pmatrix} - \boldsymbol{n}_2^T x_{\mathrm{UE}} = 0, \quad \begin{pmatrix} x \\ y \\ z \end{pmatrix} \in \mathbb{R}^3. \tag{3.3}$$

To define the path/trajectory of the reflected signal inside S_2, two things are needed to be found. First is the intersection of planes S_1 and S_2, which is a line with the direction vector $\boldsymbol{n}_3 = \boldsymbol{n}_1 \times \boldsymbol{n}_2$, and the second is the reflection point K. For this purpose, two planes $S_3(x_{\mathrm{UE}})$ and $S_3(x_{\mathrm{BS}})$ are constructed. The planes are perpendicular to both S_1 and S_2 and going through x_{UE} and x_{BS}, respectively:

$$S_3(x_{\mathrm{UE}}): \quad \boldsymbol{n}_3^T \begin{pmatrix} x \\ y \\ z \end{pmatrix} - \boldsymbol{n}_3^T x_{\mathrm{UE}} = 0, \quad \begin{pmatrix} x \\ y \\ z \end{pmatrix} \in \mathbb{R}^3,$$

and

$$S_3(x_{\mathrm{BS}}): \quad \boldsymbol{n}_3^T \begin{pmatrix} x \\ y \\ z \end{pmatrix} - \boldsymbol{n}_3^T x_{\mathrm{BS}} = 0, \quad \begin{pmatrix} x \\ y \\ z \end{pmatrix} \in \mathbb{R}^3.$$

As illustrated in Figure 3.2, the coordinates of projections $P_{S_1}(x_{\mathrm{UE}})$ and $P_{S_1}(x_{\mathrm{BS}})$ of points x_{UE} and x_{BS} to S_1 can be found as intersections of three perpendicular planes

$$P_{S_1}(x_{\mathrm{UE}}): \quad S_1 \cap S_2 \cap S_3(x_{\mathrm{UE}})$$

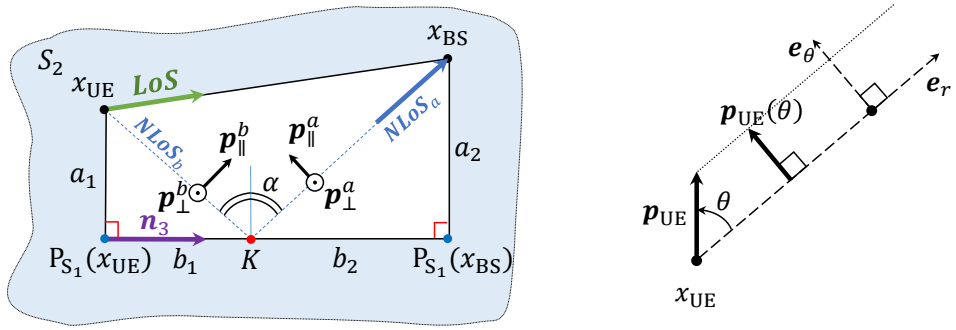

(a) (b)

Figure 3.3: (a) Reflection of the signal inside the plane S_2. (b) Polarization changes according to the observed direction $\boldsymbol{e}_r$.

and

$$P_{S_1}(x_{\mathrm{BS}}): \quad S_1 \cap S_2 \cap S_3(x_{\mathrm{BS}}).$$

Once projections $P_{S_1}(x_{\mathrm{UE}})$ and $P_{S_1}(x_{\mathrm{BS}})$ are defined, the point K can be found as illustrated in Figure 3.3(a). The point K divides the segment $[P_{S_1}(x_{\mathrm{UE}}), P_{S_1}(x_{\mathrm{BS}})]$ with length

$$d = \|P_{S_1}(x_{\mathrm{UE}}) - P_{S_1}(x_{\mathrm{BS}})\|$$

into two segments with lengths b_1 and b_2. The segments $[x_{\mathrm{UE}}, P_{S_1}(x_{\mathrm{UE}})]$ and $[x_{\mathrm{BS}}, P_{S_1}(x_{\mathrm{BS}})]$ have lengths

$$a_1 = \|x_{\mathrm{UE}} - P_{S_1}(x_{\mathrm{UE}})\| \text{ and } a_2 = \|x_{\mathrm{BS}} - P_{S_1}(x_{\mathrm{BS}})\|,$$

respectively. According to the Law of Reflection:

$$\measuredangle P_{S_1}(x_{\mathrm{UE}}) K x_{\mathrm{UE}} = \measuredangle P_{S_1}(x_{\mathrm{BS}}) K x_{\mathrm{BS}}.$$

Hence,

$$b_1 = \frac{a_1 \cdot d}{a_1 + a_2}, \quad b_2 = \frac{a_2 \cdot d}{a_1 + a_2}.$$

Finally, the coordinates of the point K can be found as

$$K = P_{S_1}(x_{\mathrm{UE}}) + b_1 \boldsymbol{n}_3.$$

The exact trajectory of the reflected signal inside S_2 is defined through the arrival and departure NLoS directions, and can be computed respectively as follows:

$$\boldsymbol{NLoS}_a = \frac{x_{\mathrm{BS}} - K}{\|x_{\mathrm{BS}} - K\|}, \quad \boldsymbol{NLoS}_b = \frac{K - x_{\mathrm{UE}}}{\|K - x_{\mathrm{UE}}\|}. \tag{3.4}$$

Here, subscript "b" indicates vectors corresponding to the signal *before* reflection and subscript "a" indicates vectors corresponding to the signal *after* reflection. As shown in Figure 3.3(a), the total distance covered by the reflected signal is:

$$d_{NLoS} = \|x_{\mathrm{BS}} - K\| + \|K - x_{\mathrm{UE}}\|. \tag{3.5}$$

The total distance also can be calculated as follows:

$$d_{NLoS} = \|x_{\mathrm{BS}} - R(x_{\mathrm{UE}})\|, \tag{3.6}$$

where $R(x_{\mathrm{UE}})$ is the position of the reflected image of the UE about to plane S_1 as illustrated in Figure 3.2. The coordinates of the image can be represented as follows:

$$R(x_{\mathrm{UE}}) = x_{\mathrm{UE}} - 2(x_{\mathrm{UE}} - P_{S_1}(x_{\mathrm{UE}})), \tag{3.7}$$

which also has another well-known Householder transformation representation (Householder, 1958):

$$R(x_{\mathrm{UE}}) = x_{\mathrm{UE}} - 2\boldsymbol{n}_1 \left(\boldsymbol{n}_1^T \left(x_{\mathrm{UE}} - A_1\right)\right). \tag{3.8}$$

3.2.2 Perpendicular and Parallel Components of Polarization

The polarization of a signal is defined by the direction of its electric field, which is perpendicular to the direction of signal propagation (Orfanidis, 2014). However, a signal is transmitted from an antenna, and consequently the transmitting antenna defines the polarization of the transmitted signal. The nature of electromagnetic signal polarization is a complex concept in terms of physics. A more detailed discussion is presented in Chapter 5. Roughly speaking, the polarization of a transmitted signal can be defined by the orientation of the transmitting antenna element, which converts electric current to electromagnetic waves and vice-versa. Here, orientations of UE and BS antennas are defined as unit vectors $\boldsymbol{p}_{\mathrm{UE}}$ and $\boldsymbol{p}_{\mathrm{BS}}$, respectively. As illustrated in Figure 3.3(b), if a transmitted signal is observed in direction $\boldsymbol{e}_r$, then the polarization $\boldsymbol{p}_{\mathrm{UE}}(\theta)$ of the signal is defined as projection of $\boldsymbol{p}_{\mathrm{UE}}$ to $\boldsymbol{e}_\theta$ and calculated as follows:

$$\boldsymbol{p}_{\mathrm{UE}}(\theta) = \boldsymbol{e}_\theta \left(\boldsymbol{e}_\theta^T \boldsymbol{p}_{\mathrm{UE}}\right). \tag{3.9}$$

Eqn. (3.9) holds for the Hertzian dipole antenna model, and the expression can be different for other antenna models (Orfanidis, 2014). It means that the observation in direction $\boldsymbol{e}_r$ causes additional attenuation of the reception. Here, vector $\boldsymbol{e}_\theta$ is perpendicular to $\boldsymbol{e}_r$ and parallel to the plane generated by $\boldsymbol{p}_{\mathrm{UE}}$ and $\boldsymbol{e}_r$. Note, $\boldsymbol{e}_r$ and $\boldsymbol{e}_\theta$ are unit vectors.

An antenna element creates a heterogeneous electric field around itself. Depending on the observed direction $\boldsymbol{e}_r$ relative to the antenna element, the observed signal can have different polarization. The vector function of the relation between an observed direction $\boldsymbol{e}_r$ and the vector of the observed polarization is denoted as $\boldsymbol{F}(\theta, \varphi)$ (Narandzic *et al.*, 2007; Orfanidis, 2014; Sinclair, 1950), where θ and φ are spherical coordinates of $\boldsymbol{e}_r$ relative to the antenna element's coordinate system, as illustrated in Figure 3.4 in the case of $\boldsymbol{p}_{\mathrm{UE}}$. This means that if a signal is observed in direction $\boldsymbol{e}_r$ with the spherical coordinates θ and φ, then the polarization of the signal is expressed as $\boldsymbol{p} = \boldsymbol{F}(\theta, \varphi)$.

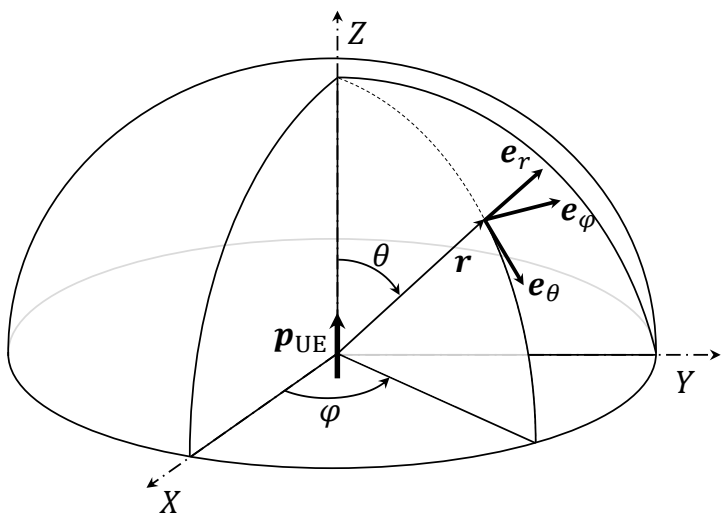

Figure 3.4: Spherical coordinates relative to the antenna coordinate system.

Let us define angle θ_b that represents angle between $\boldsymbol{p}_{\mathrm{UE}}$ and $\boldsymbol{NLoS}_b$. As illustrated in Figure 3.3(a) and Figure 3.2, in the case of reflection, the transmitted signal interacts with plane S_1 at point K and its polarization vector $\boldsymbol{p}_{\mathrm{UE}}(\theta_b)$ is decomposed into the perpendicular component:

$$\boldsymbol{p}_{\perp} = \left(\boldsymbol{p}_{\mathrm{UE}}(\theta_b)^T \boldsymbol{n}_2\right) \boldsymbol{n}_2, \tag{3.10}$$

and parallel component:

$$\boldsymbol{p}_{\parallel} = \left(\boldsymbol{p}_{\mathrm{UE}}(\theta_b)^T \left(\boldsymbol{n}_2 \times \boldsymbol{NLoS}_b\right)\right) \left(\boldsymbol{n}_2 \times \boldsymbol{NLoS}_b\right), \tag{3.11}$$

relative to S_2. Since $\boldsymbol{NLoS}_b$ and $\boldsymbol{n}_2$ are unit length perpendicular vectors, their vector product defines a unit length vector that is perpendicular both of them (Gel'fand, 1989). Note, that $\left(\boldsymbol{p}_{\mathrm{UE}}(\theta_b)^T \boldsymbol{n}_2\right)$ and $\left(\boldsymbol{p}_{\mathrm{UE}}(\theta_b)^T \left(\boldsymbol{n}_2 \times \boldsymbol{NLoS}_b\right)\right)$ define the lengths of perpendicular and parallel projections of polarization vector $\boldsymbol{p}_{\mathrm{UE}}(\theta_b)$ to plane S_2, correspondingly. Let us note these lengths as $p_{\perp}$ and $p_{\parallel}$, respectively.

The decomposed components are attenuated in accordance with the Fresnel reflection coefficients $\Gamma_\perp$ and $\Gamma_\parallel$, which depend on the angle of an incident ray and the material of the surface (Raschkowski *et al.*, 2015; Landron *et al.*, 1996). In addition to the attenuation, the parallel component of the polarization has to be rotated to become perpendicular to $\boldsymbol{NLoS}_a$. Hence, the polarization of the reflected signal can be expressed as follows:

$$\boldsymbol{p}_{ref} = \Gamma_\perp \boldsymbol{p}_\perp + \Gamma_\parallel \, p_\parallel \, (\boldsymbol{n}_2 \times \boldsymbol{NLoS}_a). \tag{3.12}$$

This equation shows that the reflection changes the polarization of a signal, and the result of the change is inextricably linked with the value of the inclination of the reflecting surface. The final attenuations caused by polarization transformations for LoS and NLoS directions can be calculated as follows:

$$G_{LoS} = \boldsymbol{p}_{\mathrm{UE}}(\theta)^T \, \boldsymbol{p}_{\mathrm{BS}}, \quad G_{NLoS} = \boldsymbol{p}_{ref}^T \, \boldsymbol{p}_{\mathrm{BS}}, \tag{3.13}$$

where θ is angle between $\boldsymbol{p}_{\mathrm{UE}}$ and $\boldsymbol{LoS}$ direction, Figure 3.3.

3.2.3 Extension to a Rough Surface

In the case of a rough surface, the energy of the specularly reflected signal is reduced due to the scattering effect (Ament, 1953). The energy of an incident signal is scattered in multiple directions instead of the direction of specular reflection. According to the Rayleigh criterion (Landron *et al.*, 1996), a surface is considered to be rough if the difference h between the minimum and maximum heights of a surface is higher than the critical height h_c that can be calculated as follows:

$$h_c = \frac{\lambda}{8 \cdot \cos\alpha}, \tag{3.14}$$

where α is the angle between the incident ray and the normal vector of a surface, as shown in Figure 3.2. The attenuation coefficient ρ_s of the reflected signal caused by a rough surface is given by

$$\rho_s(\alpha) = \exp\left[-8 \cdot \left(\frac{\pi \cdot \sigma_h \cdot \cos\alpha}{\lambda}\right)^2\right], \tag{3.15}$$

where σ_h is the standard deviation of the surface's height.

3.3 Simulation of massive MIMO Reception

In this section, the signal reception at the massive MIMO BS side is modeled. In order to compare the channel generation results of different channel models constructed on

Figure 3.5: Close range observation of the Gates of Europe. The walls of the buildings are not ideally flat. The roughness effect has to be considered in channel generation.

the PWP and SWP assumptions, it is worth to give a description of the simulating of the massive MIMO reception under the two assumptions. The section starts with the explanation of the antenna elements sorting according to the receiving sequence under the assumption of plane waves. Then the calculation of time differences between signal reception of different antenna elements is developed. The section ends with the extension of the channel model to spherical waves.

As illustrated in Figure 3.6(a), it is assumed that the antenna is deployed in a plane perpendicular to the O_x axis, and the normal vector of that plane is represented by unit vector $\boldsymbol{n}_{\mathrm{BS}}$. Vector $\boldsymbol{v}_a$ denotes the direction of an arrived signal ($\boldsymbol{LoS}$ or $\boldsymbol{NLoS}_a$). The angle between arrived signal $\boldsymbol{v}_a$ and $\boldsymbol{n}_{\mathrm{BS}}$ is denoted as Θ, and the angle between axis O_z and the projection of $\boldsymbol{v}_a$ to plane O_{yz}, which is $P_{yz}(\boldsymbol{v}_a)$, is denoted as Φ. The cosines of both angles Θ and Φ can be calculated as follows:

$$\cos\Theta = -\boldsymbol{n}_{\mathrm{BS}}^T\,\boldsymbol{v}_a, \quad \cos\Phi = \frac{\boldsymbol{e}_z^T\,P_{yz}(\boldsymbol{v}_a)}{\|P_{yz}(\boldsymbol{v}_a)\|},$$

where $\boldsymbol{e}_z$ is the direction vector of the O_z axis.

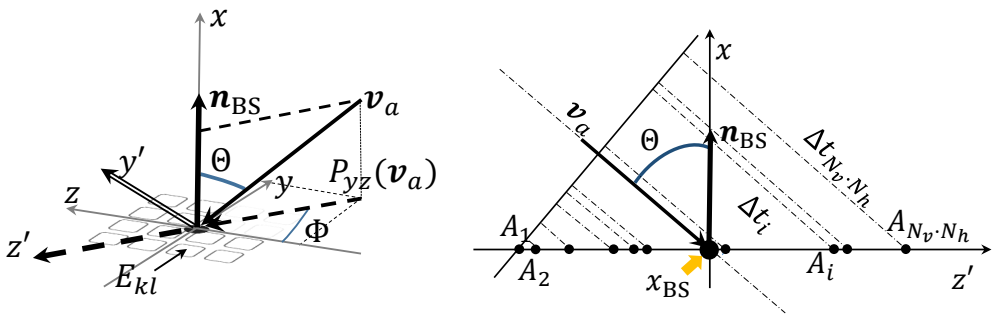

(a) (b)

Figure 3.6: (a) The geometry of an antenna array. (b) Calculation of time delays according to the receiving sequence.

3.3.1 Sorting Antenna Elements

The coordinates of antenna elements are denoted as Elm_{kl} $(k = 1, \ldots, N_v, l = 1, \ldots, N_h)$, where N_v and N_h are the numbers of vertical and horizontal elements, and $N = N_v \cdot N_h$. As illustrated in Figure 3.6(a), signal $\boldsymbol{v}_a$ first reaches the bottom right element and then all other elements sequentially. To know the sequence in which the elements receive the signal, sorting of all elements is needed to be done. The sorting of the elements should be done according to their positions relative to the new axis $O_{z'}$, which is defined by rotating O_z with angle Φ. For this purpose, old coordinate system O_{yz} needs to be rotated counterclockwise with angle Φ to obtain the new coordinate system $O_{y'z'}$. After the rotation, coordinates in the new system can be found using the following equation:

$$\begin{pmatrix} y' \\ z' \end{pmatrix} = \begin{pmatrix} \cos\Phi & \sin\Phi \\ -\sin\Phi & \cos\Phi \end{pmatrix} \begin{pmatrix} y \\ z \end{pmatrix}. \tag{3.16}$$

As illustrated in Figure 3.6(b), elements Elm_{kl} can be sorted in ascending order relative to z' coordinate, and the resulting set can be noted as $A_i, i = 1, \ldots, N_v \cdot N_h$.

3.3.2 Calculation of Time Differences

As illustrated in Figure 3.6(b), the signal first reaches element A_1, then A_2, and etc. d_{12} denotes the Euclidean distance between elements A_1 and A_2 in z' coordinates. To reach element A_2 after A_1, the arrived signal spends time Δt_2, which can be calculated as:

$$\Delta t_2 = \frac{d_{12} \cdot \sin\Theta}{c},$$

where c is the speed of light. Hence, the time spent by the signal to reach point A_i can be calculated as:

$$\Delta t_i = \frac{d_{1i} \cdot \sin \Theta}{c},$$

where d_{1i} is Euclidean distance between A_1 and A_i in z' coordinates.

3.3.3 Spherical Wave Propagation

Under the SWP assumption (Raschkowski *et al.*, 2015), each element of the antenna has its own LoS and NLoS directions. The calculation of the directions, interactions, and attenuations have to be performed separately for each element, i.e. all steps from Section 3.2 have to be done for each antenna element. It is clear that the modeling of SWP-based channels is computationally more complex than PWP-based channels. For example, for a SWP channel model, if a UE has M antennas and the serving BS has N antennas, then all steps from Section 3.2 have to be calculated $M \times N$ times for each communicating pair. On the other hand, the PWP assumption requires calculating steps from Section 3.2 only M times because antennas of the BS are not distinguishable for the channel in terms of angles of arrival. Thus, for each UE's transmitting antenna, propagation paths and signal's interactions with the environment have to be derived just for one antenna of the BS. Thus, for each UE's transmitting antenna, propagation paths and signal's interactions with the environment have to be derived just for one antenna of the BS. Other antennas will have the same paths, same attenuations, and same polarization change – the only difference in reception time, which is defined by the direction of arrival. However, in the case of spherical waves, generated channels become more spatially consistent and enable many new opportunities for signal processing algorithms. Hence, spatial consistency becomes the payment for the accepted computational complication.

3.4 Simulations

To validate the proposed solution in terms of modeling reflections from an arbitrary surface, a simulation model in MATLAB has been implemented and LTE uplink transmission has been simulated (Sesia *et al.*, 2011; Cho *et al.*, 2010).

3.4.1 Simulation Setup

The carrier's frequency F_c is set to 2.6 GHz, which is typical for LTE systems (Wikipedia contributors, 2019b). In order to examine the channel behavior on the whole bandwidth of Uplink, the maximum bandwidth in 100 resource blocks is allocated to one UE, where each resource block has 12 subcarriers with each having a bandwidth of 15 kHz (Sesia *et al.*, 2011). The simulation includes one UE and one BS. The UE has one antenna element, whereas the number of antenna elements in BS is varied from 1 to 100. Each element receives a multipath signal mixed with additive white Gaussian noise with 15 dB of SNR. The distance between the neighboring antenna elements on the massive MIMO antenna array is configured to be half of the wavelength $\Delta d = \lambda/2 \approx 6$ cm (Orfanidis, 2014). The BS's antennas have vertical orientation $\boldsymbol{p}_{\mathrm{BS}}$, while antenna orientation $\boldsymbol{p}_{UE}$ of the UE can be configured with three options: (1) Horizontal, (2) Vertical, and (3) Inclined with 45-degree.

Environment Setup

Figure 3.7 illustrates the environment's model that is constructed based on the Gate of Europe area in Spain. The information about the area has been obtained from Google maps (Figure 2.2). The geometrical characteristics of the buildings are obtained from Wikipedia. The height of the buildings is 114 meters, and the angle of inclination is 15 degrees for both towers. The height of BS antenna is set to be 30 meters, and UE is 1.9 meters (probably Michael Phelps, the most decorated Olympian of all time (Wikipedia contributors, 2019a)).

In order to evaluate the influence of inclined surfaces and spherical waves to the channel generation, both types of waves (plane and spherical) are examined and the following three environment setups are used, as illustrated in Figure 3.8: (1) *Inclined walls* (the real inclination of towers with 15 degrees), (2) *Vertical walls* (no inclination for the two towers), and (3) *Displaced walls* (the inclination degree is set to be 1 degree). Figure 3.7 shows both the LoS path and the NLoS paths caused by the reflections from the inclined walls, and the ground.

The Effect of Wall Roughness

Based on the street view from Google maps (using street view in Google maps), it can be seen that the most part of the surface of the buildings is covered by a glass material and the floor under the UE is made from concrete. As illustrated in Figure

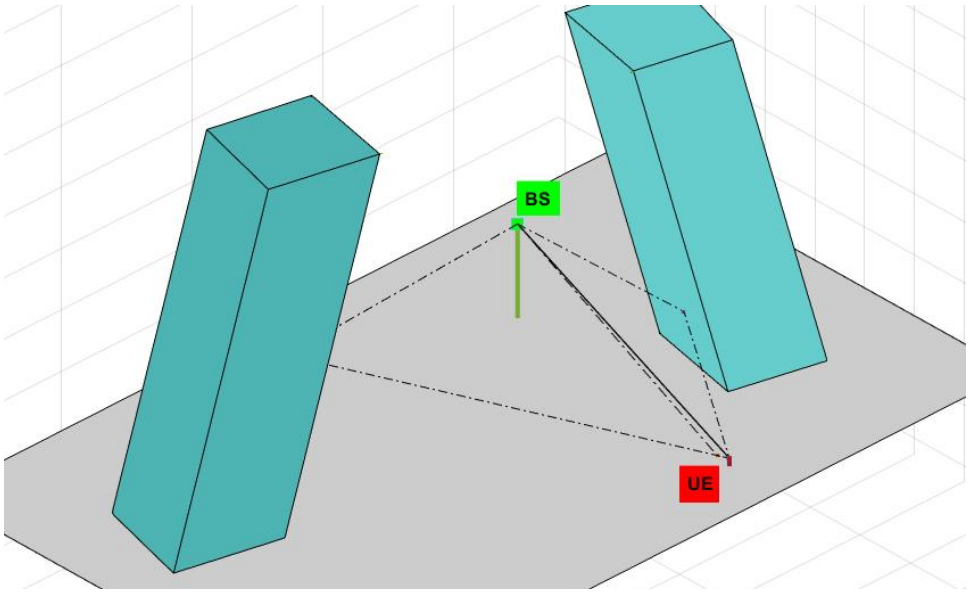

Figure 3.7: The model of the Gate of Europe. The solid line is the LoS, and the dash-doted lines represent reflections from inclined walls.

3.5, the gray straight elements on the surfaces make the walls rough. It is assumed that the gray elements stick out from the main surface with $h_{\max} = 0.2$ meters, which is higher than the critical value of the roughness h_c given in Eqn. (3.14) for all angles of incidence θ from 0° to 86°. In the performed simulation, angles of reflection are smaller than 86°. Hence, the walls are considered as rough, and the attenuation coefficient given in Eqn. (3.15) is used. From the street view, it can be roughly estimated that the percentage of gray elements is around 25% of the surface, which results in standard deviation $\sigma_h = 0.08$ m.

Calculation of Reflection and Penetration Coefficients

All the physical parameters of materials and the equations used for calculating the Fresnel coefficients of reflection are used in accordance to the METIS report (Raschkowski *et al.*, 2015), and set as follows: (1) Glass material: relative permittivity $\varepsilon_r' = 7.0$, and conductivity $\sigma = 0.25$; (2) Concrete material: $\varepsilon_r' = 5.31$, and $\sigma = 0.0707$. The Fresnel coefficients are calculated as follows:

$$\Gamma_{\perp}(\theta) = \frac{\cos\theta - \sqrt{\varepsilon_r - \sin^2\theta}}{\cos\theta + \sqrt{\varepsilon_r - \sin^2\theta}}, \tag{3.17}$$

$$\Gamma_{\parallel}(\theta) = \frac{\varepsilon_r \cdot \cos\theta - \sqrt{\varepsilon_r - \sin^2\theta}}{\varepsilon_r \cdot \cos\theta + \sqrt{\varepsilon_r - \sin^2\theta}}, \tag{3.18}$$

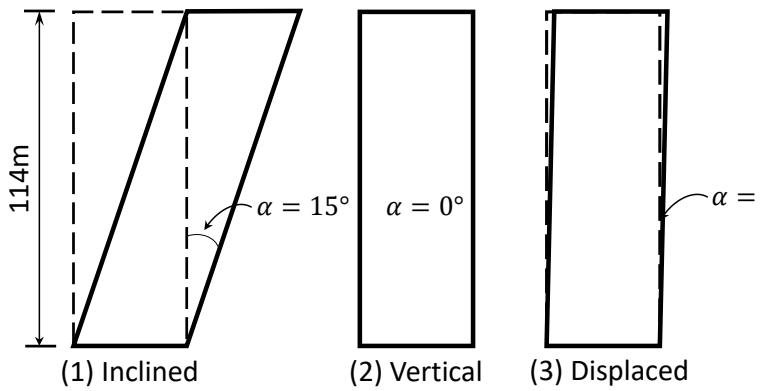

Figure 3.8: The considered three scenario with different angles of inclination.

and the complex relative permittivity of the material is represented as

$$\varepsilon_r = \varepsilon_r' - j \cdot 17.98 \cdot \sigma / f, \tag{3.19}$$

where j is the imaginary unit, and f is the frequency in GHz. In the simulation, $f = 2.6$.

It is also assumed that the LoS and the reflected from the concrete floor propagation paths are blocked by a human body. This consideration adds flexibility in the channel generation. It is always beneficial to have such kind of scenarios. The physical parameters of a human's body are: $\varepsilon_r' = 2.97$ and $\sigma = 0.0116 \cdot f^{0.7076}$. The penetration coefficient through a human body is calculated as follows:

$$T_h = \frac{(1 - \Gamma_h^2) \cdot \exp(-j \cdot (\delta - \frac{2\pi}{\lambda} \cdot d_h))}{1 - \Gamma_h^2 \cdot \exp(-j2\delta)}, \tag{3.20}$$

where

$$\delta = \frac{2\pi}{\lambda} \cdot \sqrt{\varepsilon_r},$$

d_h is the thickness of the human's body (0.6 m in the simulation), and Γ_h means Fresnel coefficient for the perpendicular and parallel components of a signal, which are calculated based on Eqn. (3.17) and Eqn. (3.18), respectively. In the case of human body penetration, the antenna of the UE is close enough to the human's body that angle of incident $\alpha = 0$.

Free Space Path Loss and Attenuation Coefficients

Since the main aim is to examine the effect of reflection from inclined walls, a simple model of free space path loss has been used

$$PL(d) = \frac{\lambda}{4\pi d}, \tag{3.21}$$

where d is the distance covered by a signal. The attenuation coefficients for each propagation path are calculated separately as follows based on equations (3.13), (3.15), (3.20), (3.21):

- LoS path

$$K_{LoS} = G_{LoS} \cdot T_h \cdot PL(d_{LoS}); \tag{3.22}$$

- NLoS path reflected from the floor

$$K_{floor} = G_{NLoS}^{concrete} \cdot T_h \cdot PL(d_{floor}); \tag{3.23}$$

- NLoS paths reflected from the walls

$$K_{NLoS} = \rho_s \cdot G_{NLoS}^{glass} \cdot PL(d_{NLoS}). \tag{3.24}$$

Here, $G_{NLoS}^{material}$ is the attenuation coefficient caused by polarization change in the dependency on the considered material.

3.4.2 Simulation Results

In this section, the results of channel response based on LTE uplink channel estimation procedure are presented (Mai *et al.*, 2007). As the channel measurements are noisy, the measurements are averaged using a sliding window with length of 10 samples.

Scenario I (One Reflecting Surface)

To evaluate the correctness of the simulation approach, the channel modeling methodology has been tested in a simple scenario with only one reflecting surface, which is the concrete floor. In this scenario, the BS observes two incoming signals: a LoS signal and a reflected from the concrete floor signal. Intuitively, it is anticipated that the power of the received signal should be higher if the antennas (UE and BS) have the same orientation and should be lower when the orientations are perpendicular to each other, i.e. the UE has a horizontal orientation. For 45 degrees of inclination of the UE's orientations, the resulting channel response should be between the two channel responses when the UE has vertical and horizontal orientations. As illustrated in Figure 3.9, this intuition is well followed: the black lines represent the situation when both antennas have the same orientation, the blue lines represent the situation when the orientation of the UE is inclined on 45 degrees relative to the vertical axis, and the red lines represent the situation when the orientation of the UE is horizontal. This indicates that, by

changing the receiver's/transmitter's antenna orientation, the connection quality can be improved. Since the UE is not located in the direction perpendicular to the antenna panel of the BS, the polarization of the transmitted signal is changing through LoS and NLoS paths. Hence, the BS can receive nonzero signals from the UE even if it has a horizontally oriented antenna.

In this simulation, it can be observed that the more the number of antenna elements at the BS, the stronger the received signal strength, which is consistent with the massive MIMO purposes. Another observation is that the discrepancy between the channels generated under the PWP and SWP assumptions grows with the number of antenna elements. This is caused by the fact that the distance between two maximally distanced antenna elements within an antenna array increases with the increase of the number of antenna elements. When the number of elements is small, spherical waves can be accurately approximated by plane waves because the difference between these waves is minuscule. However, for a massive MIMO with a big number of antennas, the difference in receiving signal power for elements that are far away from each other is large. Hence, the approximation of spherical waves by plane waves becomes rough, which has a big influence on the generation of wireless channels. This effect is well observed in Figure 3.9: for four antenna elements, the spherical and plane channels are very close; for 16 elements the channels begin to differ and the discrepancy becomes significant for 100 elements. For example, in this particular scenario, the average difference is about 1 dB, and for other scenarios with multiple reflecting surfaces the difference could be even larger.

Scenario II (the Gate of Europe)

The main aim of this scenario is to show the importance of consideration of inclined surfaces in simulations. The channel responses in the three setups given in Section 3.4.1 are compared. The displaced walls are simulated to show that even a small inclination can have a significant impact on the channel behavior. The orientations of the BS antennas are vertical, and the UE has 45-degree antenna inclination.

As illustrated in Figure 3.10, the black lines represent the model with inclined walls, the blue lines represent the model with vertical walls, and the red lines represent displaced walls. The thin lines mean that the channels are generated under the spherical waves propagation assumption, and the thick lines mean that the channels are generated under the plane waves propagation assumption. For the sake of simplicity, they are referred to as spherical channels and plane channels, respectively. As shown in

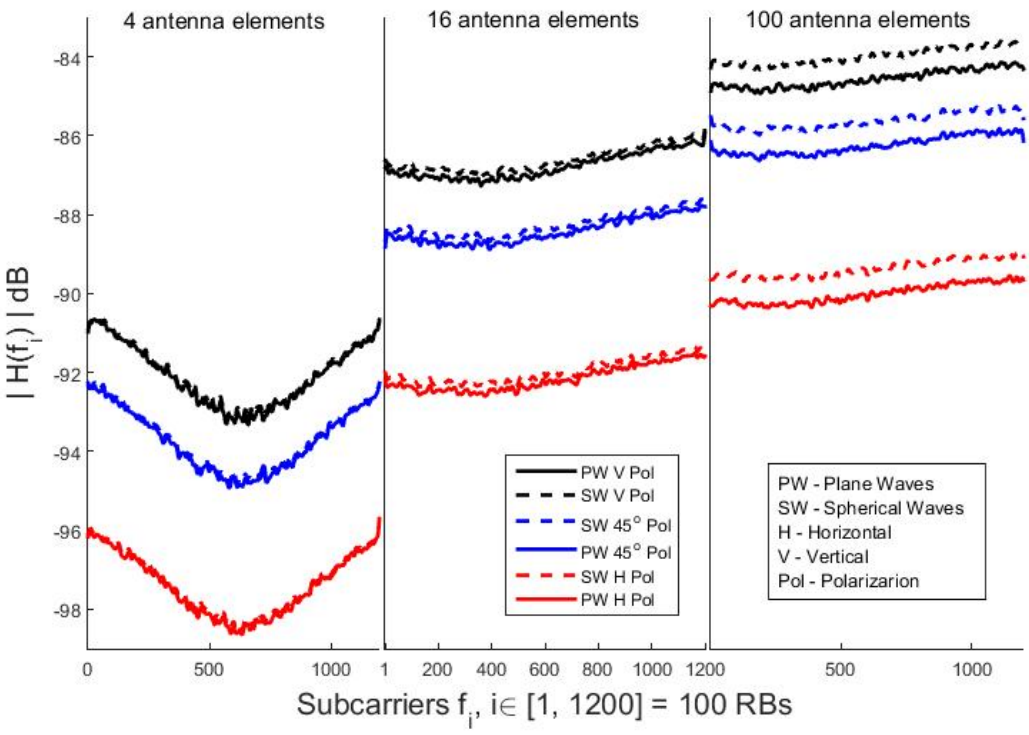

Figure 3.9: The impact of orientations of communicating antennas; different types of waves, and different number of antenna elements at the BS. Orientation $\boldsymbol{p}_{\mathrm{UE}}$ has three states: vertical, horizontal, and 45°. The number of the BS's antenna elements varies between 4, 16 and 100 elements with all elements having a vertical orientation.

Scenario I, the difference between channels generated by spherical and plane waves is small when the number of antenna elements is small. It can be seen from Figure 3.10 that, for four antenna elements, the difference between spherical and plane channels is less than 0.3 dB. Moreover, all three models generate channels close to each other, and the maximum discrepancy is less than 1.4 dB. This indicates that it is feasible to use plane waves to simulate multipath channel for antennas with a small number of antenna elements.

With the increase of the number of antenna elements, the difference between generated channels becomes significant. For 16 elements, the maximum difference between the channels with inclined walls and with vertical walls is around 8 dB. The models with vertical and displaced walls generate similar channels, and the difference between them is less than 2 dB. An interesting observation is that the spherical channel and the plane channel are very close in the model with inclined walls, while they are significantly different in the other models. For example, the difference for inclined walls

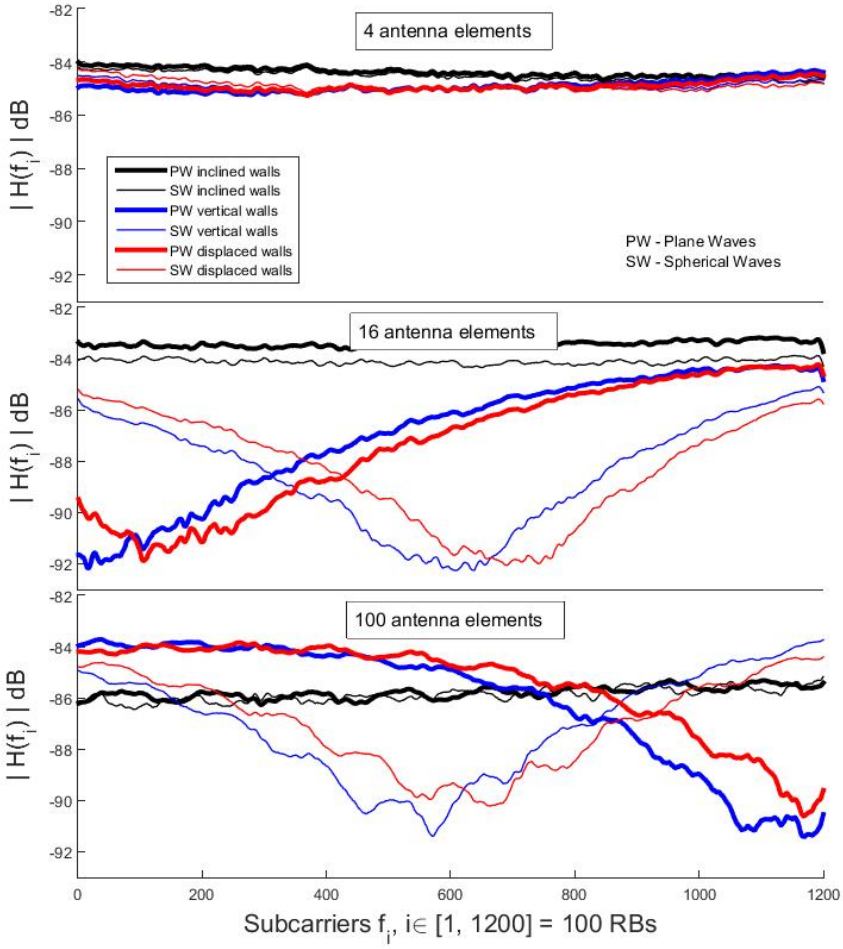

Figure 3.10: The impact of the number of antenna elements and different types of wave propagation models in the Gate of Europe scenario. The BS has vertically oriented antennas, and the UE has 45° antenna inclination. The number of antenna elements varies between 4, 16 and 100.

is less than 1 dB, while the difference for vertical/displaced walls is up to 6 dB. In the case of 100 elements, the channels with vertical walls and displaced walls start to differ up to 3 dB, which can be vital for the LTE procedures such as signal equalization, demodulation, decoding, and etc. These results indicate that massive MIMO systems are more sensitive to the accurate environment representation and they require very accurate and realistic channel models.

3.5 Conclusion

In this chapter, the steps on the modeling of wireless signal propagation for massive MIMO systems are described. The primary focus of the modeling is put into the description of the reflection phenomenon from arbitrarily inclined surfaces since, in practice, the majority of objects within the surrounding environment has sloped surfaces. The analyzed example from the simulation part shows the ability of the modeling approaches taking into account and handling any realistic environment. The simulation results indicate that inclined surfaces can have a significant influence on the channel generation in comparison with vertical surfaces due to the difference in propagation paths, angles of reflection, and polarization transformations of electromagnetic waves. Further, the difference between spherical and plane waves assumptions has been examined regarding the channel generation. It is seen that, for the MIMO antennas with a large number of antenna elements, the difference between the channels with spherical waves and plane waves is significant. Hence, by default, all the further discussions in further chapters regarding the channel modeling use the spherical wave propagation assumption.

Chapter 4

User Localization

This chapter describes the solution to localize users at the massive MIMO BS side using only uplink signals and by taking the advantages of the sphericity of the incoming wavefronts.

4.1 Introduction

In most existing beamforming schemes, beams are created based on the estimation of the DL channels via reference signals, which brings large overhead to DL data communications. For example, to maintain 25 UEs, the per-antenna reference signals used to measure the DL channels for a BS with 100 antenna elements consume more than 50% of the traffic generated by the BS (Björnson *et al.*, 2016). Recently, it has been demonstrated in (Vasisht *et al.*, 2016; Han *et al.*, 2018) that, with information on UE locations, accurate beamforming can be performed without any channel feedback overhead. Hence, it is worth developing accurate UE localization schemes to support efficient beamforming in massive MIMO systems.

Limitations of existing works: Existing GPS-based solutions cannot provide precise locations for accurate beamforming using the commodity mobile devices, especially in dense urban areas. Moreover, the location information is available at the user side instead of the BS. To use location information for beamforming, the BS has to frequently pull it for the UEs, which is energy consuming. Several schemes (Vasisht *et al.*, 2016, 2015; Kumar *et al.*, 2014) have been proposed to locate UEs using LTE UL signals based on the reference symbols carried in data communication. However, such schemes can locate UEs only after radio resources have been allocated. If the UEs can be located before radio resource allocation, the location information can be immediately

used to optimize resource allocation and beamforming. Another limitation of existing schemes is the lack of consideration for phase noise caused by non-ideal synchronization between antenna elements, which can significantly deteriorate the accuracy of UE localization (Yang *et al.*, 2014).

Challenges: The first challenge is to accurately estimate the distance between each antenna element in the massive MIMO antenna array and the UE without the need of precise time synchronization between UEs and the BS. Due to the use of the SWP assumption, the difference in time delay experienced at different antenna elements can be described through small phase shifts between the BS's antenna measurements. In case there is a single dominant LoS path to each antenna element, the phase shifts can be obtained by analyzing the angles of the RACH correlation spikes that are already computed during the RACH procedure (Sesia *et al.*, 2011; Fedorov *et al.*, 2015). In case there are multiple communication paths, the proposed scheme leverages the OFDM nature of RACH signals to obtain more measurements for a joint estimation of the shapes of all the incoming wavefronts via a nonlinear data-fitting approach.

The second challenge is to deal with the phase noise caused by non-ideal synchronization between massive MIMO antenna elements. Even though all antenna elements at a BS are synchronized using a reference clock (Malkowsky *et al.*, 2017), there are still small phase deviations, which can have a big impact on the estimation of the wavefront shape of the incoming signals. Using the Otago University massive MIMO testbed that consists of two Ettus USRPs N210 and one 10 MHz reference NI OctoClock, the phase noise between the two USRPs has been measured. According to the measurements campaign, the phase noise cannot be simply approximated by Gaussian noise. Instead, stochastic properties for the measured phase noise have been estimated via a system identification approach. Due to the incorporation of the stochastic properties of the phase noise to the localization procedure, the harmful impact of the phase noise has been successfully eliminated.

Contributions: Existing localization schemes are designed based on the assumption of PWP, which is not realistic for massive MIMO due to the increased antenna array size. Since real wireless signals propagate spherically and massive MIMO antenna arrays can recognize the sphericity of incoming waves, it is worth to take the advantages of the spherical propagation. The main advantage of the spherical propagation is that the captured by a massive MIMO BS piece of a wavefront belongs to a sphere. Consequently, the center of the sphere is the position of the signal source, which is the antenna position of a communicating UE. Hence, the sphere that fits the incoming

wavefront shape automatically infers the location of the UE. This advantage is used in the proposed localization algorithm.

In this dissertation, the architecture of LTE signals is used in the development of localization algorithms since the core of 5G signals will be adopted from LTE, at least the OFDM structure will be kept in 5G (Venkatesan and Valenzuela, 2016; Zaidi *et al.*, 2016). In LTE, communication between a UE and a BS starts from the RACH synchronization procedure where the UE broadcasts special signals to indicate its intention to connect to the BS's network. Two solutions are proposed to localize UEs based on RACH signals in both single-path and multi-path propagation environments. The first solution is suitable for a single-path LoS communication case and based on the Bancroft algorithm that utilizes relative phase shifts of the RACH correlation spikes to find the UE's location. The second solution is based on a nonlinear data-fitting approach that exploits the OFDM nature of RACH signals to jointly estimate the parameters of spheres of all the incoming wavefronts. Since UE locations are obtained based on RACH signals, the proposed schemes enable the BS to get the location of a connecting UE before allocating radio resource to it, thereby enabling the use of UE locations to optimize radio resource allocation and perform accurate beamforming.

The chapter also provides the evaluation of the proposed schemes through both simulations and a proof-of-concept experiment. Simulation results show that the single-path solution can provide a decimeter-level localization accuracy for massive MIMO with 64 or more antennas within the region of 100 meters and a sub-meter-level localization accuracy for massive MIMO with 80 or more antennas up to 300 meters. For the multipath solution, the same results can be achieved using massive MIMO with no less than 48 antenna elements. The single-path solution has been implemented and evaluated on the testbed by emulating MIMO systems with 8, 12 and 16 antenna elements. The results of the proof-of-concept experiments justify the feasibility of the proposed approach.

4.2 Background on LTE RACH Synchronization

To connect to an LTE network, a UE has to perform the RACH synchronization procedure by sending a RACH signal (i.e. preamble) to a network BS (Sesia *et al.*, 2011). For this purpose, the UE randomly selects a RACH preamble from the assigned list of available preambles, which is also known at the BS side, and sends it, as illustrated in Figure 4.1. Once the preamble reaches the BS, the correlations between the incoming

signal and the local preambles from the assigned list are calculated. If the incoming signal matches with a preamble in the assigned list, a correlation spike occurs. By detecting the correlation spike, the BS distinguishes the exact preamble used by a UE and estimates its time delay.

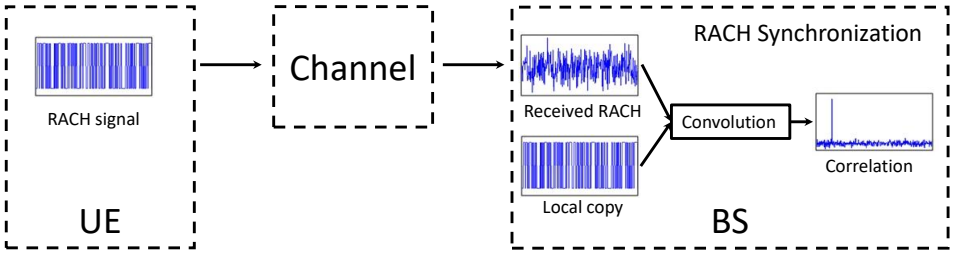

Figure 4.1: Procedure of RACH synchronization.

The robustness of RACH synchronization is provided by the good self- and mutual-orthogonal properties. RACH preambles are generated from the Zadoff-Chu (ZC) sequences (Chu, 1972), which have a constant amplitude and zero autocorrelation waveforms. In the time domain, a root ZC sequence is defined as follows:

$$zc_u(l) = e^{-j\frac{\pi u l(l+1)}{N_{ZC}}}, \tag{4.1}$$

where $N_{ZC} = 839$, $l = 0, \ldots, N_{ZC} - 1$, and the root index u is a prime number less than N_{ZC}. Other sequences can be generated by cyclically shifting the root sequence. The time domain sequence is then converted to $ZC(k)$ in the frequency domain via an 839 points discrete Fourier transform (DFT), as illustrated in Figure 4.2.

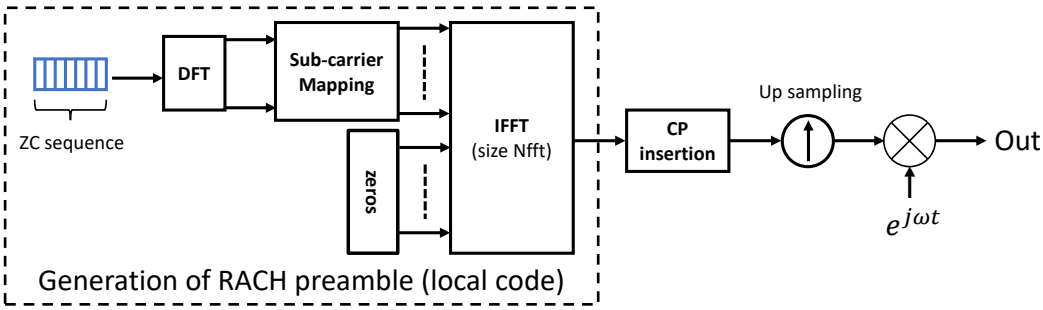

Figure 4.2: RACH signal generation.

To generate a RACH signal in the time domain, the 839 elements of $ZC(k)$ are mapped to the assigned OFDM subcarriers in the frequency domain and then converted to the time domain via a 1024 points inverse fast Fourier transform (IFFT). The UE

performs upsampling of the obtained RACH signal in order to mix with the carrier waveform and transmits the upsampled RACH signal to the BS. The sampling rate of the transmitted RACH signal becomes equivalent to the conventional sampling rate of the LTE system (Sesia *et al.*, 2011). The reverse steps are done at the BS side starting from removing carrier waveform and downsampling to extract the ZC sequence at a lower sampling rate in the digital time domain, as illustrated in Figure 4.3. The extracted signal actually contains all the information about the channel through which it has been transmitted. This channel information can be used to find the location of the UE.

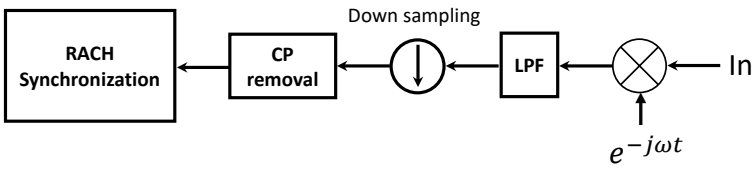

Figure 4.3: RACH signal reception.

4.3 SWP-Based Channel Modeling

The massive MIMO channel modeling part of this chapter is based on the approaches described in Chapter 3. As illustrated in Figure 4.4, an LTE BS is equipped with a massive MIMO antenna with N spatially separated antenna elements Elm_i ($i = 1, 2, \cdots, N$). Suppose, the LTE network has an operating frequency $\text{F} = \omega/2\pi$ and a sampling duration Δt. To broadcast an uplink signal $s(t)$, a UE emits an electromagnetic wave $e^{j\omega t}$ (Orfanidis, 2014) to carry the symbols to be transmitted as follows:

$$s(t) = \sum_{m=1}^{M} b_m(t)\, e^{j\omega t},$$

where symbol $b_m(t)$ is nonzero in the period $[(m-1)\Delta t, m\Delta t]$, and 0 in other periods. M is the number of transmitted symbols.

Let p_l represents a single path from the UE to antenna element Elm_i, and d_{li} represents the length of path p_l. All the symbols received at Elm_i along path p_l are delayed by $t_{li} = d_{li}/c$ where c is the speed of light. Let $s'_{li}(t)$ be the signal received at Elm_i along path p_l as follows:

$$s'_{li}(t) = a_{li} \sum_{m=1}^{M} b_m(t - t_{li})\, e^{j\omega(t - t_{li})} + \eta_i(t), \tag{4.2}$$

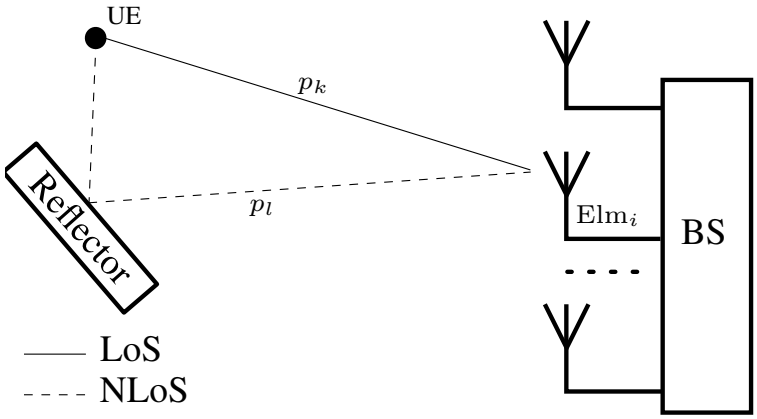

Figure 4.4: Communication between a UE and an LTE BS with massive MIMO.

where a_{li} is the path attenuation, and $\eta_i(t)$ is the noise. The attenuation coefficients are defined as $a_{li} = f(d_{li}, \omega, \text{Env})$, and indicating that a path attenuation depends on not only the traveled distance and the carrier's frequency but also the propagation environment Env (Raschkowski *et al.*, 2015).

In a real environment, a radio signal may reach each antenna element along multiple paths due to signal reflection, scattering, diffraction and refraction, which is known as multipath propagation (Hertz and Jones, 1893; Richter, 2005). Let $s'_i(t)$ be the signal received at Elm$_i$ via multipath propagation, and L_i be the number of paths traversed by the signals received at Elm$_i$. $s'_i(t)$ can be modeled as

$$s'_i(t) = \sum_{l=1}^{L_i} a_{li} s(t - t_{li}) + \eta_i(t), \tag{4.3}$$

where $t_{li} = d_{li}/c$ is the time delay to cover the distance d_{li} along path p_l from the UE to Elm$_i$.

In the following, the model is extended for multi-carrier signals. Let $s'_i(t, f_k)$ represent the signal received at Elm$_i$ with frequency f_k, where $k \in [1, N_s]$ and N_s is the number of subcarriers. Then Eqn. (4.3) can be extended for OFDM signals as follows (Salmi *et al.*, 2009; Li *et al.*, 2017):

$$\begin{pmatrix} s'_i(t, f_1) \\ s'_i(t, f_2) \\ \vdots \\ s'_i(t, f_{N_s}) \end{pmatrix} = \begin{pmatrix} \sum_{l=1}^{L_i} a_{li}(f_1) s_i(f_1, t - t_{li}) \\ \sum_{l=1}^{L_i} a_{li}(f_2) s_i(f_2, t - t_{li}) \\ \vdots \\ \sum_{l=1}^{L_i} a_{li}(f_{N_s}) s_i(f_{N_s}, t - t_{li}) \end{pmatrix} + \begin{pmatrix} \eta_i(t, f_1) \\ \eta_i(t, f_2) \\ \vdots \\ \eta_i(t, f_{N_s}) \end{pmatrix}. \tag{4.4}$$

4.4 Localization for the Single LoS Path Case

In this section, a localization method for the single path case is described. The solution for the multipath case will be presented in section 4.5.

4.4.1 Phase Estimation

Let us start the derivation of the localization problem from the assumption of ideally synchronized antenna elements in the BS. The non-ideal synchronization case is addressed in Section 4.4.3.

In the case of a single path and RACH signals, the notation a_{li} becomes a_i, t_{li} becomes t_i and the symbols b_m become RACH symbols in Eqn. (4.2). To recover each received symbol b_m, the BS removes the carrier wave $e^{j\omega t}$. Then the symbols received at Elm_i in Eqn. (4.3) can be represented as follows:

$$s_i''(t) = \frac{s_i'(t)}{e^{j\omega t}} = a_i e^{-j\omega t_i} \sum_{m=1}^{M} b_m(t - t_i) + \xi_i(t), \tag{4.5}$$

where $\xi_i(t)$ is a modified noise. As can be seen from Eqn. (4.5), the channel change (i.e. $a_i e^{-j\omega t_i}$ in Eqn. (4.5) is also reflected by t_i, which can be directly measured by phase shift. The time delay t_i can be estimated through the phase shift of the channel change.

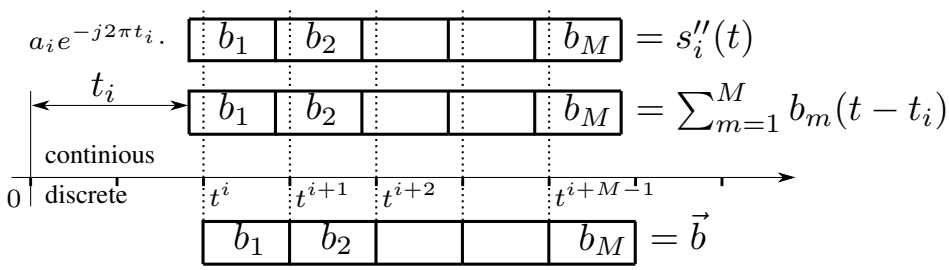

Figure 4.5: Illustration of signal shifting in continuous and discrete time domains.

A key challenge here is to retrieve the phase shift from the incoming signal in the digital domain. As illustrated in Figure 4.5, it is seen that the scalar product of the incoming signal $s_i''(t)$ with the one shifted by t_i symbols $\sum_{m=1}^{M} b_m(t - t_i)$ gives pure channel change h_i'' as follows:

$$h_i'' = \frac{1}{\|b\|^2}(s_i''(t), \sum_{m=1}^{M} b_m(t - t_i)) = a_i e^{-j\omega t_i} + \varsigma_i, \tag{4.6}$$

where the notation $(*,*)$ means the operation of scalar product, $\|b\|$ is the norm of vector $\boldsymbol{b} = (b_1, b_2, .., b_M)$, and ς_i is the modified noise. The phase shift of $s_i''(t)$, denoted by φ_i, is simply the argument of the channel change since the attenuation coefficient a_i for a LoS path is a real number, i.e.,

$$\varphi_i = -\arg(h_i'') = (\omega t_i + \delta\varphi_i) \bmod 2\pi, \tag{4.7}$$

where $\delta\varphi_i$ is noise caused by the modified noise, mod is the Modulo operator. However, the exact value of t_i is unknown. Thus, the only way to estimate t_i is based on the discrete measurements from antenna elements during the RACH synchronization procedure. Suppose the synchronization is performed with a sampling period of Δt. The BS can measure an incoming signal only at discrete time moments $t^k = k\Delta t$ as follows:

$$s_i''(t^k) = \frac{s_i'(t^k)}{e^{j\omega t^k}} = a_i e^{-j\omega t_i} \sum_{m=1}^{M} b_m(t^k - t_i) + \xi_i(t^k). \tag{4.8}$$

As illustrated in Figure 4.5, the shifted symbol $b_m(t^k - t_i) = b_m$ if

$$t^k \in [(m-1)\Delta t + t_i, m\Delta t + t_i].$$

Accordingly, starting from the time moment

$$t^i = \Delta t \lceil \frac{t_i}{\Delta t} \rceil \in [t_i, \Delta t + t_i]$$

at which

$$\sum_{m=1}^{M} b_m(t^i - t_i) = b_1,$$

antenna element Elm_i measures the values that contain useful signal as follows:

$$\begin{aligned} t^i, \quad & s_i''(t^i) = a_i e^{-j\omega t_i} b_1 + \xi_i(t^i); \\ t^{i+1}, \quad & s_i''(t^{i+1}) = a_i e^{-j\omega t_i} b_2 + \xi_i(t^{i+1}); \\ \dots \quad & \dots \\ t^{i+M-1}, \quad & s_i''(t^{i+M-1}) = a_i e^{-j\omega t_i} b_M + \xi_i(t^{i+M-1}). \end{aligned} \tag{4.9}$$

During all the previous moments t^k before the moment t^i, Elm_i measures noise $s_i''(t^k) = \xi_i(t^k)$ as no symbol is sent. The received signal can also be written using vector representation:

$$\boldsymbol{s}_i = a_i e^{-j\omega t_i} (0, \dots, 0, b_1, \dots, b_M) + \boldsymbol{\xi}_i. \tag{4.10}$$

In order to calculate the scalar product in Eqn. (4.6), the BS needs to shift symbols $\sum_{k=1}^{M} b_m(t)$, i.e. the RACH symbols vector $\boldsymbol{b} = (b_1, b_2, .., b_M)$, by $\lceil \frac{t_i}{\Delta t} \rceil$ integer steps in discrete time and calculates the scalar product with $\boldsymbol{s}_i$.

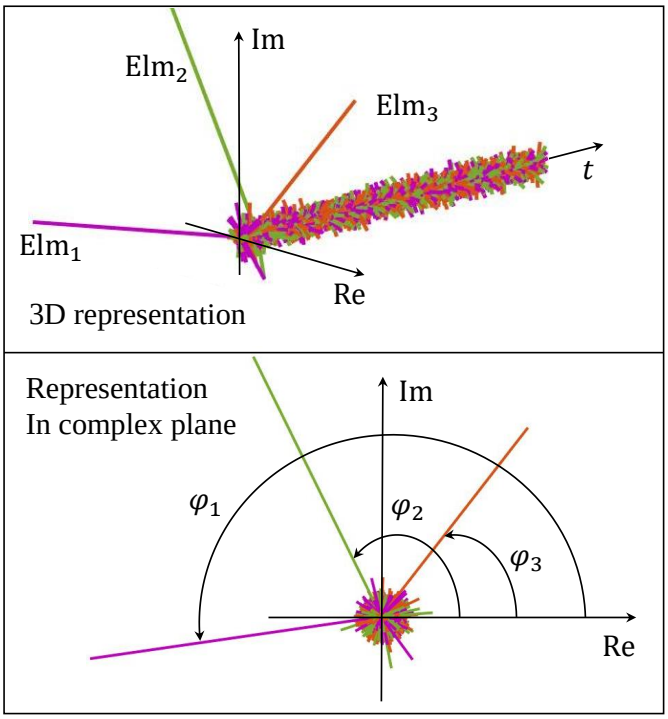

Figure 4.6: The results of RACH synchronization are depicted for three antenna elements in 3D and in a complex plane. The correlation spikes define phase shifts, which can be measured according to Eqn. (4.7).

In this way, the BS can measure the channel change at each antenna element and estimate phases of the incoming signals. Fortunately, the RACH synchronization procedure calculates a correlation vector between the incoming signal with the discrete shifted RACH vector, which is exactly the same operation as the scalar product in Eqn. (4.6) (Sesia *et al.*, 2011). Once a shift is the proper shift as in Eqn. (4.10), a spike occurs in the correlation vector, and the BS can then measure the argument of the spiking element and estimate the phase of the incoming signal according to Eqn. (4.7). This means that the scheme can take the values of correlation spikes directly from the RACH procedure and, consequently, it does not introduce an additional complexity in the correlation spikes calculation.

The main issue of the phase estimation is that the argument of the spiking element can only be measured in modulus 2π, which adds an ambiguity since the quotient (i.e. how many 2π's in the phase shift) is unknown. The following presents a phase sorting scheme to overcome this issue. It is assumed that the coordinates of each antenna element relative to the position of the MIMO antenna array are precisely known and the distance between any two neighboring elements is no larger than the half of the

wavelength $\lambda/2$ where $\lambda = 2\pi\frac{c}{\omega}$ (Orfanidis, 2014). This guarantees that the difference in phase changes of the received signals between two neighboring antenna elements is no larger than π. Consequently, for any two neighboring antenna elements, the signal with the smallest phase can be always found except in the situation where the difference is equal to π. This case is not considered because in practice, such situation is very unlikely since a BS maintains a particular area, which cancels situations with phase shifts close to π radians. The influence of noise $\delta\varphi_i$ can also be neglected in the phase sorting scheme since even in the situation with zero SNR RACH signals, the standard deviation of the phase noise is less than 0.03 radians (a detailed description is in Section 4.4.3). Hence, for any two neighboring antenna elements, the signal with smaller phase can be always found based on the following two rules:

- if $|\varphi_{i+1} - \varphi_i| < \pi$, the smaller one remains to be smaller than the bigger one;
- if $|\varphi_{i+1} - \varphi_i| > \pi$, the smaller one becomes bigger since the difference between them cannot be bigger than π, and 2π should be added to the smaller phase.

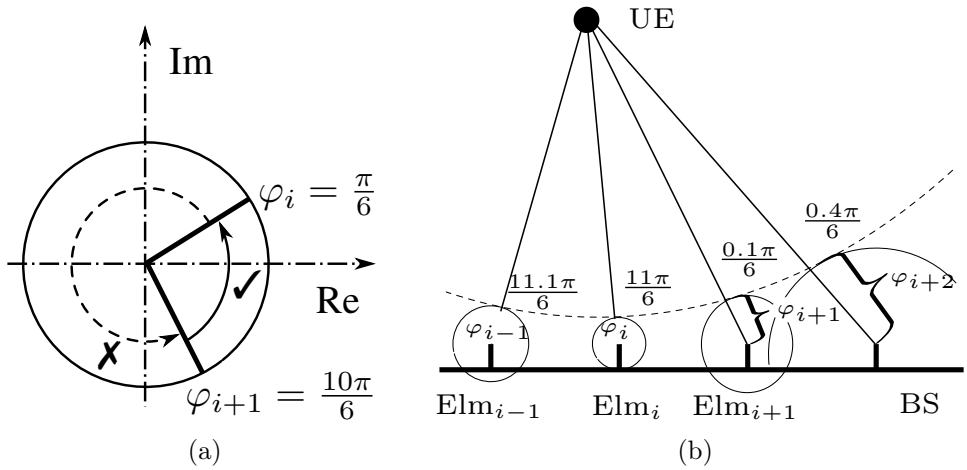

Figure 4.7: Phase shift at different antenna elements.

As illustrated in Figure 4.7(a), $\varphi_i = \frac{\pi}{6}$ and $\varphi_{i+1} = \frac{10\pi}{6}$. Since $|\varphi_{i+1} - \varphi_i| > \pi$, the actual difference should be $2\pi + \frac{\pi}{6} - \frac{10\pi}{6}$, i.e. the difference represented by the arrow with solid line instead of the one with the dashed line. Hence, $\varphi_i > \varphi_{i+1}$.

To compute the actual phase for the signal received at each antenna element, at first, the minimum phase has to be found among the signals received at all antenna elements. The minimum phase can be found by performing a pairwise comparison between neighboring antenna elements based on the above two rules. Suppose the signal

received at antenna element Elm_i has the minimum phase φ_i. For each neighbor of Elm_i denoted by Elm_j, if $|\varphi_j - \varphi_i| \leq \pi$, φ_j remains unchanged, otherwise $\varphi_k = \varphi_k + 2\pi$ for any Elm_k in the direction from Elm_i to Elm_j. The same operation needs to be repeated for the neighbors of Elm_j and so on until all φ_is have been corrected. As illustrated in Figure 4.7(b), the minimum phase is $\varphi_i = \frac{11\pi}{6}$. Since $|\varphi_{i-1} - \varphi_i| < \pi$, φ_{i-1} remains unchanged. For φ_{i+1}, $|\varphi_{i+1} - \varphi_i| > \pi$. Hence, each antenna element in the direction from Elm_i to Elm_{i+1} should correct its phase by adding 2π, i.e., $\varphi_{i+1} = \frac{0.1\pi}{6} + 2\pi = \frac{12.1\pi}{6}$ and $\varphi_{i+2} = \frac{0.4\pi}{6} + 2\pi = \frac{12.4\pi}{6}$. Then φ_{i+2} and φ_{i+1} are compared. Since $\varphi_{i+2} - \varphi_{i+1} < \pi$, $\varphi_{i+2} = \frac{12.4\pi}{6}$. In such a way the ambiguity caused by an unknown quotient is eliminated.

4.4.2 LoS Localization During RACH Synchronization

Because of the use of the SWP model, each phase shift φ_i corresponds to a certain distance

$$R_i = \lambda \times \frac{\varphi_i}{2\pi}.$$

As shown in Figure 4.8, each antenna element Elm_i is surrounded by a sphere with

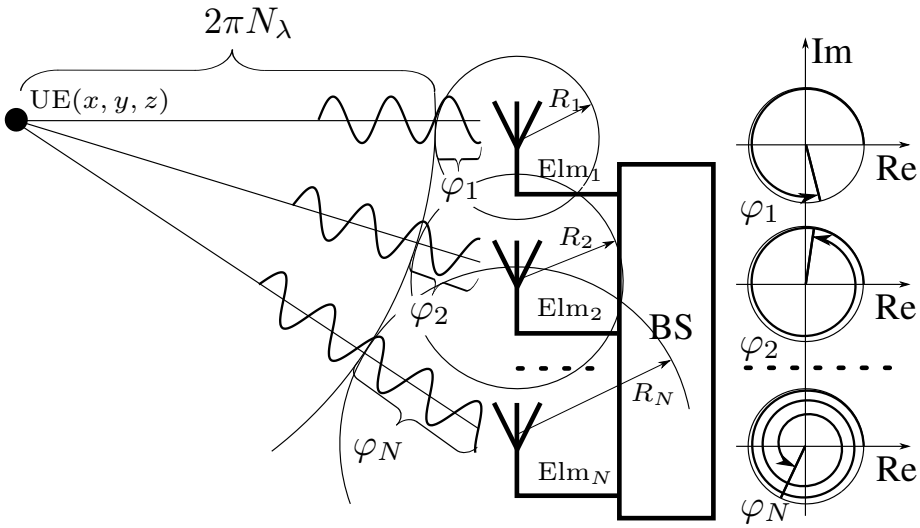

Figure 4.8: Phase shifts at antenna elements alongside the antenna array.

radius of R_i. Hence, due to the spherical propagation, there is a common sphere with radius of $R = 2\pi N_\lambda$ centered at the UE. The common sphere is, in fact, tangent to all the small spheres with radii of R_i where $i \in [1, N]$. It can be seen that the LoS distance from the UE to antenna element Elm_i can be rewritten by $d_i = R + R_i$, $i = 1, \ldots, N$. By representing d_i through the coordinates of the UE (x, y, z) and Elm_i (x_i, y_i, z_i), the

following relation can be obtained:

$$\sqrt{(x - x_i)^2 + (y - y_i)^2 + (z - z_i)^2} = R + R_i. \tag{4.11}$$

To localize the UE, the BS needs to jointly estimate the UE's coordinates and the common parameter N_λ. Since the number of unknown parameters is four (x, y, z, R), the coordinates of the UE can be calculated if there are no fewer than 4 antenna elements, which is not a problem for BS with Massive MIMO (Zhang *et al.*, 2016; Vieira *et al.*, 2017). Once the BS has enough antenna elements, the above formulated localization problem transforms to a classical GNSS positioning problem that can be solved using the Bancroft's algorithm (Bancroft, 1985).

4.4.3 Combating with Phase Noise

To understand how big is the phase noise between antenna elements in a massive MIMO antenna array, phase noise measuring experiments have been conducted using the "Otago University massive MIMO prototype" that consists of two radios Ettus USRPs N210 synchronized via a reference clock source NI OctoClock CDA-2990. The hardware is illustrated in Figure 4.9.

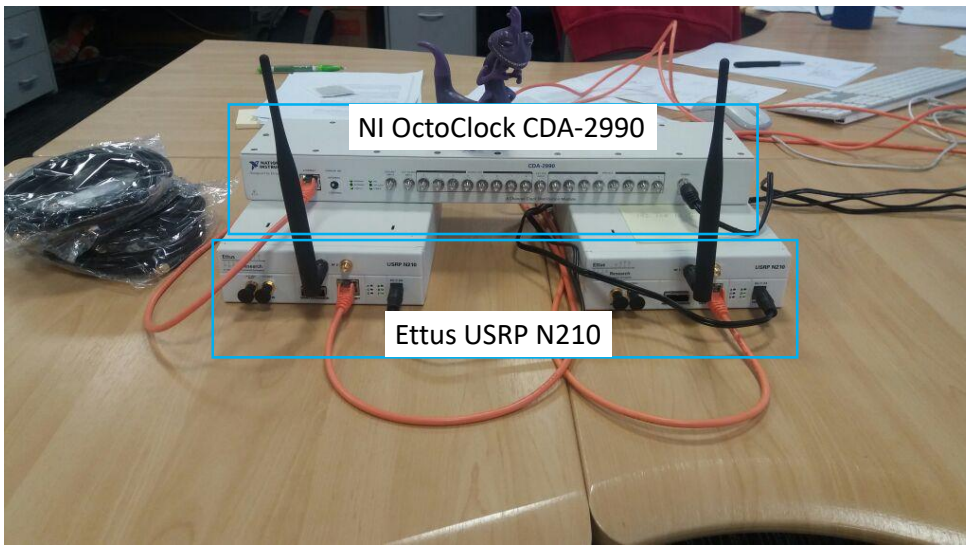

Figure 4.9: The massive MIMO hardware.

One USRP periodically sends RACH signals to the other USRP that calculates correlation between the incoming and local signals and measures the phase of a correlation spike as in Eqn. (4.7). The testbed is operating with a carrier frequency of 2.6 GHz and a sampling rate of 5.12 MS/s. Due to NI OctoClock, two radios are well synchronized,

but there is still a time variation between their samples, or in other words, synchronization inaccuracy. The same problem is in the discussed massive MIMO prototypes where each antenna has its radio chain, which is synchronized via a central reference clock of the BS (Malkowsky *et al.*, 2017). The aim of the measurements campaign is to measure the synchronization inaccuracy, which transforms to phase noise during communication. Thus, to minimize wireless channel effects and to guarantee a constant distance between the transmitter and receiver, two antenna ports of USRPs have been connected with a 1-meter long SMA-SMA cable. To obtain stochastic properties of the phase noise, 2900 RACH synchronization rounds with the phase shift measurement have been executed on the testbed. The histogram and Welch's power spectral density of the phase noise measurement campaign is illustrated in Figure 4.10 (Welch, 1967).

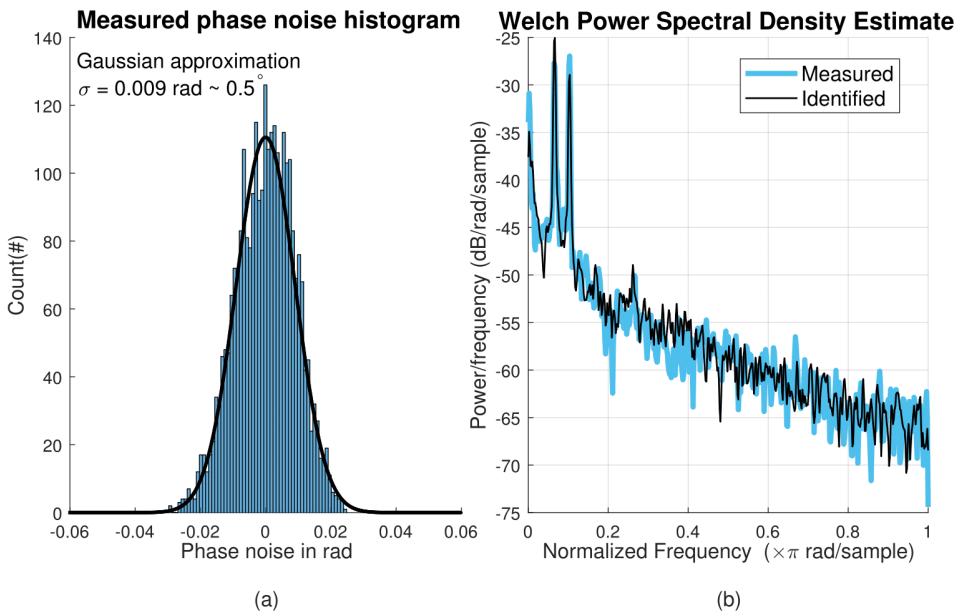

Figure 4.10: (a) Histogram of the measured phase noise; (b) Power spectral density of the measured phase noise.

As illustrated in Figure 4.10(a), the phase noise is too small to have a big impact on the phase sorting. However, it cannot be ignored in the phase shift estimation since it has a big impact on the localization accuracy (Yang *et al.*, 2014). Figure 4.10(b) shows the phase noise spectral density that has a number of significant spikes. In the presence of phase noise, the estimated phase after the sorting procedure can be represented as follows:

$$\varphi_i' = \varphi_i + \Delta\varphi_i + \delta\varphi_i, \tag{4.12}$$

where $\delta\varphi_i$ comes from the modified noise in Eqn. (4.6) and has Gaussian noise charac-

teristics, while $\Delta\varphi_i$ is the phase noise that has to be estimated during the localization procedure.

To take into account the phase noise, it is modeled as a response of a state space model to white noise (Ljung, 1999):

$$\begin{aligned} \boldsymbol{\eta}_{i+1} =& A\boldsymbol{\eta}_i + Ke_i, \\ y_i =& C\boldsymbol{\eta}_i + e_i, \end{aligned} \tag{4.13}$$

where matrices A, K, C define the state space model, y_i is the output that has the same statistical properties as $\Delta\varphi_i$, e_i is the disturbance of the model that has white noise properties and $\boldsymbol{\eta}_i$ is the vector of the model's states. In the conducted experiments, the best number of states is 6. The identified process y_i is illustrated in the black line in Figure 4.10 (b). In order to retrieve the pure φ_i from Eqn. (4.12), a Kalman filter approach is used where φ_i's are measurements and the state space model given in Eqn. (4.13) is the Kalman filter's dynamic part (Agee and Turner, 1972). The output of Bancroft's algorithm is used as the initialization for the Kalman filter. After the filtering, the output of the Kalman filter (i.e. φ_is) is put back to the Bancroft's algorithm to compute the refined UE location.

4.4.4 Eliminating Carrier Frequency Offset and Initial Phase Offset

There are always a carrier frequency offset (CFO) $\delta\omega$ and an initial phase offset ϕ that are caused by independent work of local oscillators of a UE and a BS. This non-ideality can be counted at the BS side in Eqn. (4.8) as follows:

$$\begin{aligned} s_i''(t^l) &= \frac{s_i'(t^l)}{e^{j\left[(\omega-\delta\omega)t^l-\phi\right]}} = \\ &= a_i e^{-j\omega t_i}\left[e^{j\phi}\sum_{m=1}^{M} b_m(t^l - t_i)e^{j\delta\omega\, t^l}\right] + \xi_i(t^l). \end{aligned} \tag{4.14}$$

In the same way as in Eqn. (4.9), the useful signal starts to reach Elm_i at moment t^i, and the vector representation of the received signal given in Eqn. (4.10) can be rewritten as follows:

$$\boldsymbol{s}_i = K_i e^{j\phi}\left(0, \ldots, 0, b_1 \mathrm{f}^i, \ldots, b_M \mathrm{f}^{i+M-1}\right) + \boldsymbol{\xi}_i, \tag{4.15}$$

where

$$\mathrm{f}^i = e^{j\delta\omega\, t^i},$$

and

$$K_i = a_i e^{-j\omega t_i}.$$

Hence, the spiking value in the correlation vector between the incoming signal and RACH preamble vector $\boldsymbol{b}$ can be represented as:

$$h'_i = a_i e^{-j\omega t_i} \left[e^{j\phi} \frac{1}{\|\boldsymbol{b}\|^2} \sum_{m=1}^{M} f^{i+m-1} \right] + \varsigma_i. \tag{4.16}$$

The CFO impact, inside of the square brackets in Eqn. (4.16), depends on the starting moment t^i, which can be different for different antenna elements. However, in LTE RACH synchronization, the maximum difference is no more than one RACH sampling period, i.e. for any two antenna elements $\mathrm{Elm}_i, \mathrm{Elm}_k$, the difference in the first receiving moments $|t^i - t^k| \leq \Delta\tau$ where $\Delta\tau$ is the length of the RACH sampling period. This is because the sampling rate of RACH preamble vector $\boldsymbol{b}$ is 1.28 MHz, which is 24 times smaller than conventional LTE sampling rate 30.72 MHz (Sesia *et al.*, 2011). Hence, to make it possible for the situation when $|t^i - t^k| > \Delta\tau$, the size of a massive MIMO antenna array has to be bigger than

$$\frac{3 \cdot 10^8\,\mathrm{m/s}}{1.28\,\mathrm{MHz}} \approx 234\,\mathrm{meters}.$$

In the case where $|t^i - t^k| = \Delta\tau$, it is preferable to take the moment (t^i or t^k) for which the maximum number of antenna elements have spiking values. In this way, all elements of the massive MIMO antenna array obtain the same impact from the CFO and initial phase offset provided that all antenna elements are well-synchronized (Vieira *et al.*, 2017). In the same way, the phases of the incoming signals can be estimated at different antenna elements. All spiking values are then divided by the spiking value with the minimum phase as follows:

$$h''_i = \frac{h'_i}{h'_*} = a_i e^{-j(\omega t_i - \varphi^*)} + \nu_i, \tag{4.17}$$

where h'_* is the spiking value with the minimum phase φ^*, and ν_i is the modified noise. Let r^* be the radius that corresponds to φ^*. From Eqn. (4.17), it is well seen that h''_i has a phase shift relative to φ^*. It means that the relative phase shift for the antenna element with φ^* becomes zero and its region has a zero radius, whereas the radii of the rest regions are reduced by r^*. Consequently, the radius of the common sphere centered at the UE is increased on r^*. The localization problem now can be rewritten as follows:

$$\sqrt{(x - x_i)^2 + (y - y_i)^2 + (z - z_i)^2} = R + r^* + (r_i - r^*), \tag{4.18}$$

and can be solved in the same way as Eqn. (4.11). Please note, the operation in Eqn. (4.17) change the noise properties in Eqn. (4.12)); however, the model in Eqn. (4.13) stays the same except the doubled variance of the disturbance e_i, which has to be taken into account during the phase noise estimation.

4.5 Localization for the Multipath Case

For the l-th path from UE to antenna element Elm_i, the attenuation coefficient a_{li} can be represented in the form of a complex number as:

$$a_{li} = r_{li}\, e^{j\theta_{li}}.$$

Since the attenuation for a LoS path is usually considered as a free-space loss, its attenuation coefficient commonly has a real value, that is why $\theta_{li} = 0$ (Orfanidis, 2014). This makes it possible for the single-path solution to localize a UE owing to the unnecessity to estimate the attenuation coefficients since real-valued attenuation does not introduce any phase rotation (θ_{li}). However, the attenuation coefficients for multipath propagation are generally considered as complex values (Tse and Vishwanath, 2005), and a localization algorithm has to estimate these attenuation coefficients too. Hence, the parameters to be estimated include the UE's coordinates (x, y, z), the radius of the common sphere R, and the attenuation coefficients for all paths that are different for each antenna element. Suppose the total number of paths is L. The number of parameters to be estimated becomes $4 + LN$ that is larger than the number of antenna elements N. Thus, the proposed single-path solution cannot be simply extended for the multipath case. In this section, the localization problem for the multipath scenario is solved by exploiting the OFDM nature of RACH signals.

Unlike the solution for the LoS path case, the channel influence is derived in the frequency domain, which makes it easier to understand the channel influence on OFDM signals. The approach proposed in this section first constructs a model of the radio channel based on the known environment and then optimizes it based on OFDM measurements using a nonlinear data-fitting procedure. Since RACH signals are OFDM based and the received signal is known due to the RACH synchronization procedure, the channel influence can always be estimated in the frequency domain.

4.5.1 Channel Model in Frequency Domain

The frequency response of a multipath channel Eqn. (4.3) at Elm_i, denoted by H_i, can be represented as follows (Tse and Vishwanath, 2005):

$$H_i = \sum_{l=1}^{L_i} a_{li} e^{-j\omega t_{li}}, \tag{4.19}$$

where L_i is the number of paths from the UE to Elm_i, and t_{li} is the time for the signals to traverse distance d_{li} along path l.

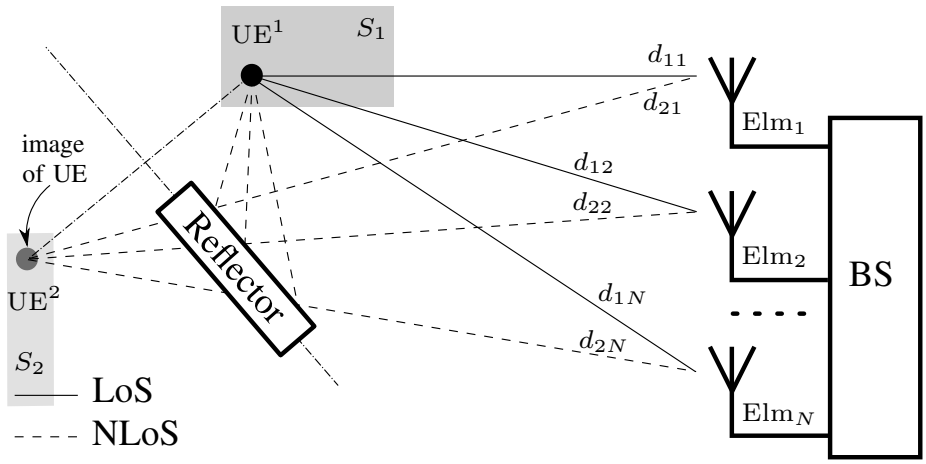

Figure 4.11: Reception of a multipath signal, S_1 and S_2 are the location search areas.

A transmitted signal during its propagation may interact with objects in the propagation environment as it is discussed in Chapter 3. Once an interacted signal is received by the BS, it is noted as an NLoS signal. The interactions can be in general grouped into physical phenomena such as reflection, scattering, diffraction and refraction/penetration (Raschkowski *et al.*, 2015; Richter, 2005). Regardless of the physical phenomena, NLoS signals cover different distances and have different angles of arrival. Consequently, from the BS perception, it looks like that the NLoS signals come from different sources. These sources are further referred to as images of the original source as illustrated in Figure 4.11, where the black circle is the real position of the UE with coordinates x^1_{UE} and the gray circle is the UE's image with coordinates x^2_{UE}. The coordinates of the images can be found through the Householder transformation Eqn. (3.8).

The distance d_{li} from image UE^l that has coordinates $x^l_{\text{UE}} = (x^l, y^l, z^l)^T$ to Elm_i is represented as an Euclidean distance:

$$d_{li} = \|\text{Elm}_i - x^l_{\text{UE}}\|.$$

The attenuation coefficient a_{li} is defined in Eqn. (3.4) and it can be treated as a function of distance d_{li}, frequency ω, physical properties of the interacting objects, positions and orientations of the communicating UE and BS:

$$a_{li} = \frac{c}{2\omega} \frac{\rho_{li} G_{li}}{\|\mathrm{Elm}_i - x^l_{\mathrm{UE}}\|}, \tag{4.20}$$

where ρ_{li} is the coefficient of roughness defined in Eqn. (3.15); G_{li} is defined in Eqn. (3.13) and is responsible for the attenuation caused by the path l Eqn. (3.12), orientations and locations of the UE and Elm_i, and the Fresnel reflection coefficients defined in Eqn. (3.17) and Eqn. (3.18). The coefficients ρ_{li} and G_{li} are frequency dependent by definition. However, a relatively small deviation in frequency does not change these coefficients much. Especially in the case of RACH signals where the bandwidth is 1.28 MHz, the coefficients change can be neglected. Thus, to simplify the model, each pair $\rho_{li} G_{li}$ is considered as a single frequency independent coefficient $\Gamma_{li} = \rho_{li} G_{li}$.

The model of a multipath channel given by Eqn. (4.19) can then be refined by incorporating Eqn. (4.20) as follows:

$$H_i = \sum_{l=1}^{L_i} \left[\frac{c}{2\omega} \frac{\Gamma_{li}}{\|\mathrm{Elm}_i - x^l_{\mathrm{UE}}\|} \right] e^{-j\frac{\omega}{c}\|\mathrm{Elm}_i - x^l_{\mathrm{UE}}\|}. \tag{4.21}$$

This is a system of N equations $i = 1, \ldots, N$ as the antenna array has N elements. The number of unknown parameters Γ_{li} and x^l_{UE} is equal to $\sum_{i=1}^{N} L_i + 3\max_i\{L_i\}$ (here 3 comes from $x^l_{\mathrm{UE}} = (x^l, y^l, z^l)$), which is bigger than N. In the case where all $L_i = L$, the number of the unknowns becomes equal to $NL + 3L$.

Since RACH signals are OFDM signals, channels can be measured on each subcarrier. In the same way, to be able to estimate the propagation parameters, it is worth to derive channel models for each subcarrier as follows:

$$\boldsymbol{H_i} = \begin{pmatrix} H_{i1} \\ H_{i2} \\ \vdots \\ H_{iN_s} \end{pmatrix} = \begin{pmatrix} \sum_{l=1}^{L_i} \frac{c\Gamma_{li}}{2f_1} \frac{e^{-j2\pi\frac{f_1}{c}\|\mathrm{Elm}_i - x^l_{\mathrm{UE}}\|}}{\|\mathrm{Elm}_i - x^l_{\mathrm{UE}}\|} \\ \sum_{l=1}^{L_i} \frac{c\Gamma_{li}}{2f_2} \frac{e^{-j2\pi\frac{f_2}{c}\|\mathrm{Elm}_i - x^l_{\mathrm{UE}}\|}}{\|\mathrm{Elm}_i - x^l_{\mathrm{UE}}\|} \\ \vdots \\ \sum_{l=1}^{L_i} \frac{c\Gamma_{li}}{2f_{N_s}} \frac{e^{-j2\pi\frac{f_{N_s}}{c}\|\mathrm{Elm}_i - x^l_{\mathrm{UE}}\|}}{\|\mathrm{Elm}_i - x^l_{\mathrm{UE}}\|} \end{pmatrix}, \tag{4.22}$$

where $f_k = \omega + k\Delta f$ is the k-th subcarrier's frequency, Δf is the frequency separation between the subcarriers, and $\Delta f = 1250$ Hz for RACH signals (Sesia *et al.*, 2011).

Non-zero RACH symbols are carried by $N_s = 839$ subcarriers, which means that the number of unknown parameters becomes much less than the number of equations. For

each antenna element Elm_i, the number of unknown parameters is $L_i + 3L_i$ according to Eqn. (4.22), where L_i is the number of unknown coefficients Γ_{li} and $3L_i$ is the number of unknown coordinates of L_i image sources. In practice $L_i \ll N_s$. It has been reported that the number of observed paths is no more than 15 when the distance to UE is more than 20 meters (Mahler *et al.*, 2015; Raschkowski *et al.*, 2015).

4.5.2 RACH OFDM Measurements

Similarly to the single-path case, all required operations are already calculated during the RACH synchronization procedure including the channel estimation. In fact, the BS calculates correlation vectors between incoming signals and local sequences based on the Fourier transformation where multiplication operations are done in the frequency domain (Fedorov *et al.*, 2015). Since the amplitudes of RACH symbols are equal to one, the conjugated multiplication of incoming symbols with RACH symbols becomes equivalent to the corresponding division of the incoming symbols to the RACH symbols. This means that the BS can obtain the channel measurements without introducing an additional complexity during the multiplication operation in the frequency domain. The channel measurement $\boldsymbol{H_i}'$ at Elm_i can be represented by:

$$\boldsymbol{H_i}' = \boldsymbol{H_i} + \boldsymbol{r_i}, \tag{4.23}$$

where $\boldsymbol{r_i}$ is an N_s dimensional vector of noise.

Now, the channel is accurately derived based on the positions of the BS's antenna elements, the UE and its images, and the surrounding environment. However, a single antenna by itself can only resolve the distances d_{li}, but not the coordinates of images x^l_{UE}. Hence, the measurements from all antenna elements of the BS have to be combined together to jointly estimate all the unknown coordinates x^l_{UE}. The combined measurements for N antenna elements of the BS can be written in a vector form as follows:

$$\begin{pmatrix} \boldsymbol{H_1}' \\ \boldsymbol{H_2}' \\ \vdots \\ \boldsymbol{H_N}' \end{pmatrix} = \begin{pmatrix} \boldsymbol{H_1} \\ \boldsymbol{H_2} \\ \vdots \\ \boldsymbol{H_N} \end{pmatrix} + \begin{pmatrix} \boldsymbol{r_1} \\ \boldsymbol{r_2} \\ \vdots \\ \boldsymbol{r_N} \end{pmatrix}.$$

Let us denote the $N \cdot N_s$ dimensional vectors as follows

$$\mathbf{H}' = \mathbf{H} + \mathbf{r}. \tag{4.24}$$

4.5.3 Localization as an Optimization Problem

The main goal is to find the position x_{UE} of the UE. The multi-path localization problem can be formulated as the following optimization problem with the objective to minimize the squared difference between the channel measurements $\mathbf{H}'$ and the channel model $\mathbf{H}$ from Eqn. (4.24).

$$\min_{\{\Gamma_{li}, x^l_{\text{UE}}\}} \quad \|\mathbf{H}' - \mathbf{H}\|^2 = \min_{\{\Gamma_{li}, x^l_{\text{UE}}\}} \sum_{i=1}^{N} \sum_{k=1}^{N_s} \|H'_{ik} - H_{ik}\|^2 \tag{4.25a}$$

$$\text{s.t.} \quad x^l_{\text{UE}} \in S_l, \forall p_l \in \bigcup_{i=1}^{N} L_i. \tag{4.25b}$$

Here, S_l are search areas, an example of search areas is illustrated in Figure 4.11. The objective function given in (4.25a) is nonlinear due to the nonlinearity of the channel model Eqn. (4.22). Such kind of optimization problem can be solved using one of the standard optimization methods such as Levenberg-Marquardt (Marquardt, 1963), SAGE (Fleury *et al.*, 1999), or RIMAX in a more complex propagation model (Salmi *et al.*, 2009) with dense multipath components.

The constraints in (4.25b) restrict the regions where the UE and its images can locate. It is assumed that the BS has the knowledge of its surrounding environment due to the availability of Google maps, Openstreetmaps, and the heatmaps generated based on the statistics of cellular and Internet traffic. The search regions can be restricted to the areas that are accessible to human beings. The RACH synchronization procedure can also help to reduce the size of the search area. It can provide a rough estimation of the time delay based on the position of the correlation spike, by which the distance from UE to BS can be estimated with the accuracy of ~ 200 meters (Sesia *et al.*, 2011). The intersection of the area maintained by the BS and the ring defined based on the estimated time delay (RACH ring area) can be employed to further decrease the search area.

Since the objective function is nonlinear and non-convex, it is vital to start the optimization from a good initialization as an improper starting point may cause early convergence to a local minimum. A straightforward approach to estimate the global optimal location is to split the area maintained by the BS into small pieces and perform an optimization within each small area. However, the complexity of such a naive approach is very high. The idea used in the dissertation is to use the output of the single-path localization algorithm as the initialization for the optimization problem.

4.6 Performance Evaluation

In this section, the experimental setups and results of the simulation and proof-of-concept experiments are discussed.

4.6.1 Simulation Setup

The carrier frequency F = $\omega/2\pi$ is set to 2.6 GHz, which is typical for LTE systems. The RACH signals occupy 864 subcarriers including 25 guard/empty subcarriers with the subcarrier spacing of $\Delta f = 1250$ Hz. The preambles are constructed according to LTE RACH signals format 0, which is set for a network cell with a radius of approximately 14 km. According to the RACH performance report from the European Telecommunications Standards Institute (ETSI), for a single-antenna receiver, the SNR is set to -17 dB (minus seventeen decibels) for the signals sent from the edge of a cell (ETSI, 2011). This SNR is used to generate background additive white Gaussian noise by considering the distance of 14 km and the UE transmitter power of 100 milliwatts.

The simulation setup includes one UE and one BS. The UE has one transmitting antenna element, whereas the number of antenna elements at the BS is varied from 16 to 100 in the single-path case, and from 8 to 64 in the multi-path case. The antenna elements at the BS is simulated as a uniformly distributed array alongside a line. The distance between two neighboring elements is configured to be half of the wavelength $\lambda/2 \approx 6$ cm (Orfanidis, 2014). Both communication sides have vertically oriented antennas. The coordinates of the BS are used as the center of the MIMO antenna array, and the coordinates of the UE as the coordinates for its single antenna. Each antenna element receives a signal mixed with the background noise that is -17 dB. The signal reception by a massive MIMO BS is simulated based on the modeling approaches described in Chapter 3. To evaluate the performance of the proposed algorithms in the single-path and multi-path cases, the following two scenarios are considered:

Single-Path Case

The UE is located in a sector with a 120 degree angle. The distance from the UE to the BS is varying from 10 to 500 meters. The single-path algorithm is tested for the single-path case to localize a UE in the following five regions: 10m - 50m, 50m - 100m, 100m -150m, 150m -300m, and 300m - 500. The 10m - 50m region is used to evaluate the performance for the near-field region, the next three scenarios are used for the transition regions between the near and far field regions, and the last scenario is used

to check the localization performance for the region that is around or exceeding the edge between the near and far fields. Note, the size of the near field region is defined by the size of an antenna array. The both measured and modeled phase noises are incorporated in the simulation. The results presented in Figure 4.12 and Figure 4.13 are calculated based on the results of 500 rounds for each configuration.

Multi-Path Case

The position of the UE is varying inside of the same sector as for the single-path case but the distance is limited to 200 meters. The NLoS signals are simulated to be specular reflections from concrete walls. The Fresnel coefficients of reflection $\Gamma_{\perp}$ Eqn. (3.17) and $\Gamma_{\parallel}$ Eqn. (3.18) are calculated based on the experimental measurements provided in (Raschkowski *et al.*, 2015). To simulate reflections, two walls are randomly placed within the simulated area such that they do not block the LoS path. The images of the UE are calculated relative to the walls using the Householder transformation Eqn. (3.8). The phase noise has not been incorporated to the multipath simulation. The results presented in Figure 4.14 are calculated based on the averaged values of 100 rounds for each configuration.

4.6.2 Simulation Results

Single-Path Scenario

The localization algorithm for the single-path case is evaluated using the following two metrics:

- Localization error: the Euclidean distance between the estimated location and the real UE location;
- Angle error: the difference on angle-of-arrival (AoA) between the estimated location and the real location.

Figure 4.12 shows the Root Mean Square (RMS) of the localization error with the variation of the number of antenna elements, respectively. The errors higher than 2.5 meters are not drawn on the plot. The blue lines represent the results of the Bancroft's algorithm, and the black lines represent the results of the Bancroft's algorithm after taking into account the phase noise Section (4.4.3). Figure 4.13 shows the RMS of the angle error with the variation of the number of antenna elements.

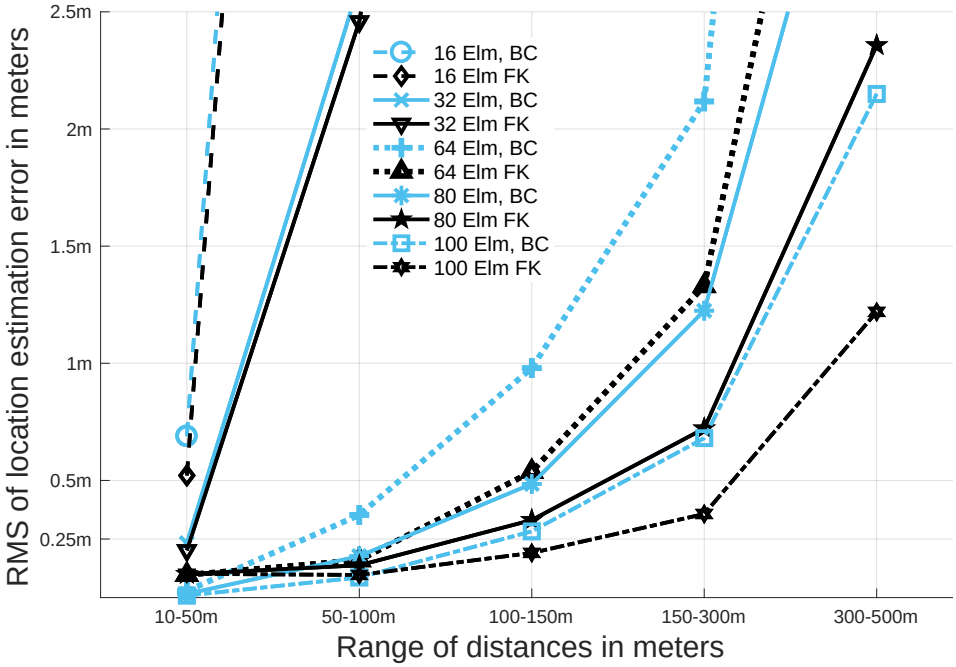

Figure 4.12: Single-path: RMS of the localization error for the Bancroft (BC) and refined (FK) results.

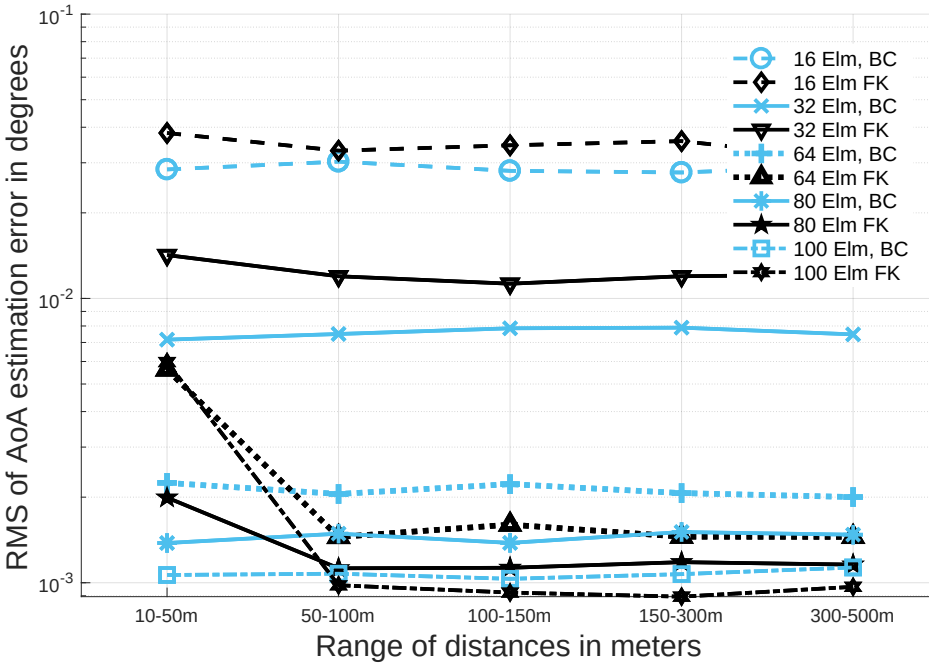

Figure 4.13: Single-path: RMS of the AoA estimation error for the Bancroft (BC) and refined (FK) results.

A key observation from the two figures is that the SWP assumption is desirable for massive MIMO systems since the localization and angle errors decrease with the increase of the number of antenna elements. Even for the region of 300m-500m, the achievable accuracy with 100 antenna elements is around one meter after taking into account the phase noise. This enables the user separation in crowded open areas such as sports matches in stadiums and open-air events.

Another observation is that in the SWP model the phase noise can significantly deteriorate the localization performance. This is why it is vital to take into account the phase noise in localization procedures. The simulation results confirm the necessity of the phase noise elimination because the refined results (i.e. FK results) are better than the results of the standard Bancroft's algorithm. An exceptional situation occurs when the number of antenna elements is higher than 64 and the distances are closer than 100 meters. The reason for this effect is that the trends of the pure phases φ_i from (4.12) are approximated using parabolic shapes in the Kalman filtering. In other words, using a Kalman filter, parameters of a parabolic shape are searched in the phase measurements (4.12) by taking into account the phase noise, and then the resulting parabolic shape is fed to Bancroft's algorithm. Obviously, a small portion of a sphere can be well approximated by a parabolic shape, but if the portion of a sphere is big enough, then the parabolic approximation becomes worse. In the case of small distances, the same effects can be seen when comparatively big portions of spherical shapes are captured by big antenna arrays and the refinement using a Kalman filter, in opposite, deteriorates the performance of the localization algorithm.

It is worth noting that the AoAs can be estimated with accuracy less than one degree. However, it can be well seen that the constructed Kalman filter converges slowly, and it starts to converge after 32 iterations, i.e. if an antenna array has more than 32 antennas. This effect is observed in Figure 4.13 where the AoA estimation accuracy for 16 and 32 elements is deteriorated by the refinement (the first and the second black lines from the up in the figure) while it is improved by the refinement for the higher number of antenna elements.

Multi-Path Scenario

At first, the single-path solution is executed to estimate the initial position. If the single path algorithm gives a solution that is behind walls, then the initial point is set near the intersection of the walls. As it was mentioned above, the BS has knowledge about the surrounding environment. That is why it is possible to place the initial

position near the intersection of the walls. Empirically, it has been found that the single-path algorithm gives an unpredictably large error when the power of reflected signals is relatively high. Due to this fact, in the simulation experiments, the initial position is always set based on the information about the surrounding environment (an environmental initialization). A standard Matlab function `lsqnonlin` has been used to solve the formulated non-linear optimization problem Eqn. (4.25). To terminate the running of `lsqnonlin`, the following stopping policy is used: if the difference between two adjacent steps is smaller than 10^{-19}, then the Matlab function `lsqnonlin` aborts.

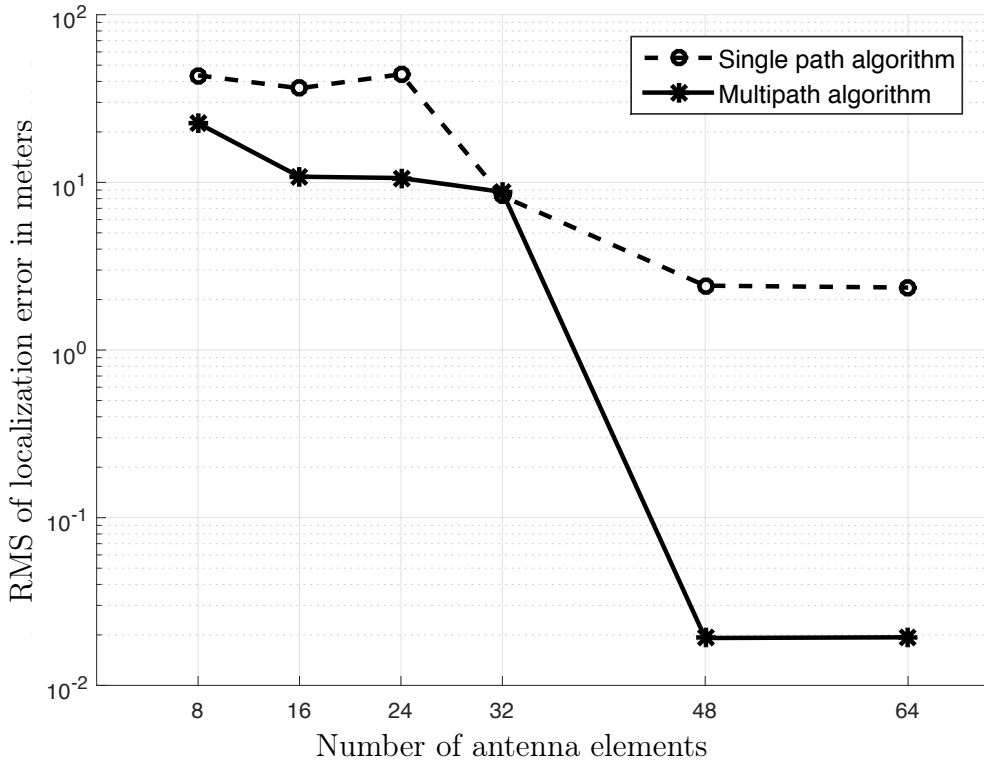

Figure 4.14: Multipath: RMS of multipath localization error.

Figure 4.14 compares the RMS with those of the single-path algorithm. It is well seen that the multipath algorithm gives slightly better results in comparison with the single paths algorithm when the number of antenna elements is no larger than 32. This is because the ability to choose slightly better initializations in overall has a positive impact. Significant improvement occurs when the number of antenna elements reaches 48. This means that starting from 48 elements, the amount of measurements becomes enough for the multipath algorithm to resolve the localization problem even if the initialization is not accurate. The proposed algorithm for the multipath case becomes robust and the achieved accuracy is within several centimeters. The accuracy of the

scenarios with a small number of antenna elements is worse due to the impact of weak initialization. If a good initial point is chosen, the result becomes good, otherwise, the algorithm may be trapped in a local minimum, and the Matlab solver does not have a good performance. Please note that the phase noise is not considered in the multipath scenario.

4.6.3 Proof-of-Concept Experiment

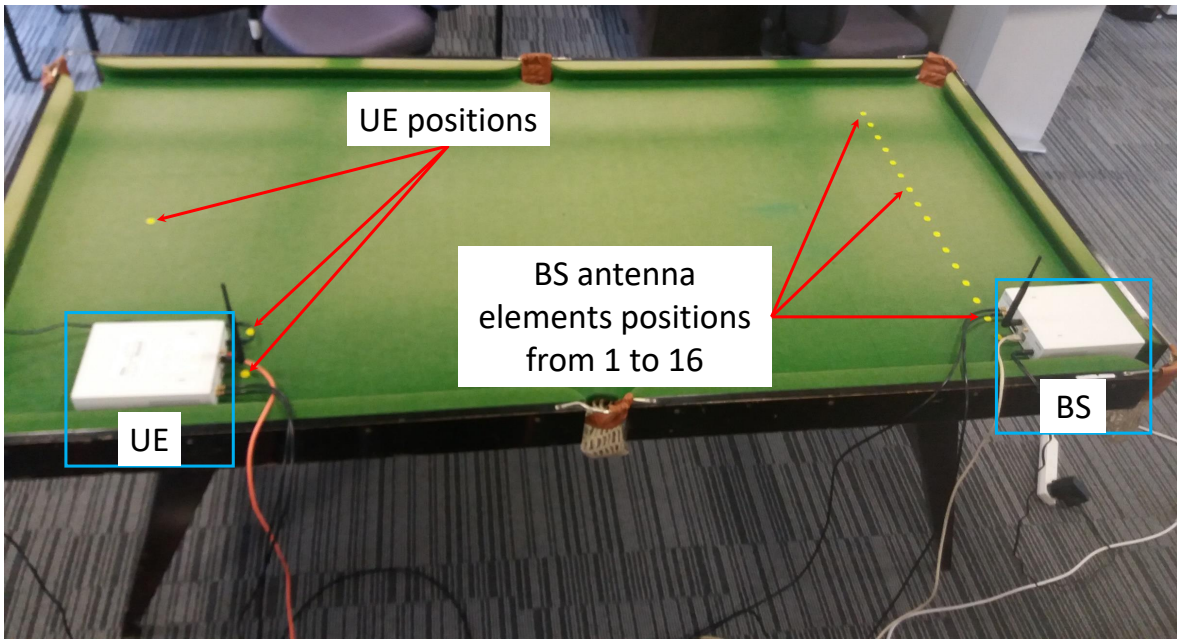

Figure 4.15: The Otago University Massive MIMO testbed that is capable of emulating simultaneous reception of up to 16 antennas. Yellow dots on the right side indicate the positions of MIMO antenna elements, on the left side indicate positions of the UE.

The single-path solution has been implemented on the massive MIMO testbed. The number of antennas on the emulated antenna array varies between 8, 12 and 16 antenna elements. The experimental setup is the same as in the phase noise measurements experiment described in 4.4.3 except the two radios are communicating through the air as illustrated in Figure 4.15. The ranges of experiments are limited by the lengths of available SMA cables that synchronize the radios, which do not allow positioning the two radios further than 2 meters from each other. The UE repetitively sends RACH signals over the air, and the receiver changes its position according to the required number of times to emulate antenna arrays with 8, 12 and 16 elements. Once the receiver captures a signal, it performs the RACH synchronization procedure and

measures the phase of the correlation spike as in Eqn. (4.7). Since the radios know the transmission moments due to the reference clock, the time alignment has been performed to emulate simultaneous reception by all antenna elements. The sorted phases are illustrated in Figure 4.16. It can be seen that the phase changes consistently according to the positions of the antenna elements, thereby justifying the feasibility of the designed solution.

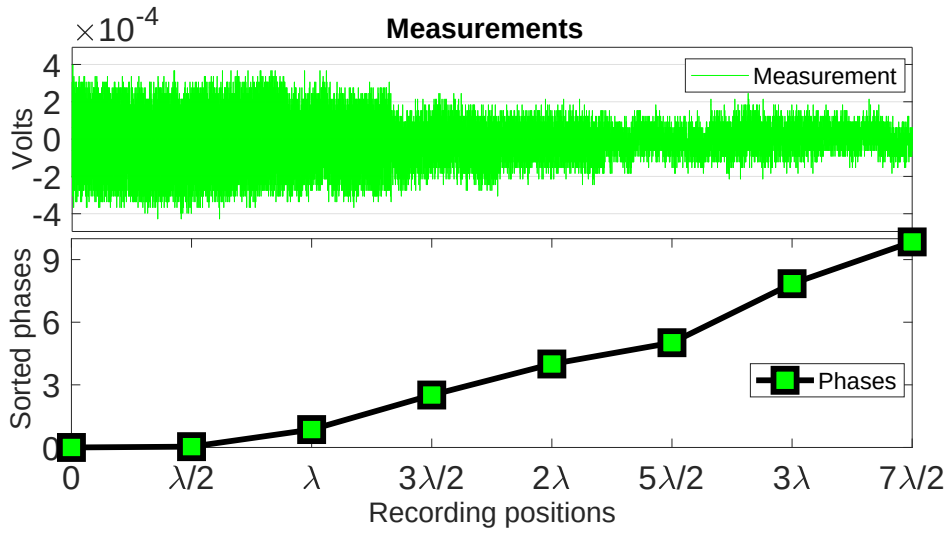

Figure 4.16: Experimental results: sorted phases obtained from the RACH synchronization procedure.

The experiments have been conducted in an indoor office environment with moving objects and people. For each position, the testbed executes 16 RACH procedures. Consequently, for each antenna configuration, the localization algorithm has been executed 16 times as illustrated in Figure 4.17. The centimeter-level accuracy is achieved because of the emulated antenna array can easily capture the spherical shape of the wavefront for such limited distances. The key observation from the proof-of-concept experiment is that the localization accuracy is increasing with the increase of the number of antenna elements. Thus, from a 4.3cm accuracy for 8 antennas, it goes down to a 1.3 cm of accuracy for 16 antennas. The doubling of the number of antenna elements gives an improvement more than two times. Note, the phase noise elimination has not been performed in these experiments since the sizes of antenna arrays are too small for using the Kalman filtering approach described in section 4.4.3. Instead, a calibration procedure has been done where using the known position of the UE, the initial phase shifts have been estimated for all 16 antennas. Then 16 executions of the localization

procedure have been done by taking into account the estimated initial phase shifts.

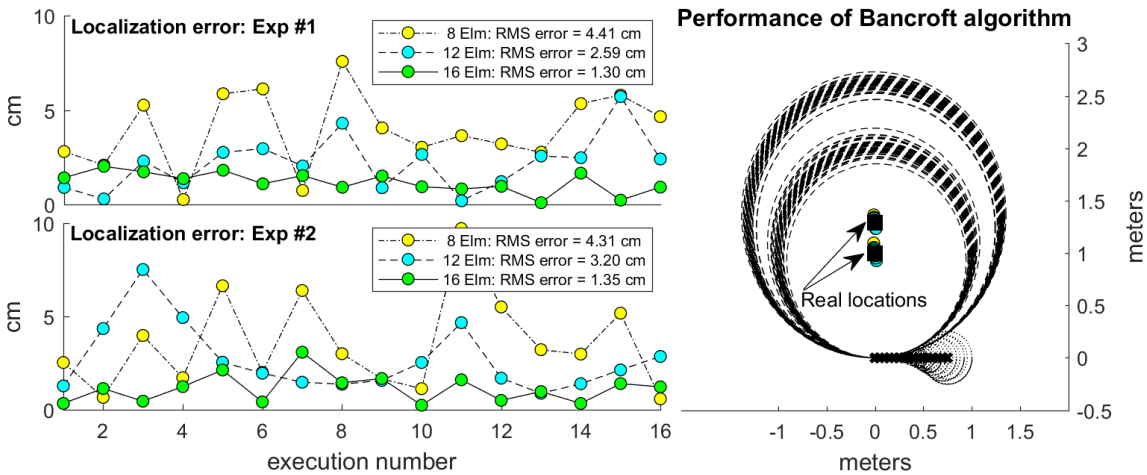

Figure 4.17: Experimental results: the estimation of two locations with different number of antenna elements.

4.7 Conclusion

In this chapter, two algorithms to localize LTE UEs during the RACH synchronization procedure are proposed. The first algorithm is designed to localize UEs in the single path case using phase rotations of incoming signals, which can be measured by the antenna elements of a massive MIMO BS during the procedure of RACH synchronization. The second algorithm works in the multipath case, in which the multipath channel is modeled using the spherical wave propagation assumption and linked to the propagation environment. The proposed schemes have been evaluated in both simulations and experiments. The obtained results show that the localization algorithms can achieve decimeter-level accuracy for massive MIMO with a big number of antenna elements. The further development of the research lays in the extensive experimental validation of the algorithms and the enhancement of the optimization methods.

Chapter 5

Downlink Channel Reconstruction

This chapter presents an efficient solution for downlink channels reconstruction of non-transmitting antennas of a UE based on an incomplete observation of uplink channels of the UE's transmitting antennas. The key idea of the DL channel reconstruction is to use the location and orientation information of non-transmitting antennas, which can be inferred based on the UL signals received from the transmitting antennas. In addition to the location information, for a non-transmitting antenna, the information about its orientation becomes critical for reconstructing the antenna's channel because for the same location, for example, two antennas can have significantly different channels depending on their orientations. The methodology on the estimation of the orientation of a transmitting antenna in both single-path and multi-path propagation environments is thoroughly described in this chapter. The estimation of the orientation is determined as a closed-form expression in both propagation environments.

More advanced channel modeling approaches are also presented that are complementary to the methods described in Chapter 3. The advancement is caused by the introduction of a new concept of a non-zero size antenna. The consequence of the introduced concept is that an antenna is no longer treated as a source-point but defined by its size and orientation. The concept enables modeling a more realistic variation of the electromagnetic wave polarization caused by the mobility of a UE making the evolution of the channel more consistent, which becomes crucial in the antenna orientation estimation.

5.1 Introduction

The continuously increasing demand on high throughput wireless communication has forced the communication technology to integrate more and more antennas at both BS and UE sides to exploit the advantages of the MIMO technology to increase the capacity of the wireless channel. From the BS side, the massive MIMO technology, as one of the key technologies for 5G networks, tends to integrate even hundreds of antennas at one BS. Ericsson, Huawei, and Facebook have demonstrated massive MIMO systems with as many as 96 to 128 antennas (Ericsson, 2018; Huawei, 2017; Facebook, 2016). From the UE side, the existing flagman smartphones such as Samsung S8, Note9, Sony XZ, Pixel 2 already have four antennas (Samsung, 2018). In 2018, Qualcomm has unveiled the first mmWave 5G antennas for smartphones, and its Snapdragon X50 modem can support up to 16 antennas in one smartphone (Qualcomm, 2018). It is undoubted that more and more antennas will be added to both UEs and BSs in the near future.

While the trend in the increasing of the number of antennas at the UE side is evident, having more antennas for transmission will not only increase the hardware complexity and consume more energy, but also make the pilot contamination problem even worse (Jose *et al.*, 2011). Hence, leading UE producers are putting efforts to optimize the antenna design by limiting the number of antennas for transmission, so only a subset of the antennas is used for transmission, and the others are receive-only. A UE with a number of antennas simply performs a weighted summation of signals from antennas with similar channels during signal reception. Since only a subset of antennas is used for transmission, the BS inevitably measures an incomplete channel. Hence, the available channel capacity becomes smaller than the capacity of the full channel where all UE's antennas are involved in transmission, and the increase in throughput can be minuscule.

The question investigated in this chapter is: *is it possible to reconstruct the full downlink channel between all antennas at a UE and a BS based on only the incomplete uplink channel measurements obtained from the subset of transmitting antennas at the UE?* A possible approach in the DL channel reconstruction is to use the frequency-independent reciprocity on propagation paths, which implies that UL and DL signals traverse through the same paths. This approach has been proposed to eliminate or significantly reduce the overhead caused by DL channel estimation feedback (Vasisht *et al.*, 2016; Han *et al.*, 2018). Using the parameters of the propagation paths (Li *et al.*, 2017; Salmi *et al.*, 2009; Fedorov *et al.*, 2018; Fleury *et al.*, 1999), the DL channel can be

inferred using UL channel measurements. However, such an approach becomes inapplicable for the receive-only antennas since the BS cannot directly obtain the information about the propagation parameters for the receive-only antennas. Hence, the BS has to at first obtain the location and orientation of non-transmitting antennas, and only then infer propagation parameters.

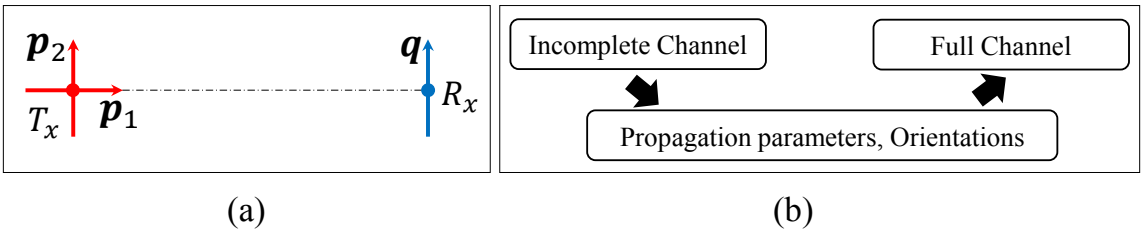

Figure 5.1: (a) The impact of the mutual orientations of the transmitting antenna (T_x) and the receiving antenna (R_x) on the channel. (b) Reconstructing the full channel by inferring propagation parameters and orientations in ARDI.

Since the form factor of a UE is usually small especially for smartphones, it is commonly assumed that the channels for different antennas are similar. However, as illustrated in Figure 5.1(a), the channels for transmitting antennas with orientations $\boldsymbol{p}_1$ and $\boldsymbol{p}_2$ are significantly different, they are perpendicular to each other. The reception from the antenna with orientation $\boldsymbol{p}_1$ is almost equal to zero since it is perpendicular to the orientation of the receiving antenna $\boldsymbol{q}$. This example shows that, even if the parameters of propagation paths are known, the channel for a receive-only antenna cannot be inferred due to unknown orientation, which can significantly affect the channel reconstruction.

Novelty and Contribution: In this chapter, a novel channel reconstruction scheme ARDI (**A**ntenna orientation **R**econstruction and **D**ownlink channel **I**nference) is designed that can reconstruct the full DL channel based on incomplete UL channel measurements. The scheme is named after early human-like female anthropoid Ardi, which is dated as 4.4 million years old (Gibbons, 2009). The heart of ARDI is the reconstruction of a UE transmitting antenna orientation at the BS side based on only UL signals. It is observed that the channel response is closely related to the mutual orientations of transmitting and receiving antennas. This observation has allowed designing an algorithm that enables the BS to use channel response as a measurement and calculate the orientation of transmitting antennas of UE based on the electromagnetic signal propagation model. Since the layout of the antennas at a UE is known based

on the UE models, the orientations and other propagation parameters for the non-transmitting antennas can then be inferred, based on which the full downlink channel can be reconstructed.

To the best of my knowledge, ARDI is the first scheme that can reconstruct the orientation of an antenna based on a single electromagnetic impulse in both single-path and multipath propagation environments. The derived solution has a closed-form expression for antenna orientation reconstruction in both propagation environments. Although there are some works on antenna array orientation reconstruction (Shahmansoori *et al.*, 2018; Talvitie *et al.*, 2017), none of them can reconstruct the orientation of a single antenna or reconstruct the orientation of a UE based on two transmitting antennas. Also, ARDI is the first scheme that can reconstruct DL channels for non-transmitting antennas. There are some existing works on the DL channel reconstruction (Vasisht *et al.*, 2016; Han *et al.*, 2018), but all of them consider only a single antenna at UEs.

In addition, ARDI is designed to make the radio channel deterministic Eqn. (2.2) via linking the physical environment where signals propagate and the channel transformation that signals experience during their traverse from a transmitter to a receiver (Figure 5.2). Hence, it is capable of inferring channels in different frequency bands as well as for different positions and time moments. The suitability of the scheme in both FDD and TDD modes will be explained in later sections.

5.2 Overview of ARDI

As illustrated in Figure 5.3, the BS has N antennas, and the UE has M antennas, from which only m antennas can transmit ($M = 4$ and $m = 2$ in the example given in Figure 5.3). The aim of this chapter is to design a scheme that increases the downlink channel capacity by expanding the downlink channel from $m \times N$ to $M \times N$.

The **key idea** of ARDI is to reconstruct the full $M \times N$ DL channel based on the spatial information such as propagation paths, locations, and orientations of the antennas inferred based on the UL signals from the transmitting antennas at the UE to the antennas at the BS. Figure 5.4 shows the flowchart of ARDI. Firstly, the BS estimates the propagation parameters of the transmitting antennas such as propagation paths, antenna location, and Doppler effect, and then it reconstructs orientations of the transmitting antennas based on the estimated propagation parameters. Based on the orientations and the propagation parameters, the BS further infers the multipath

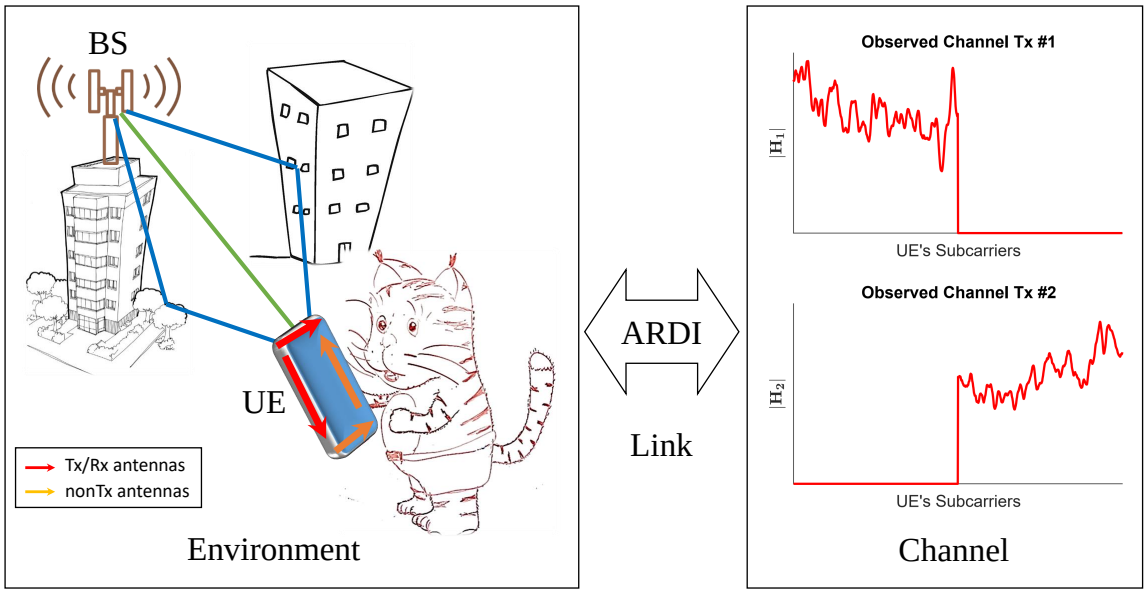

Figure 5.2: The BS is observing channels $|\mathbf{H_1}|$ and $|\mathbf{H_2}|$ from the two transmitting antennas depicted in red. Using the observation, ARDI links the propagation environment with the channel and becomes capable of inferring channels for non-transmitting antennas depicted in orange.

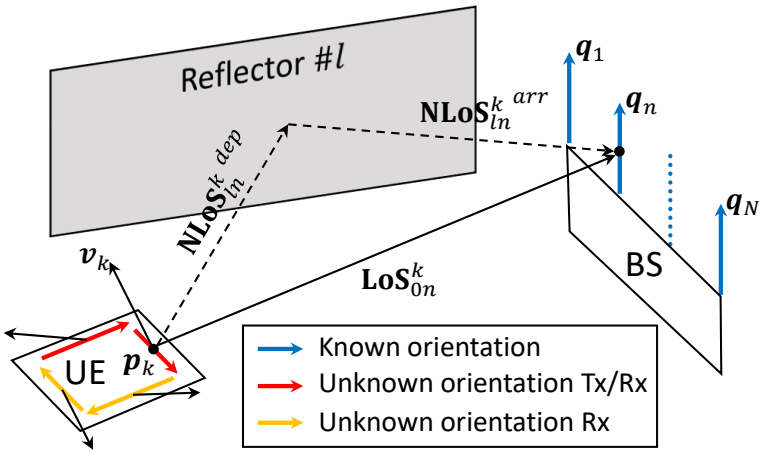

Figure 5.3: Communication between a UE and a BS.

propagation parameters and orientations for the non-transmitting antennas, and finally reconstruct the full $M \times N$ DL channel based on the estimated propagation parameters.

The description of the flowchart starts from the basic antenna theory (Orfanidis, 2014) and then transitions to the standard wireless communication theory. At first, the basics on generation and reception of signals by antennas are introduced to design a solution for reconstruction of orientation of a transmitting antenna. Then, the con-

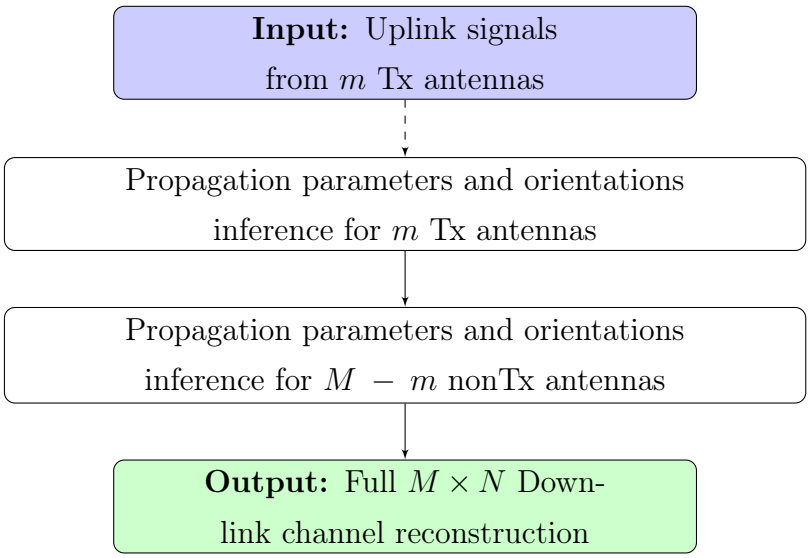

Figure 5.4: Steps for reconstructing the full downlink channel.

structed solution is integrated into a massive MIMO LTE system. For this purpose, an advancement in the massive MIMO channel modeling will be required to complement the described channel model from Chapter 3.

5.3 Antenna Orientation Reconstruction

This section describes the derivation of the solution for a massive MIMO BS to reconstruct the orientation of a transmitting antenna of a UE based on only the measurements of the uplink signals. The solution is motivated by the *strong relation between the voltage induced at a receiving antenna and the mutual orientation of the transmitting and receiving antennas* (Afraimovich *et al.*, 1999). This relation is illustrated in Figure 5.5 where black and blue segments represent transmitting and receiving antennas, respectively.

As shown in Figure 5.5, a transmitting antenna centered at T_x with orientation $\boldsymbol{p}$ emits an electromagnetic signal that is received by a receiving antenna centered at R_x with orientation $\boldsymbol{q}$, where $\boldsymbol{p}$ and $\boldsymbol{q}$ are unit length vectors. Let $\overline{T_xR_x}$ be the line that connects the centers of the two antennas. $S_{\boldsymbol{p}}$ is the plane determined by $\boldsymbol{p}$ and $\overline{T_xR_x}$, and $S_{\boldsymbol{q}}$ is the plane determined by $\boldsymbol{q}$ and $\overline{T_xR_x}$. θ^{tx} is the angle between $\boldsymbol{p}$ and $\overline{T_xR_x}$, and θ^{rx} is the angle between $\boldsymbol{q}$ and $\overline{T_xR_x}$. The electric field generated by the transmitting antenna is propagated in the $S_{\boldsymbol{p}}$ plane (the black sinusoid) and attenuated according to θ^{tx}. However, only the portion of the electric field that is projected to

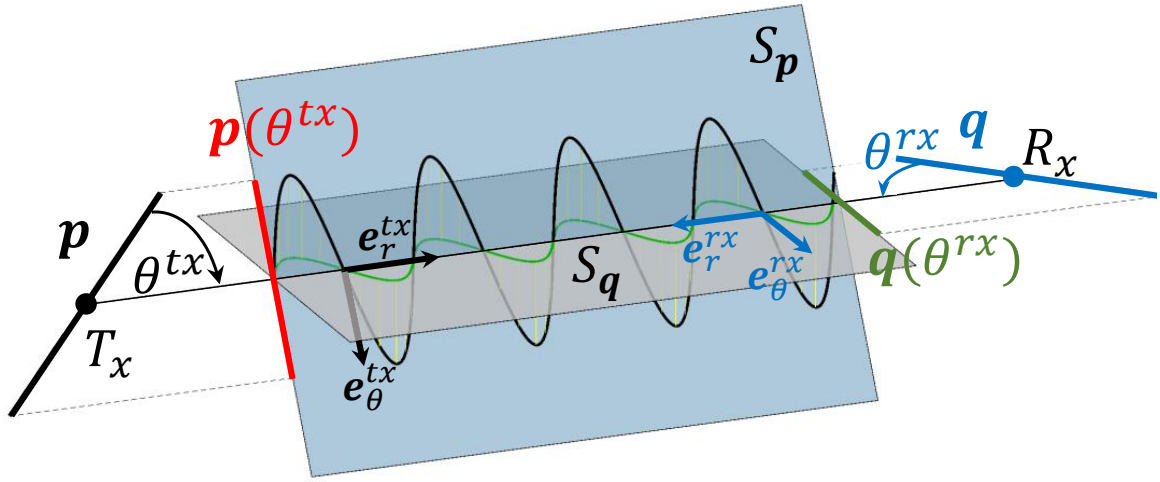

Figure 5.5: Definition of the effective lengths and the electric field projections.

plane $S_{\boldsymbol{q}}$ (the green sinusoid) can contribute to the voltage induction at the receiving antenna, and that portion is further attenuated according to angle θ^{rx}. The projection from $S_{\boldsymbol{p}}$ to $S_{\boldsymbol{q}}$ is illustrated by thin yellow lines. Consequently, the mutual orientation of the communicating antennas has a big impact on the voltage induced at the receiving antenna.

The **key idea** of the proposed solution is to reconstruct the orientation of a transmitting antenna based on the voltage measurements by exploring the above relation. For a BS with a massive MIMO antenna array, the voltages induced from the uplink signals can be measured on the distributed antenna elements. The spatially diversified voltage measurements allow reconstructing the orientation of the transmitting antenna.

Based on the Hertzian dipole antenna model with the length of d (Orfanidis, 2014), closed-form equations for the reconstruction of antenna orientation in the single-path LoS scenario is derived and then extended the reconstruction methodology to the multipath propagation scenario.

5.3.1 Single-Path LoS Case

Let r be the Euclidean distance between the two communicating antennas. As illustrated in Figure 5.5, the notation $\boldsymbol{e}_r^{tx}$ is used to represent the unit vector for the direction of the wave propagation from T_x to R_x, and $\boldsymbol{e}_\theta^{tx}$ is used to represent the unit vector for signal polarization that is always perpendicular to $\boldsymbol{e}_r^{tx}$ (Orfanidis, 2014;

Stratton, 1941). In the same way, vectors $\boldsymbol{e}_r^{rx}$ and $\boldsymbol{e}_\theta^{rx}$ are defined for the receiving antenna. The triples $(\boldsymbol{e}_r^{tx}, \boldsymbol{e}_\theta^{tx}, \boldsymbol{e}_\varphi^{tx})$ and $(\boldsymbol{e}_r^{rx}, \boldsymbol{e}_\theta^{rx}, \boldsymbol{e}_\varphi^{rx})$ are constructed according to the local spherical coordinates defined relative to the transmitting and receiving antennas, respectively (Figure 3.4). Since the dipole antenna model is considered, the observed electric field from angle θ^{tx} is oscillating within plane $S_{\boldsymbol{p}}$. It means that the observed electric field can be considered as if it is transmitted from an antenna $\boldsymbol{p}(\theta^{tx})$ with orientation $\boldsymbol{e}_\theta^{tx}$ and length $d \sin\theta^{tx}$. In Figure 5.5, $\boldsymbol{p}(\theta^{tx})$ is represented by the red line in plane $S_{\boldsymbol{p}}$. In the antenna theory, vector

$$\boldsymbol{p}(\theta^{tx}) = d \sin\theta^{tx} \boldsymbol{e}_\theta^{tx}$$

is called as the effective length of the transmitting antenna at T_x, and firstly was introduced by George Sinclair in 1950 (Sinclair, 1950). Let $\boldsymbol{E}(R_x)$ be the electric field oscillating in $S_{\boldsymbol{p}}$ near the receiving antenna. $\boldsymbol{E}(R_x)$ can be defined as

$$\boldsymbol{E}(R_x) = \frac{j\kappa\eta}{4\pi r} \mathrm{I_{in}} e^{-j\kappa r} \boldsymbol{p}(\theta^{tx}) = E(r) d \sin\theta^{tx} \boldsymbol{e}_\theta^{tx}, \tag{5.1}$$

where $E(r) = \frac{j\kappa\eta}{4\pi r} \mathrm{I_{in}} e^{-j\kappa r}$ is the scalar part of the electric field measured in Volts/meter^2, and it is a function of the propagation distance r between the two communicating antennas and the amplitude of the input current to the transmitting antenna $\mathrm{I_{in}}$; $\kappa = \omega/c$ is the wavenumber, ω is the frequency of the signal's carrier in radians ($\omega = 2\pi\mathrm{F}$), c is the speed of light, η is the characteristic impedance of air (Orfanidis, 2014).

Since the receiving antenna can receive the electric field oscillating within plane $S_{\boldsymbol{q}}$, only the portion of the electric field projected from $S_{\boldsymbol{p}}$ to plane $S_{\boldsymbol{q}}$ can be received by the receiving antenna and contribute to voltage induction. The amplitude of the projection of the electric field from $S_{\boldsymbol{p}}$ into $S_{\boldsymbol{q}}$ is the scalar product of $\boldsymbol{E}(R_x)$ with $\boldsymbol{e}_\theta^{rx}$. Due to the reception angle θ^{rx}, the maximum energy reception is further restricted by the effective length of the receiving antenna

$$\boldsymbol{q}(\theta^{rx}) = d \sin\theta^{rx} \boldsymbol{e}_\theta^{rx}, \tag{5.2}$$

which is represented by the green line in Figure 5.5. Hence, the voltage induced at the receiving antenna, denoted by V, can be derived by the scalar product of electric field $\boldsymbol{E}(R_x)$ and receiver's effective length $\boldsymbol{q}(\theta^{rx})$ as follows:

$$V = \boldsymbol{E}(R_x) \cdot \boldsymbol{q}(\theta^{rx}). \tag{5.3}$$

Substituting formulas Eqn. (5.1) and Eqn. (5.2) into Eqn. (5.3), the induced voltage can be represented as follows:

$$V = d^2 E(r) \sin\theta^{tx} \sin\theta^{rx} \, (\boldsymbol{e}_\theta^{tx} \cdot \boldsymbol{e}_\theta^{rx}). \tag{5.4}$$

Remarks: It can be seen from Eqn. (5.4) that no voltage can be induced when $\sin\theta^{tx} = 0$ and (or) $\sin\theta^{rx} = 0$, thereby zeroing out the signal at the receiving antenna. The maximum amplitude for the induced voltage over a given distance r can be obtained if the two antennas are in the same plane and both $\sin\theta^{tx}$ and $\sin\theta^{rx}$ are equal to 1 or -1. Hence, the mutual orientations and locations of the communicating antennas have a direct impact on the measured voltage through distance r, observation and reception angles θ^{tx} and θ^{rx}.

The target is to extract the orientation of the transmitting antenna from the measured voltage. In the current expression Eqn. (5.4), the orientation does not take part. However, $\boldsymbol{e}_\theta^{tx}$ can be represented via orientation vector $\boldsymbol{p}$ and radius vector $\boldsymbol{e}_r^{tx}$. Following the rules of the vector product and the illustration in Figure 5.5, it is well seen that the unit vector $\boldsymbol{e}_\theta^{tx}$ can be defined as follows:

$$\boldsymbol{e}_\theta^{tx} = \frac{(\boldsymbol{p} \times \boldsymbol{e}_r^{tx}) \times \boldsymbol{e}_r^{tx}}{\|(\boldsymbol{p} \times \boldsymbol{e}_r^{tx}) \times \boldsymbol{e}_r^{tx}\|}. \tag{5.5}$$

The numerator in Eqn. (5.5) can be rewritten using the properties of triple product properties (Gel'fand, 1989) as follows:

$$(\boldsymbol{p} \times \boldsymbol{e}_r^{tx}) \times \boldsymbol{e}_r^{tx} = (\boldsymbol{p} \cdot \boldsymbol{e}_r^{tx})\, \boldsymbol{e}_r^{tx} - \boldsymbol{p}. \tag{5.6}$$

The same result can be obtained from a geometrical representation of vectors. As illustrated in Figure 5.6, vector $\boldsymbol{p}_\theta$ that is parallel to $\boldsymbol{e}_\theta^{tx}$ can be represented through subtraction $\boldsymbol{p}$ from its projection $\boldsymbol{p}_r$ to radius vector $\boldsymbol{e}_r^{tx}$. The projection of $\boldsymbol{p}$ to $\boldsymbol{e}_r^{tx}$ can be represented as $\boldsymbol{p}_r = (\boldsymbol{p} \cdot \boldsymbol{e}_r^{tx})\, \boldsymbol{e}_r^{tx}$, consequently, $\boldsymbol{p}_\theta = (\boldsymbol{p} \cdot \boldsymbol{e}_r^{tx})\, \boldsymbol{e}_r^{tx} - \boldsymbol{p}$. The value of denominator in Eqn. (5.5) is nothing but the length of $\|\boldsymbol{p}_\theta\| = \sin\theta^{tx}$, as illustrated in Figure 5.6. Consequently, $\boldsymbol{e}_\theta^{tx}$ can be represented as follows:

$$\boldsymbol{e}_\theta^{tx} = \frac{(\boldsymbol{p} \cdot \boldsymbol{e}_r^{tx})\, \boldsymbol{e}_r^{tx} - \boldsymbol{p}}{\sin\theta^{tx}}. \tag{5.7}$$

Further, it can be noted that for any nonzero column vectors $\boldsymbol{e} = (e_1, e_2, e_3)^T$ and $\boldsymbol{p} = (p_1, p_2, p_3)^T$ the equality is held:

$$(\boldsymbol{p} \cdot \boldsymbol{e})\boldsymbol{e} = (\boldsymbol{e}\boldsymbol{e}^T)\boldsymbol{p}. \tag{5.8}$$

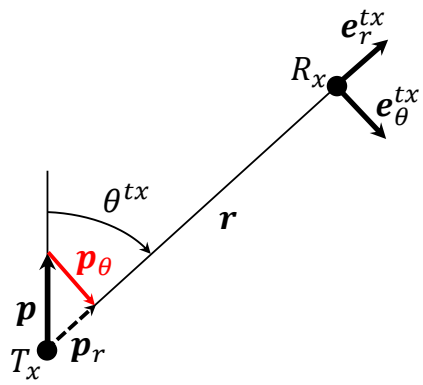

Figure 5.6: Definition of projections $\boldsymbol{p}_r$ and $\boldsymbol{p}_\theta$ to $\boldsymbol{e}_r^{tx}$ and $\boldsymbol{e}_\theta^{tx}$, respectively.

The element-wise derivation of $(\boldsymbol{p} \cdot \boldsymbol{e})\boldsymbol{e}$ gives the following:

$$\left((p_1, p_2, p_3) \begin{pmatrix} e_1 \\ e_2 \\ e_3 \end{pmatrix} \right) \begin{pmatrix} e_1 \\ e_2 \\ e_3 \end{pmatrix} = \begin{pmatrix} p_1 e_1\, e_1 & p_2 e_2\, e_1 & p_3 e_3\, e_1 \\ p_1 e_1\, e_2 & p_2 e_2\, e_2 & p_3 e_3\, e_2 \\ p_1 e_1\, e_3 & p_2 e_2\, e_3 & p_3 e_3\, e_3 \end{pmatrix} =$$

$$= \begin{pmatrix} e_1^2 & e_2 e_1 & e_3 e_1 \\ e_2 e_1 & e_2^2 & e_3 e_2 \\ e_3 e_1 & e_3 e_2 & e_3^2 \end{pmatrix} \begin{pmatrix} p_1 \\ p_2 \\ p_3 \end{pmatrix} = \left(\begin{pmatrix} e_1 \\ e_2 \\ e_3 \end{pmatrix} (e_1, e_2, e_3) \right) \begin{pmatrix} p_1 \\ p_2 \\ p_3 \end{pmatrix},$$

which is exactly equal to $(\boldsymbol{e}\boldsymbol{e}^T)\boldsymbol{p}$.

Following this rule, the equation (5.7) can be transformed as follows:

$$\boldsymbol{e}_\theta^{tx} = \left(\boldsymbol{e}_r^{tx} (\boldsymbol{e}_r^{tx})^T - I \right) \frac{1}{\sin \theta^{tx}} \boldsymbol{p}, \tag{5.9}$$

where I is the identity matrix. For the sake of writing simplicity, the following projection matrix is defined:

$$\mathrm{Pr}^{tx} = \boldsymbol{e}_r^{tx} (\boldsymbol{e}_r^{tx})^T - I,$$

which projects vectors to $\boldsymbol{e}_\theta^{tx}$. Finally, unit vector $\boldsymbol{e}_\theta^{tx}$ can be expressed through transmitter's orientation vector $\boldsymbol{p}$ as follows:

$$\boldsymbol{e}_\theta^{tx} = \mathrm{Pr}^{tx} \frac{1}{\sin \theta^{tx}} \boldsymbol{p}. \tag{5.10}$$

In the same way, unit vector $\boldsymbol{e}_\theta^{rx}$ can be expressed through receiver's orientation vector $\boldsymbol{q}$ as follows:

$$\boldsymbol{e}_\theta^{rx} = \mathrm{Pr}^{rx} \frac{1}{\sin \theta^{rx}} \boldsymbol{q}, \tag{5.11}$$

where $\mathrm{Pr}^{rx} = \boldsymbol{e}_r^{rx} (\boldsymbol{e}_r^{rx})^T - I$ is projection matrix that projects vectors to $\boldsymbol{e}_\theta^{rx}$.

By substituting $\boldsymbol{e}_\theta^{tx}$ and $\boldsymbol{e}_\theta^{rx}$ in (5.4), the induced voltage can be represented as follows:

$$V = d^2 E(r) \left(\mathrm{Pr}^{rx}\boldsymbol{q} \cdot \mathrm{Pr}^{tx}\boldsymbol{p}\right) = \boldsymbol{q}^T \mathrm{Pr}^{rx} d^2 E(r) \mathrm{Pr}^{tx} \boldsymbol{p}, \tag{5.12}$$

since scalar product $\boldsymbol{a} \cdot \boldsymbol{b} = \boldsymbol{a}^T \boldsymbol{b}$ and $(\mathrm{Pr}^{rx})^T = \mathrm{Pr}^{rx}$.

Let V_n be the voltage measured from the n-th antenna, and

$$\mathrm{Path}_n = \boldsymbol{q}_n^T \mathrm{Pr}_n^{rx} \, d^2 E(r_n) \, \mathrm{Pr}_n^{tx}$$

where r_n is the distance between the transmitting antenna at the UE and the n-th antenna at the BS. The notation "Path" is chosen because it represents the transformation that a signal is experiencing during the propagation from a transmitting antenna to a receiving antenna. For a massive MIMO antenna array with N elements, Eqn. (5.12) can be rewritten as follows:

$$\begin{pmatrix} V_1 \\ V_2 \\ \vdots \\ V_N \end{pmatrix} = \begin{pmatrix} \mathrm{Path}_1 \\ \mathrm{Path}_2 \\ \vdots \\ \mathrm{Path}_N \end{pmatrix} \boldsymbol{p}. \tag{5.13}$$

It can be seen from the system of equations (5.13) that the left side of the system consists of the real measurements on voltages from the massive MIMO antenna array, whereas the right side consists of the reconstructed voltages based on location T_x and orientation $\boldsymbol{p}$ of the transmitting antenna. Hence, the problem to find both the location and orientation of the transmitting antenna can be formulated as the following minimization problem:

$$\min_{T_x, \boldsymbol{p}} \|\boldsymbol{V} - \mathbf{Path}\, \boldsymbol{p}\|^2, \tag{5.14}$$

where $\mathbf{Path} = (\mathrm{Path}_1^T, .., \mathrm{Path}_N^T)^T$ and $\boldsymbol{V} = (V_1, .., V_N)^T$. Since both the location and orientation of each receiving antenna at the BS are known, the unknown parameters in Eqn. (5.14) include: 3 parameters for the location of the transmitting antenna and another 3 parameters for its orientation.

Theoretically, both the location and the orientation can be obtained if $N \geq 6$. However, it is worth noting that both Pr^{tx} and Pr^{rx} are nonlinear functions of the location of the transmitting antenna. Hence, problem (5.14) becomes a nonlinear optimization problem, which is much harder to solve than linear programs. In practice, the problem (5.14) can be solved in two stages. The first stage is to find the location of the transmitting antenna. The location can be found based on the localization solution described in Chapter 4. Once the location is known, matrix **Path** becomes known and

the only unknown in Eqn. (5.13) is $\boldsymbol{p}$. In this case, orientation $\boldsymbol{p}$ can be found using the standard least squares method as follows:

$$\tilde{\boldsymbol{p}} = \mathrm{Re}\{(\mathbf{Path}^T\mathbf{Path})^{-1}\mathbf{Path}^T\boldsymbol{V}\}. \tag{5.15}$$

The real part of the solution is extracted since an antenna orientation is a real valued vector by the definition and the least squares method may give a complex valued solution.

The solution given in Eqn. (5.15) is a closed-form solution for the reconstruction of the antenna orientation in the case of a LoS propagation. To my knowledge, this is the first time when a closed-form solution for antenna orientation reconstruction is derived.

5.3.2 Multi-Path Case

In a multipath propagation environment, an antenna can receive a number of copies of the transmitted signal due to signal reflections from reflecting objects. In the same way as in Chapter 3, in this chapter, the ray tracing approach is also used for modeling multipath propagation, by which the orientation of the transmitting antenna can be explicitly tracked during reflection. In the same way as in Chapter 3, reflections with two or more bounces are not considered because in most practical cases the energy of a transmitted signal drops sharply after the second reflection according to the Fresnel coefficients of reflection (Landron *et al.*, 1996; Raschkowski *et al.*, 2015).

As illustrated in Figure 5.7, a transmitted signal is reflected from surface S_1 with normal vector $\boldsymbol{n}_1$. According to the Law of Reflection, the reflection is proceeding in S_2 with normal vector $\boldsymbol{n}_2$, and K is the reflection point. Superscript "b" is used to indicate vectors corresponding to the signal *before* reflection and superscript "a" is used for the vectors corresponding to the signal *after* reflection. For a LoS path, $\boldsymbol{e}_r^{tx} = -\boldsymbol{e}_r^{rx}$. For a NLoS path, $\boldsymbol{e}_r^{tx} = \boldsymbol{e}_r^{b}$ and $\boldsymbol{e}_r^{rx} = -\boldsymbol{e}_r^{a}$. This reflection model is slightly differ from the model described in Chapter 3. The main difference is that the reflected signal is bearing the information about the transmitting antenna orientation, which can be extracted at the receiver side.

The main challenge for the antenna orientation reconstruction in the multipath case is to take into account the transformation of the electric field vector (5.1) during reflection. The electric field $\boldsymbol{E}^b(K)$ at point K before the reflection can be decomposed into the following two components that transform differently due to the physical properties of the reflecting surface: *(1)* the perpendicular component $\boldsymbol{E}_\perp^b(K)$ that is

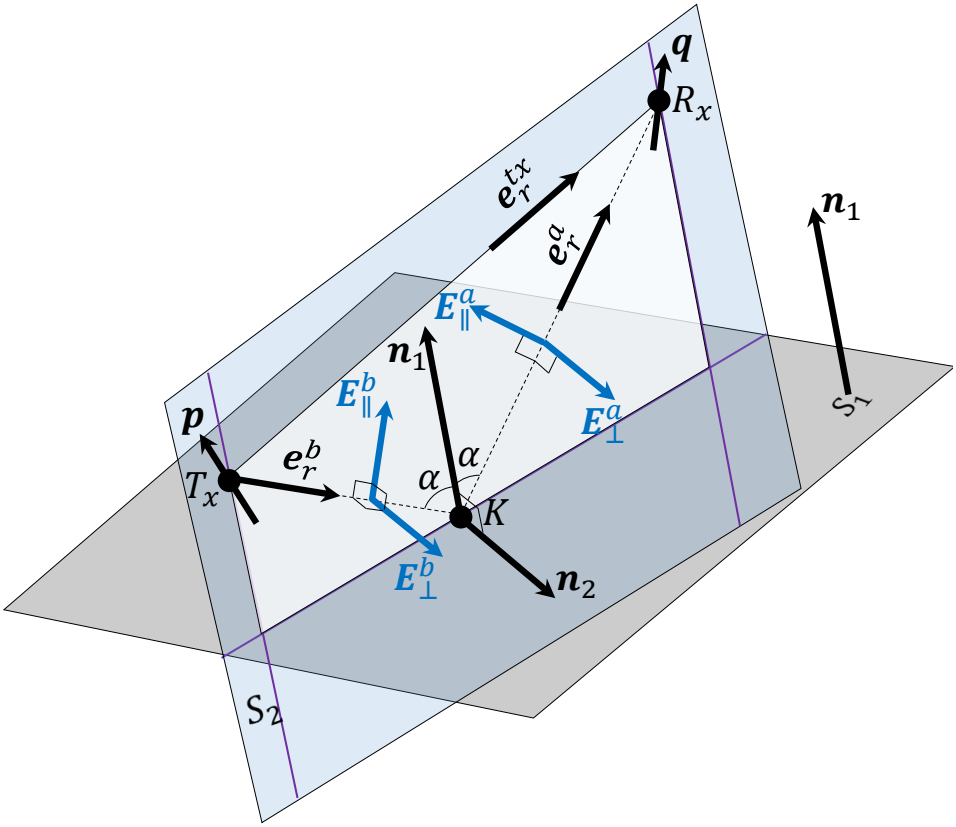

Figure 5.7: Definition of vectors in the case of reflection.

perpendicular to S_2, and *(2)* the parallel component $\boldsymbol{E}_\parallel^b(K)$ that is within S_2. The perpendicular component of the electric field has the following expression:

$$\boldsymbol{E}_\perp^b(K) = (\boldsymbol{E}^b(K) \cdot \boldsymbol{n}_2)\boldsymbol{n}_2,$$

and the parallel component is simply represented as follows:

$$\boldsymbol{E}_\parallel^b(K) = \boldsymbol{E}^b(K) - \boldsymbol{E}_\perp^b(K).$$

Based on the property of the scalar product Eqn. (5.8), the perpendicular component can be transformed as

$$\boldsymbol{E}_\perp^b(K) = (\boldsymbol{n}_2\boldsymbol{n}_2^T)\boldsymbol{E}^b(K).$$

According to the electric field vector given in Eqn. (5.1) and taking into account Eqn. (5.10), the two components of the electric field at point K before reflection can be computed as follows:

$$\boldsymbol{E}_\perp^b(K) = dE(r^K)(\boldsymbol{n}_2\boldsymbol{n}_2^T)\mathrm{Pr}^b\boldsymbol{p}, \tag{5.16}$$

$$\boldsymbol{E}_\parallel^b(K) = dE(r^K)(I - \boldsymbol{n}_2\boldsymbol{n}_2^T)\mathrm{Pr}^b\boldsymbol{p}, \tag{5.17}$$

where r^K is the distance from T_x to reflection point K, and $\mathrm{Pr}^b = \boldsymbol{e}_r^b(\boldsymbol{e}_r^b)^T - I$ is the projection matrix as in Eqn. (5.10).

After reflection, the perpendicular component attenuates with Fresnel reflection coefficient $\Gamma_\perp(\alpha)$ (Raschkowski *et al.*, 2015) where α is the angle of incident. The parallel component rotates in plane S_2 clockwise with angle $\pi - 2\alpha$ to become perpendicular to the propagation direction $\boldsymbol{e}_r^a$ and attenuates with Fresnel reflection coefficient $\Gamma_\parallel(\alpha)$ (Raschkowski *et al.*, 2015). Hence, the two components after reflection can be represented as follows:

$$\begin{aligned} \boldsymbol{E}_\perp^a(K) &= \Gamma_\perp(\alpha)\, \boldsymbol{E}_\perp^b(K) \\ &= \Gamma_\perp(\alpha)\, dE(r^K)(\boldsymbol{n}_2\boldsymbol{n}_2^T)\mathrm{Pr}^b\boldsymbol{p}, \end{aligned} \tag{5.18}$$

$$\begin{aligned} \boldsymbol{E}_\parallel^a(K) &= \Gamma_\parallel(\alpha)\, W(\boldsymbol{n}_2, \pi - 2\alpha)\boldsymbol{E}_\parallel^b(K) \\ &= \Gamma_\parallel(\alpha)\, W(\boldsymbol{n}_2, \pi - 2\alpha)dE(r^K)(I - \boldsymbol{n}_2\boldsymbol{n}_2^T)\mathrm{Pr}^b\boldsymbol{p}, \end{aligned} \tag{5.19}$$

where $W(\boldsymbol{n}_2, \pi - 2\alpha)$ is the rotation matrix that rotates vectors around the normal vector $\boldsymbol{n}_2$ with angle $\pi - 2\alpha$ (Gel'fand, 1989). The main observation is that, in the case of NLoS propagation, in addition to the propagation attenuation, the electric field experiences additional attenuation caused by the reflection phenomenon. The Fresnel coefficients $\Gamma_\perp(\alpha)$ and $\Gamma_\parallel(\alpha)$ depend on angle of incident α and the physical properties of a reflecting surface (Raschkowski *et al.*, 2015).

The transformed electric field defined by $\boldsymbol{E}_\perp^a(K)$ and $\boldsymbol{E}_\parallel^a(K)$ experiences further attenuation during the propagation in the direction $\boldsymbol{e}_r^a$ from the reflection point K to the receiver point R_x. The portion of the electric field received by the receiving antenna is restricted by the effective length of the receiving antenna, which can be expressed as

$$\boldsymbol{q}(\theta_r^a) = d\,\mathrm{Pr}^a\,\boldsymbol{q}$$

based on the definition of the effective length and (5.11). Here, the projection matrix Pr^a is expressed as $\mathrm{Pr}^a = \boldsymbol{e}_r^a(\boldsymbol{e}_r^a)^T - I$. In the same way as that in the LoS path case, the voltage induced by the electric field propagating along an NLoS path can be computed as follows:

$$V^{NLoS} = \boldsymbol{q}^T\mathrm{Pr}^a\boldsymbol{E}^a(R_x) = \boldsymbol{q}^T\mathbf{NLoS}\,\boldsymbol{p}, \tag{5.20}$$

where $\boldsymbol{E}^a(R_x) = \boldsymbol{E}_\perp^a(R_x) + \boldsymbol{E}_\parallel^a(R_x)$, and **NLoS** is the electric field transformation matrix defined as follows:

$$\begin{aligned} \mathbf{NLoS} = d^2\,\mathrm{Pr}^a\,E(r^{NLoS})\,\big[&\Gamma_\perp(\alpha)(\boldsymbol{n}_2\boldsymbol{n}_2^T) + \\ &+ \Gamma_\parallel(\alpha)\,W(\boldsymbol{n}_2, \pi - 2\alpha)(I - \boldsymbol{n}_2\boldsymbol{n}_2^T)\big]\,\mathrm{Pr}^b. \end{aligned} \tag{5.21}$$

Here r^{NLoS} is the total covered distance of the NLoS path.

For the LoS path, its transformation matrix is $\mathbf{LoS} = d^2 \mathrm{Pr}^{rx} E(r^{LoS}) \mathrm{Pr}^{tx}$, and (5.12) can be written as:

$$V^{LoS} = \boldsymbol{q}^T \, \mathbf{LoS} \, \boldsymbol{p}. \tag{5.22}$$

Assume the multipath signal propagation has L NLoS paths. For each NLoS path and the LoS path, the receiving antenna has the corresponding vector of effective length. Consequently, the total voltage produced on the receiving antenna can be represented as follows:

$$\begin{aligned} V &= \boldsymbol{q}^T \left[\mathbf{LoS} + \sum_{l=1}^{L} \mathbf{NLoS}_l \right] \boldsymbol{p} = \\ &= V^{LoS} + \sum_{l=1}^{L} V_l^{NLoS}, \end{aligned} \tag{5.23}$$

where $\mathbf{NLoS}_l$ is the transformation matrix for the l-th NLoS path. Let

$$\mathrm{MultiPath}_n = \boldsymbol{q}_n^T \left[\mathbf{LoS}_n + \sum_{l=1}^{L} \mathbf{NLoS}_{ln} \right], \quad n \in [1, .., N]. \tag{5.24}$$

In the same way as in the LoS case, for a massive MIMO antenna array with N antennas, Eqn. (5.23) can be written as follows:

$$\begin{pmatrix} V_1 \\ V_2 \\ \vdots \\ V_N \end{pmatrix} = \begin{pmatrix} \mathrm{MultiPath}_1 \\ \mathrm{MultiPath}_2 \\ \vdots \\ \mathrm{MultiPath}_N \end{pmatrix} \boldsymbol{p}. \tag{5.25}$$

After defining $\mathbf{Path} = (\mathrm{MultiPath}_1^T, .., \mathrm{MultiPath}_N^T)^T$, both the location and orientation of the transmitting antenna can be obtained by solving problem (5.14) using the same least square approach as for the LoS case.

5.3.3 Constrained Least Square Method

In the presence of noise, the equations (5.13) and (5.25) can be represented as follows:

$$\boldsymbol{V} = \mathbf{Path} \, \boldsymbol{p} + \boldsymbol{\xi}, \tag{5.26}$$

where $\boldsymbol{\xi}$ is noise vector $\boldsymbol{\xi} = (\xi_1, .., \xi_N)^T$. The standard least squares solution does not take into account the fact that orientation vector $\boldsymbol{p}$ has unit length. Let us add the unit length constraint and formulate a constrained least square problem as follows:

$$\min_{\boldsymbol{p}} ||\mathbf{Path} \, \boldsymbol{p} - \boldsymbol{V}||_2 \quad \text{subject to} \quad ||\boldsymbol{p}||_2 = 1. \tag{5.27}$$

Here, the solution is searched on a unit spheres. Since the type of the constrain is simple, the exact solution can be derived straight forward using Lagrange multipliers (Lorenz and Boyd, 2005).

The first step in the solution search is in performing a singular value decomposition (SVD) of matrix **Path** as follows:

$$\mathbf{Path} = A\Lambda B^H$$

where $A_{N\times N}$ and $B_{3\times 3}$ are unitary matrices, and Λ is a diagonal real matrix of the same dimension as **Path**. Using the fact that the multiplication on a unitary matrix does not change the length of a vector (Gel'fand, 1989), problem (5.27) can be reformulated as follows:

$$\min_{\tilde{\boldsymbol{p}}} ||\Lambda\,\tilde{\boldsymbol{p}} - \boldsymbol{y}||_2 \quad \text{subject to} \quad ||\tilde{\boldsymbol{p}}||_2 = 1, \tag{5.28}$$

where $\tilde{\boldsymbol{p}} = B^H\boldsymbol{p}$ and $\boldsymbol{y} = A^H\boldsymbol{V}$. By applying the method of Lagrange multipliers, Lagrangian $L(\tilde{\boldsymbol{p}}, \lambda)$ is defined as follows:

$$L(\tilde{\boldsymbol{p}}, \lambda) = (\Lambda\,\tilde{\boldsymbol{p}} - \boldsymbol{y})^H(\Lambda\,\tilde{\boldsymbol{p}} - \boldsymbol{y}) + \lambda(\tilde{\boldsymbol{p}}^H\tilde{\boldsymbol{p}} - 1),$$

where λ is the Lagrange multiplier. To calculate the stationary points, $L(\tilde{\boldsymbol{p}}, \lambda)$ has to be differentiated with respect to $\tilde{\boldsymbol{p}}^H$ and λ and set the partial derivatives equal to zeros as follows:

$$\Lambda^H\Lambda\tilde{\boldsymbol{p}} - \Lambda^H\boldsymbol{y} + \lambda\tilde{\boldsymbol{p}} = 0, \tag{5.29}$$

and

$$\tilde{\boldsymbol{p}}^H\tilde{\boldsymbol{p}} - 1 = 0. \tag{5.30}$$

It can be noted that Eqn. (5.29) has an analytical solution:

$$\tilde{\boldsymbol{p}} = (\Lambda^H\Lambda + \lambda I)^{-1}\Lambda^H\boldsymbol{y}. \tag{5.31}$$

Plugging the analytical solution into Eqn. (5.30) gives

$$\boldsymbol{y}^H\Lambda(\Lambda^H\Lambda + \lambda I)^{-1}(\Lambda^H\Lambda + \lambda I)^{-1}\Lambda^H\boldsymbol{y} - 1 = 0.$$

Since Λ is diagonal matrix with the singular values of matrix Path, the last expression can be reduced as following:

$$\sum_{i=1}^{3} \frac{\sigma_i^2}{(\sigma_i^2 + \lambda)^2}|y_i|^2 = 1, \tag{5.32}$$

where $\sigma_i, i = 1, 2, 3$ are diagonal elements of matrix Λ.

Note, Eqn. (5.32) has more than one solutions. Among all the solutions, the solution λ^* that brings the minimum value for problem (5.28) is chosen. Once λ^* is found, orientation vector $\boldsymbol{p}$ can be reconstructed from $\tilde{\boldsymbol{p}}$ as following: $\boldsymbol{p} = B\tilde{\boldsymbol{p}}$.

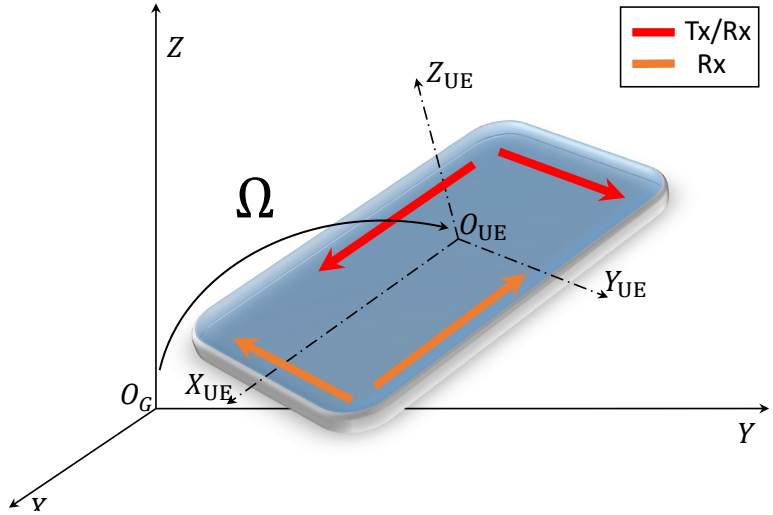

Figure 5.8: The orientation of a UE in the global coordinate system O_G.

5.4 UE Orientation Reconstruction

In order to enable the reconstruction of channels for non-transmitting antennas, at first, ARDI has to calculate positions and orientation of each antenna in the global coordinate system O_G. It can be done using the location of the UE and its orientation in the global coordinate system. This section describes how ARDI estimates the orientation of the UE during an arbitrary movement.

Relative orientations and positions of antennas in a UE are considered as known due to a known hardware design of the UE. Using the described approach from Section 5.3, orientations of the transmitting antennas can be reconstructed at the BS side via UL signals. Consequently, using the estimated orientations of the transmitting antennas, the orientation of the UE's coordinate system (or simply the orientation of UE) can be reconstructed. In an ideal situation when the m orientations are estimated without errors, the orientations of two non-parallel antennas are enough for reconstructing the UE's orientation. However, in the presence of estimation error, it is preferable to use all the estimated m orientations in order to incorporate all the observed information.

As illustrated in Figure 5.8, orientations $\boldsymbol{p}_k$ of the UE's transmitting antennas are defined in its local coordinate system O_{UE} as follows:

$$\boldsymbol{p}_k = p_{k1}\boldsymbol{e}_x^{\text{UE}} + p_{k2}\boldsymbol{e}_y^{\text{UE}} + p_{k3}\boldsymbol{e}_z^{\text{UE}}, \quad k = 1, .., M, \tag{5.33}$$

where $(\boldsymbol{e}_x^{\text{UE}}, \boldsymbol{e}_y^{\text{UE}}, \boldsymbol{e}_z^{\text{UE}})$ is the orthonormal basis of UE's coordinate system O_{UE}.

During an arbitrary movement of a mobile user, the orientation of the UE can be arbitrarily changed. The orientation change can be represented through a rotation

matrix Ω as illustrated in Figure 5.8. The UE together with its antennas is moving as a rigid body. If the basis $(\boldsymbol{e}_x^{\mathrm{UE}}, \boldsymbol{e}_y^{\mathrm{UE}}, \boldsymbol{e}_z^{\mathrm{UE}})$ rotates with the rotation matrix Ω, then orientations of antennas also rotate with the same rotation matrix. The rotation of M antennas can represented as follows:

$$\boldsymbol{p}_k' = \Omega \boldsymbol{p}_k = p_{k1}\Omega\, \boldsymbol{e}_x^{\mathrm{UE}} + p_{k2}\Omega\, \boldsymbol{e}_y^{\mathrm{UE}} + p_{k3}\Omega\, \boldsymbol{e}_z^{\mathrm{UE}}, \quad k = 1, .., M.$$

These equations can be rewritten via the projection of the rotation matrix Ω to the orthonormal basis $(\boldsymbol{e}_x^{\mathrm{UE}}, \boldsymbol{e}_y^{\mathrm{UE}}, \boldsymbol{e}_z^{\mathrm{UE}})$ as follows:

$$\boldsymbol{p}_k' = \Omega \boldsymbol{p}_k = p_{k1}\boldsymbol{\omega}_1 + p_{k2}\boldsymbol{\omega}_2 + p_{k3}\boldsymbol{\omega}_3, \quad k = 1, .., M, \tag{5.34}$$

where $(\boldsymbol{\omega}_1, \boldsymbol{\omega}_2, \boldsymbol{\omega}_3)$ are the projection vectors of Ω to the local coordinate system. If the initial orientation of O_{UE} is taken to coincide with the orientation of the global coordinate system O_G, then the rotation matrix $\Omega = (\boldsymbol{\omega}_1, \boldsymbol{\omega}_2, \boldsymbol{\omega}_3)$ can be represented through its projections.

The estimated orientations $\boldsymbol{p}_k'$ of the m transmitting antennas can be used as measurements in the system of m equations (5.34). The aim is to extract the elements of rotation matrix Ω from this system of m equations. The elementwise representation of Eqn. (5.34) can be written as follows:

$$\begin{pmatrix} p_{k1}' \\ p_{k2}' \\ p_{k3}' \end{pmatrix} = \begin{pmatrix} p_{k1}\,\omega_{11} + p_{k2}\,\omega_{12} + p_{k3}\,\omega_{13} \\ p_{k1}\,\omega_{21} + p_{k2}\,\omega_{22} + p_{k3}\,\omega_{23} \\ p_{k1}\,\omega_{31} + p_{k2}\,\omega_{32} + p_{k3}\,\omega_{33} \end{pmatrix}, \quad k = 1, .., m \tag{5.35}$$

These equation can be written in a way that the vector that consists of the rotation matrix elements ω_{ij} is separated from the matrix that consists of the orientation vector elements p_{ki}:

$$\begin{pmatrix} p_{k1}' \\ p_{k2}' \\ p_{k3}' \end{pmatrix} = \begin{pmatrix} p_{k1} & 0 & 0 & p_{k2} & 0 & 0 & p_{k3} & 0 & 0 \\ 0 & p_{k1} & 0 & 0 & p_{k2} & 0 & 0 & p_{k3} & 0 \\ 0 & 0 & p_{k1} & 0 & 0 & p_{k2} & 0 & 0 & p_{k3} \end{pmatrix} \begin{pmatrix} \boldsymbol{\omega}_1 \\ \boldsymbol{\omega}_2 \\ \boldsymbol{\omega}_3 \end{pmatrix}, \quad k = 1, .., m. \tag{5.36}$$

In a compact form these equations can be represented through the Kronecker multiplication $\otimes$ (Henderson and Searle, 1981):

$$\begin{pmatrix} p_{k1}' \\ p_{k2}' \\ p_{k3}' \end{pmatrix} = \boldsymbol{p}_k^T \otimes I_3 \begin{pmatrix} \boldsymbol{\omega}_1 \\ \boldsymbol{\omega}_2 \\ \boldsymbol{\omega}_3 \end{pmatrix}, \quad k = 1, .., m, \tag{5.37}$$

where I_3 is the unit matrix of size 3×3. For all m transmitting antennas, the above can be represented as follows:

$$\begin{pmatrix} \boldsymbol{p}'_1 \\ \vdots \\ \boldsymbol{p}'_m \end{pmatrix} = \begin{pmatrix} \boldsymbol{p}_1^T \\ \vdots \\ \boldsymbol{p}_m^T \end{pmatrix} \otimes I_3 \begin{pmatrix} \boldsymbol{\omega}_1 \\ \boldsymbol{\omega}_2 \\ \boldsymbol{\omega}_3 \end{pmatrix}, \tag{5.38}$$

Let $P = [\boldsymbol{p}_1, \boldsymbol{p}_2, .., \boldsymbol{p}_m]^T$ and $\Pi = P \otimes I_3$. If P has the full rank, then the rank Π is also full since (Brewer, 1978)

$$\operatorname{rank} \Pi = \operatorname{rank} P \operatorname{rank} I_3.$$

Hence, the system of equations (5.38) can be solved through a standard least squares method as follows:

$$\begin{pmatrix} \tilde{\boldsymbol{\omega}}_1 \\ \tilde{\boldsymbol{\omega}}_2 \\ \tilde{\boldsymbol{\omega}}_3 \end{pmatrix} = (\Pi^H \Pi)^{-1} \Pi^H \begin{pmatrix} \boldsymbol{p}'_1 \\ \vdots \\ \boldsymbol{p}'_m \end{pmatrix} \tag{5.39}$$

since $\Pi^H \Pi$ is invertible.

In the case when $\operatorname{rank} P = 2$, the matrix $\Pi^H \Pi$ becomes non-invertible. In this case, a special vector has to be constructed that makes P a full-rank matrix and keeps the relations with the rows of P during any movement. Since the rank is two, all $\boldsymbol{p}_k$ are in a plane and consequently they define this plane. The normal vector of the plane can be found using SVD of P. The smallest singular value of the decomposition corresponds to the vector $\boldsymbol{p}_{ort}$ that is perpendicular to the plane (Gel'fand, 1989), and all $\boldsymbol{p}_k$ are perpendicular to $\boldsymbol{p}_{ort}$. Due to the fact that the UE is a rigid body, P does not change its rank during an arbitrary movement. This means that $\boldsymbol{p}_{ort}$ stays perpendicular to the plane generated by the m transmitting antennas. Consequently, $\boldsymbol{p}_{ort}$ can be taken as an additional measurement in (5.38) as follows:

$$\begin{pmatrix} \boldsymbol{p}'_1 \\ \vdots \\ \boldsymbol{p}'_m \\ \boldsymbol{p}'_{ort} \end{pmatrix} = \begin{pmatrix} \boldsymbol{p}_1^T \\ \vdots \\ \boldsymbol{p}_m^T \\ \boldsymbol{p}_{ort} \end{pmatrix} \otimes I_3 \begin{pmatrix} \boldsymbol{\omega}_1 \\ \boldsymbol{\omega}_2 \\ \boldsymbol{\omega}_3 \end{pmatrix}. \tag{5.40}$$

In this case, the updated matrix Π becomes full ranked and the least squares method (5.39) can be used to find the elements of the rotation matrix.

The case where $\operatorname{rank} P < 2$ means that all transmitting antennas are oriented along one direction, i.e. parallel to each other, or there is only one transmitting antenna. In this case, the orientation cannot be reconstructed since there is uncertainty regarding

the other two directions. This special case should be considered in a combination with additional assumptions regarding the orientation, for example, a rough orientation measurements can be provided by an onboard inertial measurement unit (IMU). The investigation of this case falls to the scope of the future study, which is not considered in this thesis.

5.4.1 Recovery of the Global Orientations and Locations of M Antennas

Since the relative orientations and locations of antennas are fixed inside of a UE and known due to manufacturing documentation, the spatial information about the antennas can be reconstructed from the estimated location (from Chapter 4) and orientation (Section 5.3) of the UE. The coordinates of the UE are found based on the localization scheme described in Chapter 4. The averaged location of the m transmitting antennas is treated as the coordinates of the UE's center of gravity $\mathrm{UE}_{cg} = (x_{cg}, y_{cg}, z_{cg})^T$. Note that the orientations of the m transmitting antennas are estimated using the coordinates of the center of gravity, which means that for all transmitting antennas radius vectors $\boldsymbol{e}_r^{tx}$ are originated from the center of gravity in Section 5.3.

Once the orientation of the UE is defined, i.e. orientation matrix Ω in (5.34), the orientation of M antennas in the global coordinate system O_G can be reconstructed directly using (5.34) for all $k = 1, .., M$. Let T_x^k represents the location of k-th antenna of the UE in the local coordinate system O_{UE}. The locations of antennas can be calculated directly from the orientation and the coordinates of the center of gravity. At first, the coordinates of M antennas are rotated using the estimated rotation matrix Ω. Then, the resulting coordinates are transitioned to new locations by adding the estimated location of the center of gravity UE_{cg} as follows:

$$T_x^{k\prime} = \Omega T_x^k + \mathrm{UE}_{cg},$$

where $T_x^{k\prime}$ is the location of k-th antenna in the global coordinate system. Hence, as a result of this step, ARDI obtains locations $T_x^{k\prime}$ and orientations $\boldsymbol{p}_k'$ of all M antennas of the UE, and is ready to infer the full DL channel.

5.5 Full Downlink Channel Reconstruction

5.5.1 Channel Modeling

Let us consider the case where transmitting antennas of a UE transmit UL signals simultaneously but use different radio resource blocks (Sesia *et al.*, 2011). Hence, they do not interfere with each other at the reception side. At the physical level, signals are transmitted via the emission of electromagnetic waves from a transmitting antenna. The control of output electric field defined in (5.1) is done by controlling the input current in the time domain

$$\mathrm{I}(t) = \mathrm{I}_{in} \sum_{m=1}^{N_{\mathrm{sym}}} \mathrm{sym}_m(t) e^{j\omega t},$$

where N_{sym} is the number of transmitting symbols, $\mathrm{sym}_m(t)$ is nonzero in period $[(m-1)\Delta t, m\Delta t]$ where Δt is the system's sampling duration, and I_{in} is the amplitude of the input current to the transmitting antenna. The LoS observation of the electric field at any point X, denoted by $\boldsymbol{E}(t, X)$, is

$$\begin{aligned}\boldsymbol{E}(t, X) =& \frac{j\kappa\eta}{4\pi r}\mathrm{I}(t - r/c)\boldsymbol{p}(\theta^{tx}) = \\ =& \mathrm{I}_{in}\frac{j\kappa\eta}{4\pi r}\sum_{m=1}^{N_{\mathrm{sym}}}\mathrm{sym}_m(t-r/c)e^{j\omega(t-r/c)}\boldsymbol{p}(\theta^{tx}),\end{aligned}$$

where r is the distance between an antenna and the observation point. At the receiving antenna with orientation $\boldsymbol{q}$, this electric field induces voltage

$$V(t) = \boldsymbol{E}(t, X) \cdot \boldsymbol{q}(\theta^{rx})$$

according to Eqn. (5.4). By processing the measured voltage, the BS can reconstruct the transmitted symbols sym_m by removing the carrier wave $e^{j\omega t}$ and then estimating channel to equalize the distorted symbols. Through the procedure of channel estimation (CE) based on the reference symbols (Sesia *et al.*, 2011), the downlink channel can be represented as follows:

$$H = \mathrm{I}_{in}\frac{j\kappa\eta}{4\pi r}e^{-j\kappa r}\boldsymbol{p}(\theta^{tx}) \cdot \boldsymbol{q}(\theta^{rx}) = \mathrm{I}_{in}\mu\kappa e^{-j\kappa r}, \tag{5.41}$$

where $\mu = \frac{j\eta}{4\pi r}\boldsymbol{q}(\theta^{rx}) \cdot \boldsymbol{p}(\theta^{tx})$ can be considered as a complex-valued channel attenuation coefficient. This is another interpretation of the propagation attenuation, which differs from the massive MIMO channel modeling approach described in Chapter 3. In

accordance with Eqn. (5.4) and Eqn. (5.1), channel given in Eqn. (5.41) has the volt unit.

In mobility scenarios, the modeling of the downlink channel becomes more complicated due to the Doppler effect since an arbitrary movement in 3D space causes different velocities on each antenna. Hence, the signals sent from different antennas can experience different Doppler shifts depending on the propagation path and receiving antenna (Kihei *et al.*, 2017):

$$\nu_{ln}^{k} = (\boldsymbol{v}^{k} \cdot \boldsymbol{e}_{ln}^{k})\frac{\omega}{c} = D_{ln}^{k}\kappa, \tag{5.42}$$

where $\boldsymbol{v}^k$ is the velocity vector of the k-th antenna, $\kappa = \omega/c$ is the wavenumber, and $\boldsymbol{e}_{ln}^k$ is the unit length radius vector that indicates the direction from the k-th transmitting antenna to the n-th receiving antenna through the l-th path. Hence, in a dynamic multipath propagation environment, the channel for the signal that travels from the k-th transmitting antenna to the n-th receiving antenna can be modeled based on (5.41) and (5.42) as:

$$H_{n}^{k} = \mathrm{I}_{in} \sum_{l=0}^{L} \mu_{ln}^{k}\kappa\, e^{-j\kappa r_{ln}^{k}}\, e^{-j\nu_{ln}^{k}(r_{ln}^{k}/c)}, \tag{5.43}$$

where L is the number of propagation paths. To enable the channel reconstruction, the multipath propagation parameters $\{\mu_{ln}^k, r_{ln}^k, \nu_{ln}^k\}$ for each propagation path l from the k-th transmitting antenna to the n-th receiving antenna have to be identified. The total number of unknown multipath propagation parameters becomes larger than the number of the measured channels since there is only m ($m < M$) transmitting antennas. To find all the parameters, in the same way as in Chapter 4, the OFDM nature of the UL signals is used to increase the number of measurements (Salmi *et al.*, 2009). Consequently, the channel at subcarrier $f_i = \omega + i\Delta f$ can be represented as follows:

$$H_{n}^{k}(f_i) = \mathrm{I}_{in} \sum_{l=0}^{L} \mu_{ln}^{k}\kappa_i\, e^{-j\kappa_i\, r_{ln}^{k}}\, e^{-jD_{ln}^{k}\kappa_i(r_{ln}^{k}/c)}, \tag{5.44}$$

where r_{ln}^k and D_{ln}^k are the frequency independent parameters of distance and Doppler shift, respectively. Channel attenuation coefficients μ_{ln}^k are frequency dependent; $\kappa_i = f_i/c$, $f_i \in \mathcal{F}_k$ and $\mathcal{F}_k$ is the subset of subcarriers that is allocated for the k-th transmitting antenna, and $\cup_{k=1}^{m}\mathcal{F}_k$ is the total given radio resource.

Observation: The BS can reconstruct the downlink channels once the multipath propagation parameters $\{\mu_{ln}^k, r_{ln}^k, D_{ln}^k\}$ are obtained from (5.44) (Vasisht *et al.*, 2016). While the parameters for the transmitting antennas can be easily inferred based on the measurements of the UL signals, it is *challenging* to infer them for the non-transmitting

antennas. The following explains how to infer these parameters.

5.5.2 Parameter Estimation for Transmitting Antennas

In the same way as optimization problem (4.25) in Chapter 4, the propagation parameters $\{\mu_{ln}^k, r_{ln}^k, D_{ln}^k\}$ can be estimated by solving the following optimization problem:

$$\min_{\{\mu_{ln}^k, r_{ln}^k, D_{ln}^k\}} \sum_{i=1}^{N_s^k} \sum_{n=1}^{N} \sum_{k=1}^{m} \left\| H_n^{k\prime}(f_i) - H_n^k(f_i) \right\|^2, \tag{5.45}$$

where N_s^k is the total number of subcarriers in $\mathcal{F}_k$. This optimization problem can be solved using the approaches discussed in Chapter 4.

The main obstacle in estimating the propagation parameters is that r_{ln}^k and D_{ln}^k have to be estimated as one parameter $r_{ln}^k + D_{ln}^k(r_{ln}^k/c)$ since they cannot be separated from the exponential function $e^{-j\kappa_i(r_{ln}^k + D_{ln}^k(r_{ln}^k/c))}$. Hence, the solution of optimization problem (5.45) gives μ_{ln}^k and $r_{ln}^k + D_{ln}^k(r_{ln}^k/c)$. To further separate r_{ln}^k and D_{ln}^k, the parameters estimation has to be done twice with a time gap τ. In fact, UL channel estimation is performed twice every millisecond in LTE (Sesia *et al.*, 2011), which gives the required time diversity in the estimated parameters. Suppose the estimation for the first CE is $est_1 = r_{ln}^k + D_{ln}^k(r_{ln}^k/c)$, and at the second is $est_2 = r_{ln}^k + D_{ln}^k(r_{ln}^k/c - \tau)$. The difference between the two estimations is $est_1 - est_2 = D_{ln}^k \tau$. Since τ is known, D_{ln}^k can be extracted from the difference of two consecutive CEs. Once D_{ln}^k is extracted, r_{ln}^k can also be obtained.

Based on the SWP model, the locations of the transmitting antennas T_x^k and their images $\mathrm{Im}_l(T_x^k)$ can be found from the extracted r_{ln}^k using the Bancroft method for each image as it is done in Chapter 4. As illustrated in Figure 5.9 (a), based on the estimated locations, the reflecting plane S_l can be determined because it has to go through the middle of the segments $[T_x^k, \mathrm{Im}_l(T_x^k)]$ and be perpendicular to them. Now, to calculate the NLoS transformation matrices in (5.21), ARDI needs to calculate the angle of incidence α_{ln}^k, which can be obtained based on the location of the receiving antenna and the reflecting plane S_l. Hence, by doing the same operations for each pair of antennas (T_x^k, R_x^n) and each l-th path, ARDI can calculate the incidence angles α_{ln}^k for each NLoS path.

The CE given in (5.43) can be represented in a convenient form for orientation reconstruction as follows:

$$H_n^k = \boldsymbol{q}_n^T \left[\mathbf{LoS}\mathrm{D}_n^k + \sum_{l=1}^{L} \mathbf{NLoS}\mathrm{D}_{ln}^k \right] \boldsymbol{p}_k, \tag{5.46}$$

where the multipath transformation matrices incorporate the estimated Doppler shifts $\mathbf{LoS}\mathrm{D}_n^k = \mathbf{LoS}_n^k\, e^{-jD_{0n}^k \kappa(r_{0n}^{cg}/c)}$ and $\mathbf{NLoS}\mathrm{D}_{ln}^k = \mathbf{NLoS}_{ln}^k\, e^{-jD_{ln}^k \kappa(r_{ln}^{cg}/c)}$.

5.5.3 Parameter Estimation for Non-transmitting Antennas

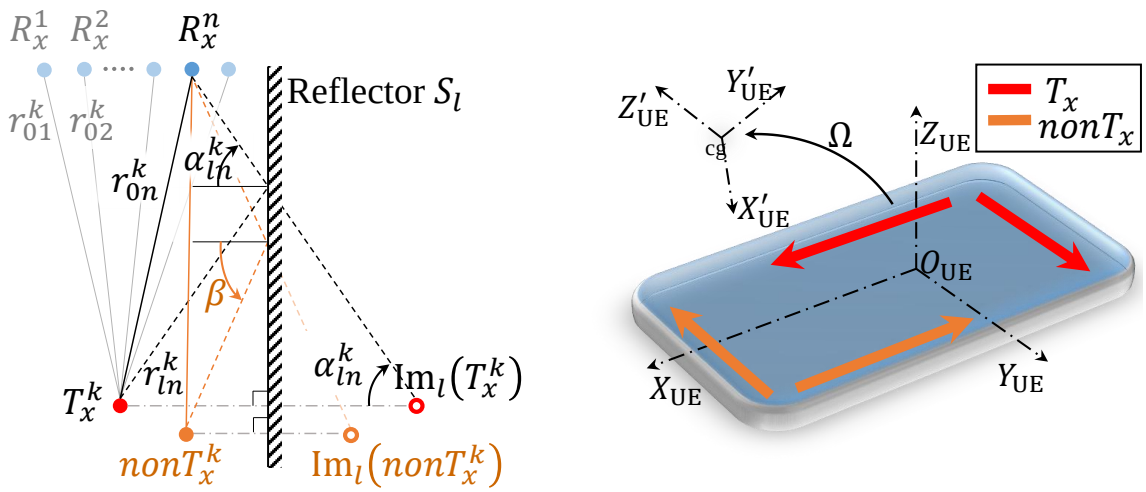

(a) (b)

Figure 5.9: (a) Derivation of the reflection plane from a transmitting antenna location and its image location. (b) Mobility of UE, its antennas' orientation and location.

As illustrated in Figure 5.9 (b), it is assumed that at least two of the m transmitting antennas are not parallel. During the CE procedure, ARDI can obtain the coordinates and orientations of the m transmitting antennas using the method introduced in Section 5.3, from which the orientation of the UE Ω can be estimated using the steps derived in Section 5.4. Suppose the layout the antennas in UE is a priori knowledge based on the UE design, both the positions and orientations of the non-transmitting antennas can then be calculated based on their relative positions/orientations to the transmitting antennas.

Inference of r_{ln}^k: For the LoS path, r_{ln}^k can be easily calculated based on the calculated locations of non-transmitting antennas described in Section 5.4.1. For the NLoS path, suppose $nonT_x^k$ represents the location for a non-transmitting antenna, as illustrated in Figure 5.9 (a). Based on the reflecting plane S_l, the image of $nonT_x^k$, denoted by $\mathrm{Im}_l(nonT_x^k)$, can be calculated since the location of $nonT_x^k$ is known. Then r_{ln}^k can be obtained by calculating the distance from the image to the receiving antenna, and the incident angle α_{ln}^k can also be obtained.

Inference of μ_{ln}^k: Once r_{ln}^k and the orientations of the non-transmitting antennas have been found, μ_{ln}^k for non-transmitting antennas can be inferred since

$$\mu_{ln}^k = \frac{j\eta}{4\pi r_{ln}^k} \boldsymbol{q}(\theta^{rx}) \cdot \boldsymbol{p}(\theta^{tx}).$$

Inference of D_{ln}^k: To infer the Doppler effects, ARDI needs to obtain at least two measurements of the location and orientation of the UE. Using these measurements, it calculates the speed and the angular velocity as follows:

$$\boldsymbol{v}_{cg} = \frac{\mathrm{UE}_{cg}(t_2) - \mathrm{UE}_{cg}(t_1)}{t_2 - t_1}, \ \dot{\Omega} = \frac{\Omega(t_2) - \Omega(t_1)}{t_2 - t_1},$$

where t_1 and t_2 are moments when the location and orientation measurements have been obtained. Consequently, speeds of antennas are inferred as $\boldsymbol{v}^k = \boldsymbol{v}_{cg} + \dot{\Omega} T_x^k$, and Doppler shifts are calculated according to (5.42).

After the inference of multipath propagation parameters $\{\mu_{ln}^k, r_{ln}^k, D_{ln}^k\}$ for non-transmitting antennas, ARDI reconstructs the DL channels using (5.44) for non-transmitting antennas. Figure 5.10 gives an example with 2 transmitting antennas and 2 non-transmitting antennas, where the red lines represent the measured channels and the black lines represent the reconstructed channels. For the uplink transmission, the full radio resource is equally allocated to the two transmitting antennas. For the DL channel inference, each antenna occupies the full radio resource.

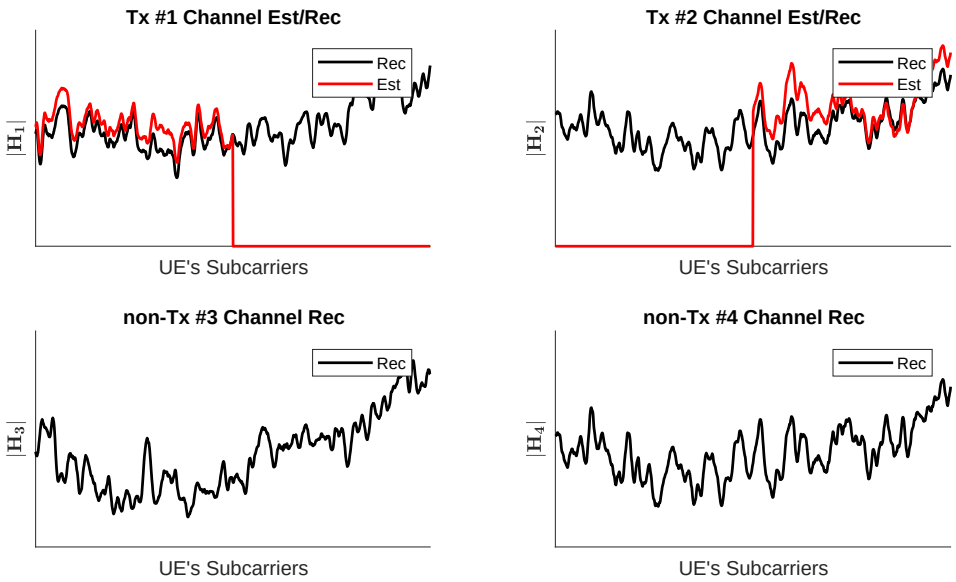

Figure 5.10: Example with estimated and inferred channels for a user equipment with four antennas two of them are transmitting in the LTE TDD transmission mode.

5.5.4 Feasibility for FDD and TDD Modes

It can be seen that the proposed scheme reconstructs the full DL channel based on the environmental parameters: propagation paths, mobility, location, and orientation of the UE's antennas. Based on the incomplete uplink channel measurements, ARDI infers these parameters and reconstructs the channels separately for all UE antennas. This means that ARDI creates a separate model of the environment for each antenna where the antenna is the only transmitting antenna. In this way, without interference from other antennas, each antenna can occupy the full radio resource and transmit signals from its estimated position with estimated orientation. This feature makes ARDI capable of inferring the DL channel in both TDD and FDD transmission modes.

5.6 Performance Evaluation

This section presents the results of a simulation-based evaluation of ARDI considering a realistic 3D movement of a user equipment.

5.6.1 Simulation Setup

As shown in Figure 5.11, the UE is kept in the human's right hand. A well-known eigenwalker model has been used to model a realistic movement of a human body (Troje, 2002). The yellow lines represent propagation paths. During a random walk, in addition to the ground reflection, six reflecting planes are simulated by randomly positioning and arbitrarily orienting them in the 3D space. However, only one reflector is depicted in the example since adding the other planes, and propagation paths can make the plot messy. The signals are propagated according to the SWP assumption and reflected based on the law of reflection described in Chapter 3 by taking into account the orientation of the transmitting antennas.

Signal Specification

A typical TDD LTE network with carrier frequency $\omega = 2.6$ GHz is simulated. The UE is a cellphone with four omnidirectional antennas, and only two of them can transmit. The LTE signals from two transmitting antennas occupy 100 resource blocks, with 12 subcarriers in each and 15 kHz separation between subcarriers (Sesia *et al.*, 2011). In total, 1200 subcarriers are equally shared by the two transmitting antennas. Additive Gaussian noise with zero mean value is applied at the BS side. The intensity of the

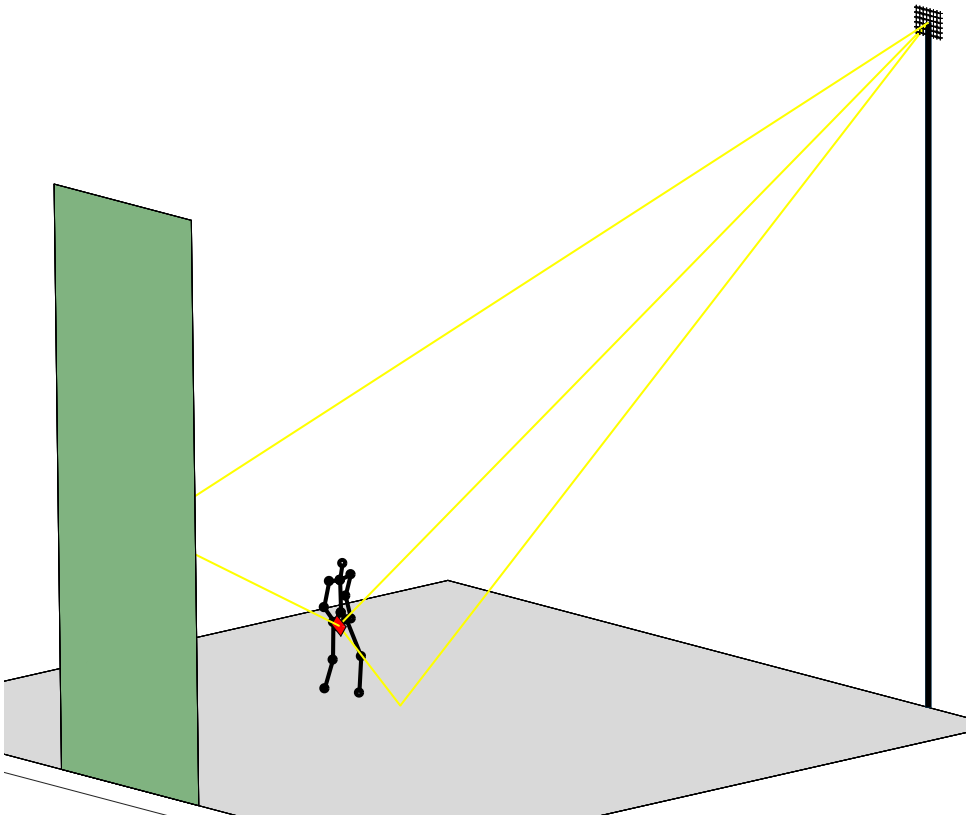

Figure 5.11: Simulation environment for signal propagation.

noise is defined by the SNR relative to the strength of the LoS signal. Even in the case where the LoS path is blocked, the noise intensity is calculated relative to the LoS signal as if it has been delivered to the BS.

Geometry Specification

As illustrated in Figure 5.11, the BS has a planar antenna array that consists of 256 antennas, 16 rows in horizontal and 16 columns in vertical directions. Antennas are half wavelength separated in both directions. Orientations of antennas are set in the way that each next antenna has alternated orientation {East, North, Up}. The location of the BS is fixed, and the height is 20 meters above the ground. The UE is modeled as a red rectangular polygon with 120×70 millimeters in length and width. Four antennas are located on the edges of the polygon in two parallel pairs, as shown in Figure 5.9 (b). The height of the human is 1.61 meters (probably Larisa Latynina, the second most decorated Olympian of all time (Wikipedia contributors, 2019a)). The distance between the BS and UE varies from 50 to 100 meters. The average moving speed is set to 5 kilometers per hour. Due to a realistic motion of the human's model and

3D motion of the UE, the speeds of antennas on the UE differ from each other. This creates different Doppler effects for different antennas. Note, the movement of the red polygon is a complex 3D movement that consists of a 3D rotation and 3D translation.

Physical Parameters of the Environment

The ground is assumed to be bricked. The reflectors are made from concrete. Relative permittivity and conductivity parameters of these materials are taken from the Material properties Table in (Raschkowski *et al.*, 2015). The air attenuation is considered as a free space attenuation.

In the same way as in Chapter 4, a standard Matlab function lsqnonlin is used to extract the propagation parameters from (5.45). Once the algorithm converges, the extracted results are fed to ARDI to analyze the accuracy of the antenna orientation reconstruction and channel inference. Two propagation scenarios are considered: *scenario 1* - a multipath propagation with LoS when the LoS path is observable; *scenario 2* - a multipath propagation without LoS when the LoS path and the path reflected from the ground are blocked.

5.6.2 Results on Antenna Orientation Reconstruction

Figure 5.12 plots the median and standard deviation of the antenna orientation reconstruction error measured in degrees under different setting of SNR. Each point is calculated based on the results of 500 iterations. It is well seen that the antenna orientation reconstruction error tends to converge to zero with the increase of SNR in both scenarios. The accuracy of the antenna orientation reconstruction is worse in *scenario 2*. This is an expected result caused by the blockage of the strong LoS path, which leads to a less accurate estimation of the propagation parameters. In addition, transformation matrix **Path** in Eqn. (5.23) accumulates less observation, which additionally degrades the overall reconstruction performance. However, such kind of accuracy is enough to achieve good performance on the DL channel reconstruction, which will be demonstrated in the following subsection. Figure 5.13 shows the cumulative distribution function (CDF) of the orientation reconstruction errors for the considered SNRs. The median estimation error is less than 2° even for *scenario 2*. This capability can be used in different types of applications such as the elimination of DL channel feedback in beamforming, human motion tracking, localization refining, etc.

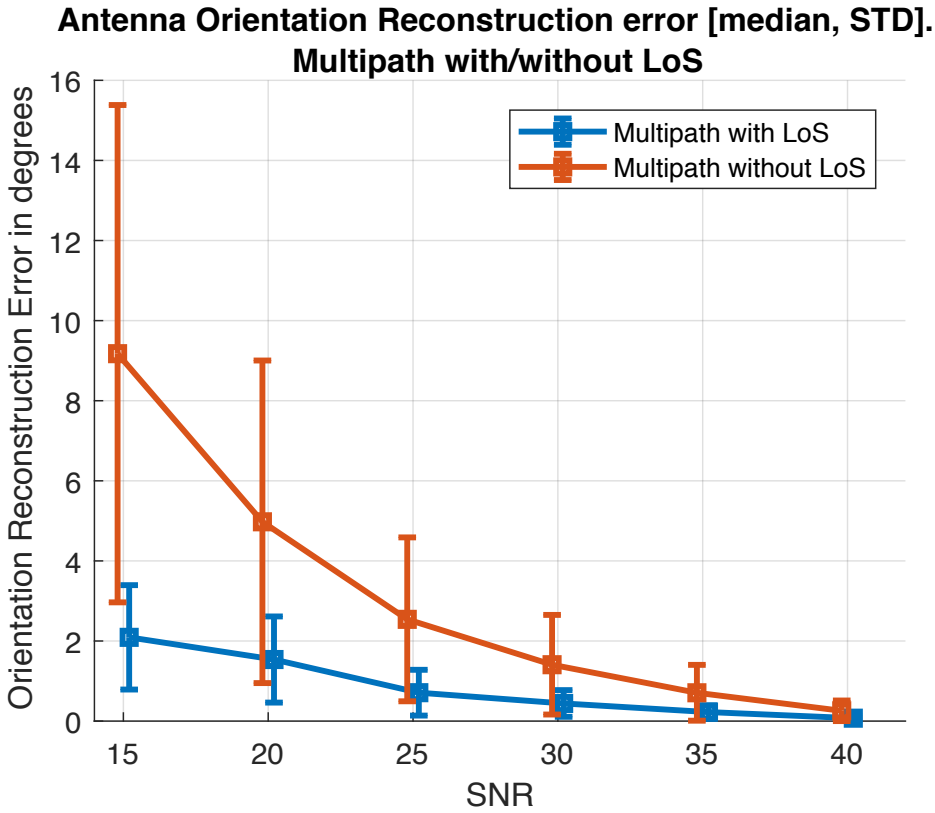

Figure 5.12: Accuracy of the antenna orientation estimation.

5.6.3 Results on Full Downlink Channel Reconstruction

In this section, the evaluation of ARDI performance in the DL channel reconstruction is analyzed. In the simulation, at first, the channels are measured separately for each pair of communicating antennas $\overline{\mathbf{H_n^k}} = (H_n^k(f_1), .., H_n^k(f_{N_s}))^T$ where $n \in [1, ..., 256]$, $k \in [1, ..., 4]$, $N_s = 1200$, and $H_n^k(f_i)$ is defined in Eqn. (5.43). Then, the measured channels for the two transmitting antennas $(\overline{\mathbf{H_n^1}}, \overline{\mathbf{H_n^2}})$ are cropped by providing each antenna with 600 subcarriers. As illustrated in Figure 5.10, the first antenna occupies the first 600 subcarriers, and the second occupies the rest part of the subcarriers. After the crop, ARDI extracts propagation parameters $\{\mu_{ln}^k, r_{ln}^k, D_{ln}^k\}$ from the cropped channels. Then, ARDI performs the antenna orientation reconstruction and DL channel inference for the non-transmitting antennas $(\mathbf{H_n^3}, \mathbf{H_n^4})$, which are further compared with the measured channels $(\overline{\mathbf{H_n^3}}, \overline{\mathbf{H_n^4}})$. To analyze the accuracy of the DL channel reconstruction, the ARDI's results are compared with an "old" approach in which the BS just uses the measured channels for the transmitting antennas as predictions for the corresponding parallel non-transmitting ones. In other words, the measured channels $\overline{\mathbf{H_n^1}}$ are used to predict channels for non-transmitting antenna #3, and $\overline{\mathbf{H_n^2}}$ is used to

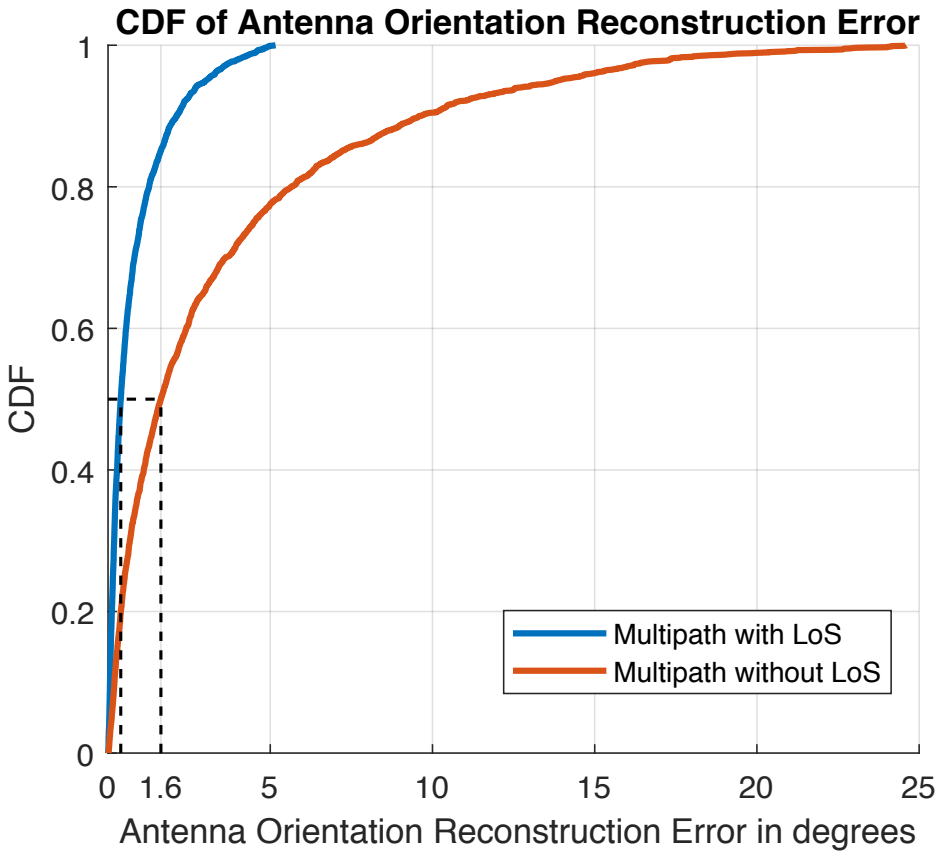

Figure 5.13: CDF of the antenna orientation estimation.

predict channels for non-transmitting antenna #4.

The aim is to analyze the difference between the reconstructed channel and the measured channel in terms of both amplitude and phase. However, the absolute difference between the measured and reconstructed channels is not representative since the absolute values of the channels for different distances may differ by the orders of magnitudes. The channel differences for locations that are far from the BS can be much smaller than the differences for locations that are close to the BS. Due to this, the following metric is proposed, which can be considered as a normalized difference between reconstructed and measured channels (Zhou and Giannakis, 2004):

$$\epsilon_n^k = \frac{\|\overline{\mathbf{H_n^k}} - \mathbf{H_n^k}\|}{\|\overline{\mathbf{H_n^k}}\|}, \quad n \in [1, .., 256], k \in [3, 4], \tag{5.47}$$

where $\overline{\mathbf{H_n^k}}$ is the measured channel and $\mathbf{H_n^k}$ is the reconstructed channel. It can be seen that the closer the reconstructed channel to the measured channel, the smaller the value of ϵ. This metric takes into account not only the correlation of the channels but also the similarity of amplitudes and complex phases of the channels. For example,

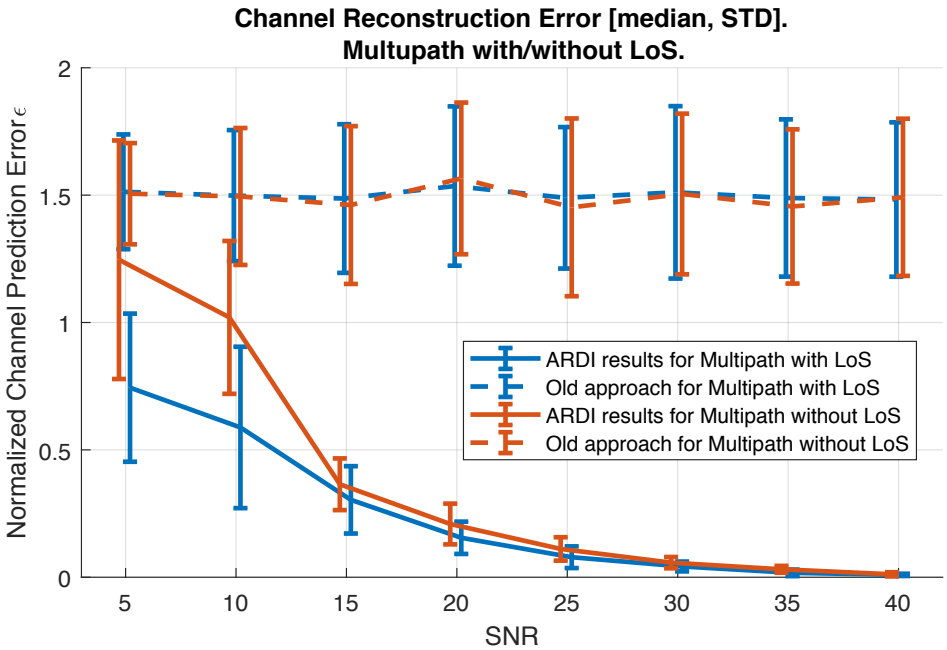

Figure 5.14: Accuracy of the DL channel reconstruction.

the channels may be well correlated with coefficient of correlation $\rho(\overline{\mathbf{H_n^k}}, \mathbf{H_n^k}) \approx \mathbf{1}$ while $\mathbf{H_n^k} = \beta\overline{\mathbf{H_n^k}}$ where β can be any complex number. It is also critical to make β close to one especially in a precoding procedure (Sesia *et al.*, 2011), which means the difference $\|\overline{\mathbf{H_n^k}} - \mathbf{H_n^k}\|$ has to be close to zero.

Let us consider the case where the amplitudes of $\overline{\mathbf{H_n^k}}$ and $\mathbf{H_n^k}$ are quite similar, which is possible when the localization is performed accurately. Let $\mathbf{H_n^k} = \Phi\overline{\mathbf{H_n^k}}$ where Φ is a unitary matrix in the vector space $\mathbb{C}^{N_s}$. The metric Eqn. (5.47) can be re-written as

$$\epsilon_n^k = \frac{\|(I_{N_s} - \Phi)\overline{\mathbf{H_n^k}}\|}{\|\overline{\mathbf{H_n^k}}\|}, \quad n \in [1, .., 256], k \in [3, 4].$$

Since the amplitudes are similar, the difference on phases will dominate the reconstruction error. Hence, if $\Phi = I_{N_s}$, $\epsilon_n^k = 0$, which indicates that the channel is accurately reconstructed. If $\Phi = -I_{N_s}$, $\epsilon_n^k = 2$, which is the worst case. Consequently, if the amplitudes of the measured and the reconstructed channels are similar, $\epsilon_n^k \in [0, 2]$. Significantly different amplitudes indicate that the localization has been possibly performed with a big error. In this case, the difference in amplitude can dominate in the reconstruction error, and ϵ_n^k can be any positive value fenced from zero.

To examine the overall channel reconstruction performance, the DL channel reconstruction scheme has been executed 100 times under different settings on SNR. For each iteration, median and standard deviation values have been calculated for

$\{\epsilon_n^k\}$ $n \in [1, ..256]$, $k \in [3, 4]$, and then all the obtained medians and standard deviations have been averaged over 100 iterations. Figure 5.14 shows the average medians and standard deviations under different settings on SNR. It can be seen that the reconstructed channels converge to the measured channels in both scenarios with the increase of SNR. One observation from this figure is that the "old" approach does not give good channel prediction for any SNR. Note, if the metric is far above zero, the reconstructed channel is less likely related to the real channel. Another interesting observation can be seen from the standard deviation. For lower SNRs, ARDI has a larger standard deviation than the "old" approach. This is because, for lower SNRs, ARDI reconstructs the DL channel inaccurately because of the large errors in the estimating the propagation parameters, orientations and locations of antennas. Instead of reconstructing the channel near the UE, ARDI reconstructs the channel for a distant place from the UE. In such kind of situations, the value of ϵ_n^k can significantly increase and can be higher than 2. However, in most cases, ARDI can still correctly reconstruct DL channel, and this is why the median is lower than that in the "old" approach. As expected, the performance of the DL channel reconstruction is slightly weaker in *Scenario 2*. For higher SNRs starting from 15 dB, ARDI performs similarly in both scenarios. Based on the obtained results it can be concluded that ARDI is capable of reconstructing the full DL channel with a reasonable accuracy for SNRs higher than 15 dB. This revolutionary ability of ARDI can become very helpful in the reconstruction of the full massive MIMO channel from incomplete channel measurements.

5.7 Conclusion

In this chapter, a smart scheme ARDI is introduced, the scheme is capable of reconstructing the full downlink channel in massive MIMO systems from incomplete UL channel measurements in both FDD and TDD communication modes. Consequently, ARDI enables the increase of a massive MIMO channel capacity without further growth of the number of transmitting antennas. The results of this work can have implication for other types of wireless communication systems such as WiFi and mmWave networks since the same physical principles are used in all of them. Further development of this research lays in the extension of the antenna orientation reconstruction method towards realistic antenna models and experimental validation.

Chapter 6

Conclusion and Future Work

6.1 Conclusion

This thesis has discussed challenging issues regarding radio channel modeling, user localization, and channel reconstruction for non-transmitting antennas. New practical solutions for these issues are essential for the further development of both existing and next-generation networks. As discussed, one of the main inhibitory factors for the development of modern networks is the increasing complexity of the CE procedure. Due to the formation of the procedure under the stochastic channel paradigm, CE also gives an outdated state of the channel, which is a critical drawback especially for the next-generation networks. That is why this thesis focuses on designing channel acquisition schemes that rely not only on the channel response but also the spatial information about the propagation environment. Note, in this thesis, the concept of the propagation environment goes a little further than just the surrounding environment. It also incorporates the location, orientation, and mobility information of the communicating BSs and UEs.

Similar to the transition between the time and frequency domains, the main idea of the thesis is to enable the transition between the channel and environment domains. As illustrated in Figure 6.1, the transition from the channel domain to the environmental domain is performed using the observed channel; the required manipulations with the spatial information about the propagation environment are made in the environment domain; the transition back to the channel domain is then performed by reconstructing the resulting channel. Such an approach in channel processing obviates the reception of the channel response, which is time consuming, and reconstructs channels even for non-transmitting antennas. Hence, the transition between the channel and environment

domains becomes helpful in developing solutions that mitigate the CE challenges in both existing and next-generation networks: excessive energy consumption at the UE side; an ineffective mechanism of channel feedback; the outdated state of the channel; and inability to provide channel state information for non-transmitting antennas.

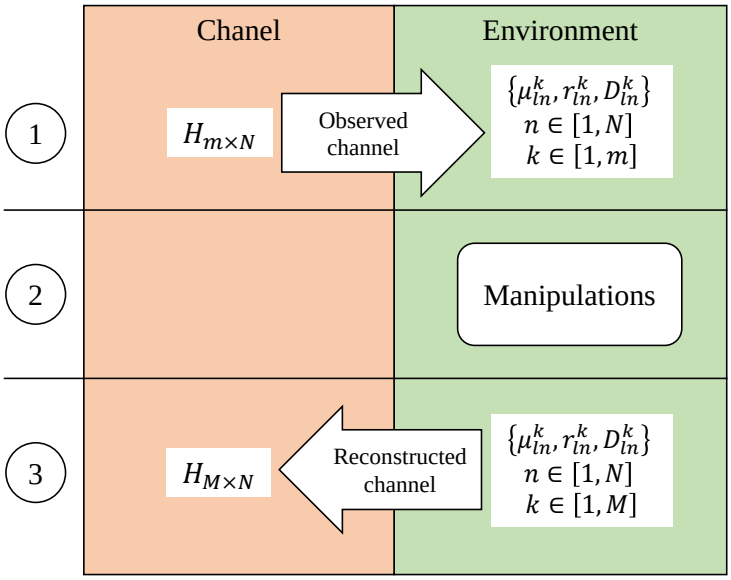

Figure 6.1: Channel and environment domains. Notations are taken from Chapter 5.

However, to enable a correct transition back and forth, a spatially consistent channel model has to be designed. Thus, Chapter 3 presents the methodology for creating a spatially consistent channel model for Massive MIMO systems. The main contributions of this research are the incorporation of the SWP model in the channel model and the complete derivation of the reflection of the wireless signal from arbitrarily inclined surfaces. The channel model designed correctly links the propagation environment with the observed channels. Further, to realize the transition from the channel domain to the environment domain, a novel localization solution has been designed. Chapter 4 describes in detail the user localization solution in massive MIMO networks. The main contributions of this piece of work are user localization based on only UL signals including LTE RACH signals under the SWP assumption, phase noise elimination, and carrying out proof-of-concept localization experiments on the Otago University massive MIMO testbed. The designed solution is capable of accurately localizing UEs in both single-path and multipath environments.

To realize the transition back from the environment domain to channel domain, a novel solution in channel reconstruction for non-transmitting antennas has been developed. Chapter 5 describes in detail the channel reconstruction scheme. The main

challenge in designing the solution was to obtain the orientation information of non-transmitting antennas. Knowledge about orientation becomes essential, especially in the inference of spatial characteristics of the non-transmitting antennas. This inference can be considered as "manipulations" in the environment domain. Thus, the central contribution of this study is the orientation reconstruction of a single transmitting antenna in both single-path and multipath propagation environments. The locations and orientations of non-transmitting antennas can be inferred from the estimated locations and orientations of transmitting antennas using the known layout design of the UE. Another contribution of this work is in the advancement of the channel modeling approaches described in Chapter 3 by incorporating a mechanism for signal polarization change that is consistent with any 3D movement. Once locations and orientations of all antennas are known, the propagation paths can be inferred, which means that channels for non-transmitting antennas can also be reconstructed.

6.2 Limitations

Due to the lack of a full-size testbed, all the results on channel simulation have been evaluated theoretically and compared with the available publications in terms of logical correctness, and hence there might be incorrectness in describing the real channel effects. Although the proof-of-concept localization experiments have been conducted on the Otago University massive MIMO testbed, this was a small testbed that consists of only two radios. All the time alignment procedures have been done offline. Consequently, some essential effects of simultaneous reception might have been unobserved. Also, due to the lack of a full-size testbed, it was impossible to examine which hardware impairment has a dominant negative effect in localization performance. Thus, only phase noise has been considered, since the effect of a nonideal synchronization is observable even for the Otago testbed. This limitation can be addressed by accessing full-sized testbeds in larger research laboratories such as Lund, Bristol, or Rice Universities, and hence this topic falls to future studies.

The antenna orientation reconstruction was developed by considering the Hertzian dipole antenna model. Although the model has non-zero size and orientation, that is, the antenna cannot be considered as a point source, this is still an idealized model. However, this solution can become helpful in developing solutions for other antenna models. Addressing this limitation transforms into an even larger research question that may have fundamental impacts on future wireless technologies.

6.3 Future Work

Further development of the channel modeling project lies in the experimental validation of the proposed approaches and enhancement of the variety of simulation scenarios by considering other areas for which accurate geometrical representations are available. This will give an excellent platform for collecting channel statistics that can be used, for example, in finding optimal positions for BSs. Simultaneously with the incorporation of new scenarios, it will be interesting to analyze the performance of the localization solution in different environments. The main direction of future work for the localization solution is to conduct field experiments with a full-sized massive MIMO prototype. For this purpose, it is worth look for a postdoc opportunity in the leading research laboratories such as Lund, Bristol, or Rice Universities. Another interesting future direction for the localization project is to implement Machine Learning approaches in the nonlinear data-fitting optimization problem to increase the localization accuracy and robustness.

The future development of the antenna reconstruction and channel reconstruction – like the localization – lies in extensive experimental validation. The first step of the experiments for validating the correctness of the antenna orientation reconstruction can be started by conducting proof-of-concept tests using the Otago testbed, and then extending it to channel reconstruction validation experiments.

6.4 Final Words

It has been an interesting dive into the massive MIMO topic. Each step opened far more new questions than I was able to cover. It should be a standard situation in science – each tiny step sheds light on a broader area. I hope that the produced contributions will find their applications in the real world.

Bibliography

Abbott, B. P. *et al.* (2016). Observation of Gravitational Waves from a Binary Black Hole Merger. *Phys. Rev. Lett.*, *116*, 061102.

Abu-Rgheff, M. (2007). *Introduction to CDMA Wireless Communications*. Elsevier Science.

Adeogun, R. O., Teal, P. D., and Dmochowski, P. A. (2015). Extrapolation of MIMO Mobile-to-Mobile Wireless Channels Using Parametric-Model-Based Prediction. *IEEE Transactions on Vehicular Technology*, *64*(10), 4487–4498.

Adib, F., Mao, H., Kabelac, Z., Katabi, D., and Miller, R. C. (2015). Smart Homes That Monitor Breathing and Heart Rate. In *Proceedings of the 33rd Annual ACM Conference on Human Factors in Computing Systems*, CHI '15, New York, NY, USA, 837–846. ACM.

Afraimovich, E. L., Chernukhov, V. V., Kobzar, V. A., and Palamartchouk, K. S. (1999). Determining polarization parameters and angles of arrival of HF radio signals using three mutually orthogonal antennas. *Radio Science*, *34*(5), 1217–1225.

Agee, W. S. and Turner, R. H. (1972). Optimal estimation of measurement bias. Technical report, National Range Operations Directorate White Sands Missile Range Nm Analysis and Computation Div.

Alard, M. and Lassalle, R. (1987). Principles of Modulation and Channel Coding for Digital Broadcasting for Mobile Receivers. *Eur Broadcast Union Rev*, *224*, 47–68.

Aleksiejunas, R. (2016). MIMO Channel Reconstruction from Lower Dimensional Multiple Antenna Measurements. *CoRR*, *abs/1612.02925*, 1–16.

Alsharif, M. H., Kim, J., and Kim, J. H. (2017). Green and Sustainable Cellular Base Stations: An Overview and Future Research Directions. *Energies*, *10*(5), 1–27.

Ament, W. S. (1953). Toward a Theory of Reflection by a Rough Surface. *Proc. IRE*, *41*(1), 142–146.

Bancroft, S. (1985). An Algebraic Solution of the GPS Equations. *IEEE Transactions on Aerospace and Electronic Systems*, *AES-21*(1), 56–59.

Björnson, E., Hoydis, J., Kountouris, M., and Debbah, M. (2014). Massive MIMO Systems With Non-Ideal Hardware: Energy Efficiency, Estimation, and Capacity Limits. *IEEE Transactions on Information Theory*, *60*(11), 7112–7139.

Björnson, E., Hoydis, J., and Sanguinetti, L. (2017). *Massive MIMO Networks:Spectral, Energy, and Hardware Efficiency.* Now Foundations and Trends.

Björnson, E., Larsson, E. G., and Debbah, M. (2016). Massive MIMO for Maximal Spectral Efficiency: How Many Users and Pilots Should Be Allocated? *IEEE Transactions on Wireless Communications*, *15*(2), 1293–1308.

Björnson, E., Larsson, E. G., and Marzetta, T. L. (2016). Massive MIMO: ten myths and one critical question. *IEEE Communications Magazine*, *54*(2), 114–123.

Boban, M., Barros, J., and Tonguz, O. K. (2014). Geometry-Based Vehicle-to-Vehicle Channel Modeling for Large-Scale Simulation. *IEEE Transactions on Vehicular Technology*, *63*(9), 4146–4164.

Brewer, J. (1978). Kronecker products and matrix calculus in system theory. *IEEE Transactions on Circuits and Systems*, *25*(9), 772–781.

Cao, W. and Wang, W. (2004). A frequency-domain channel prediction algorithm in wideband wireless communication systems. In *2004 IEEE 15th International Symposium on Personal, Indoor and Mobile Radio Communications (IEEE Cat. No.04TH8754)*, Volume 4, 2402–2405 Vol.4.

Chen, T., Zakharov, Y. V., and Liu, C. (2011). Low-Complexity Channel-Estimate Based Adaptive Linear Equalizer. *IEEE Signal Processing Letters*, *18*(7), 427–430.

Cherian, S. S. and Rudrapatna, A. N. (2013). LTE location technologies and delivery solutions. *Bell Labs Technical Journal*, *18*(2), 175–194.

Chizhik, D., Foschini, G. J., and Valenzuela, R. A. (2000). Capacities of multi-element transmit and receive antennas: Correlations and keyholes. *Electronics Letters*, *36*(13), 1099–1100.

Cho, Y. S., Kim, J., Yang, W. Y., and Kang, C. G. (2010). *MIMO-OFDM Wireless Communications with MATLAB*. Wiley Publishing.

Chu, D. (1972). Polyphase codes with good periodic correlation properties (Corresp.). *IEEE Transactions on Information Theory*, *18*(4), 531–532.

Cisco (2018). Cisco Visual Networking Index: Forecast and Trends, 2017–2022. `https://www.cisco.com/c/en/us/solutions/collateral/service-provider/visual-networking-index-vni/white-paper-c11-741490.pdf`. [Online; accessed 26-Nov-2018].

DOCOMO, N. (2018). Mitsubishi Electric and NTT DOCOMO Achieve World's First 27Gbps Throughput in 5G Outdoor Trials. `https://www.nttdocomo.co.jp/english/info/media_center/pr/2018/1122_00.html`. [Online; accessed 22-November-2018].

Dong, L., Xu, G., and Ling, H. (2001). Prediction of fast fading mobile radio channels in wideband communication systems. In *GLOBECOM'01. IEEE Global Telecommunications Conference (Cat. No.01CH37270)*, Volume 6, 3287–3291 vol.6.

Duel-Hallen, A. (2007). Fading Channel Prediction for Mobile Radio Adaptive Transmission Systems. *Proceedings of the IEEE*, *95*(12), 2299–2313.

Duel-Hallen, A., Hu, S., and Hallen, H. (2000). Long-range prediction of fading signals. *IEEE Signal Processing Magazine*, *17*(3), 62–75.

Emerson, D. T. (1997). The work of Jagadis Chandra Bose: 100 years of millimeter-wave research. *IEEE Transactions on Microwave Theory and Techniques*, *45*(12), 2267–2273.

Ericsson (2016). 5G radio access. `https://www.ericsson.com/assets/local/publications/white-papers/wp-5g.pdf`. [Online; accessed 2016].

Ericsson (2017). SmarTone, Ericsson trial FDD Massive MIMO. `https://www.ericsson.com/en/press-releases/2017/10/smartone-ericsson-trial-fdd-massive-mimo`. [Online; accessed 30-Oct-2017].

Ericsson (2018). Massive MIMO increasing capacity and spectral efficiency. `https://www.ericsson.com/en/news/2018/1/massive-mimo-highlight`. [Online; accessed 26-January-2018].

ETSI (2011). ETSI TS 136 104 V10.2.0. Standard, European Telecommunications Standards Institute, 650 Route des Lucioles,F-06921 Sophia Antipolis Cedex - FRANCE.

Ettus (2019). Ettus Research - The leader in Software Defined Radio. `https://www.ettus.com/`. [Online; accessed 14-January-2019].

Facebook (2016). Introducing Facebook's new terrestrial connectivity systems — Terragraph and Project ARIES. `https://code.fb.com/connectivity/introducing-facebook-s-new-terrestrial-connectivity-systems-terragraph-and-project-aries/`. [Online; accessed 13-April-2016].

Fedorov, A., Lyashev, V., and Rapoport, L. (2015). Fast algorithm of LTE RACH detection based on sparse fourier transform. In *2015 Third International Conference on Digital Information, Networking, and Wireless Communications (DINWC)*, 77–82.

Fedorov, A., Zhang, H., and Chen, Y. (2017). Geometry-based modeling and simulation of 3D multipath propagation channel with realistic spatial characteristics. In *2017 IEEE International Conference on Communications (ICC)*, 1–6.

Fedorov, A., Zhang, H., and Chen, Y. (2018). User Localization Using Random Access Channel Signals in LTE Networks with Massive MIMO. In *2018 27th International Conference on Computer Communication and Networks (ICCCN)*, 1–9.

Fedorov, A., Zhang, H., Sidorenko, G., and Yang, B. (2019). Full Downlink Channel Reconstruction using Incomplete Uplink Channel Measurements in Massive MIMO networks. In *IFIP Networking 2019 Conference*, 1–9.

Fleury, B. H., Jourdan, P., and Stucki, A. (2002). High-resolution channel parameter estimation for MIMO applications using the SAGE algorithm. In *2002 International Zurich Seminar on Broadband Communications Access - Transmission - Networking (Cat. No.02TH8599)*, 30–30.

Fleury, B. H., Tschudin, M., Heddergott, R., Dahlhaus, D., and Pedersen, K. I. (1999). Channel parameter estimation in mobile radio environments using the SAGE algorithm. *IEEE Journal on Selected Areas in Communications*, *17*(3), 434–450.

Flordelis, J., Gao, X., Dahman, G., Rusek, F., Edfors, O., and Tufvesson, F. (2015). Spatial separation of closely-spaced users in measured massive multi-user MIMO

channels. In *2015 IEEE International Conference on Communications (ICC)*, 1441–1446.

Flordelis, J., Hu, S., Rusek, F., Edfors, O., Dahman, G., Gao, X., and Tufvesson, F. (2016). Exploiting antenna correlation in measured massive MIMO channels. In *2016 IEEE 27th Annual International Symposium on Personal, Indoor, and Mobile Radio Communications (PIMRC)*, 1–6.

Flordelis, J., Rusek, F., Tufvesson, F., Larsson, E. G., and Edfors, O. (2018). Massive MIMO Performance—TDD Versus FDD: What Do Measurements Say? *IEEE Transactions on Wireless Communications*, *17*(4), 2247–2261.

Fodor, G., Rajatheva, N., Zirwas, W., Thiele, L., Kurras, M., Guo, K., Tolli, A., Sorensen, J. H., and d. Carvalho, E. (2017). An Overview of Massive MIMO Technology Components in METIS. *IEEE Communications Magazine*, *55*(6), 155–161.

Foschini, G. and Gans, M. (1998). On Limits of Wireless Communications in a Fading Environment when Using Multiple Antennas. *Wireless Personal Communications*, *6*(3), 311–335.

Gao, X., Edfors, O., Rusek, F., and Tufvesson, F. (2015). Massive MIMO Performance Evaluation Based on Measured Propagation Data. *IEEE Transactions on Wireless Communications*, *14*(7), 3899–3911.

Gel'fand, I. M. (1989). *Lectures on linear algebra*. Courier Corporation.

Gibbons, A. (2009). A New Kind of Ancestor: Ardipithecus Unveiled. *Science*, *326*(5949), 36–40.

Gkizeli, M. and Karystinos, G. N. (2014). Maximum-SNR Antenna Selection Among a Large Number of Transmit Antennas. *IEEE Journal of Selected Topics in Signal Processing*, *8*(5), 891–901.

Golovan, A. A. and Cepe, A. (2016). Determination of trajectory parameters for a small satellite using raw satellite measurements. *Moscow University Mechanics Bulletin*, *71*(1), 19–22.

Google (2005). Google Maps is a web mapping service developed by Google. `www.google.com/maps`. [Online; accessed 8-Feb-2004].

Han, Y., Hsu, T.-H., Wen, C.-K., Wong, K.-K., and Jin, S. (2018). Efficient Downlink Channel Reconstruction for FDD Multi-Antenna Systems. *ArXiv e-prints*, *0*, 1–23.

Han, Y., Ni, J., and Du, G. (2010). The potential approaches to achieve channel reciprocity in FDD system with frequency correction algorithms. In *2010 5th International ICST Conference on Communications and Networking in China*, 1–5.

Hardell, L. (2017). World Health Organization, radiofrequency radiation and health - a hard nut to crack (Review). *International Journal of Oncology*, *51*(2), 405–413. Exported from https://app.dimensions.ai on 2018/12/22.

Harris, P., Hasan, W. B., Malkowsky, S., Vieira, J., Zhang, S., Beach, M., Liu, L., Mellios, E., Nix, A., Armour, S., Doufexi, A., Nieman, K., and Kundargi, N. (2016). Serving 22 Users in Real-Time with a 128-Antenna Massive MIMO Testbed. In *2016 IEEE International Workshop on Signal Processing Systems (SiPS)*, 266–272.

Harris, P., Malkowsky, S., Vieira, J., Bengtsson, E., Tufvesson, F., Hasan, W. B., Liu, L., Beach, M., Armour, S., and Edfors, O. (2017). Performance Characterization of a Real-Time Massive MIMO System With LOS Mobile Channels. *IEEE Journal on Selected Areas in Communications*, *35*(6), 1244–1253.

Hassanieh, H., Adib, F., Katabi, D., and Indyk, P. (2012). Faster GPS via the Sparse Fourier Transform. In *Proceedings of the 18th Annual International Conference on Mobile Computing and Networking*, Mobicom '12, New York, NY, USA, 353–364. ACM.

Heath, R. W., González-Prelcic, N., Rangan, S., Roh, W., and Sayeed, A. M. (2016). An Overview of Signal Processing Techniques for Millimeter Wave MIMO Systems. *IEEE Journal of Selected Topics in Signal Processing*, *10*(3), 436–453.

Heino, P., Meinilä, J., Kyösti, P., Hentila, L., Jämsä, T., Suikkanen, E., Kunnari, E., and Narandzic, M. (2010). CP5-026 WINNER+ D5.3 v1.0 WINNER+ Final Channel Models. Tech. rep., University of Oulu.

Henderson, H. V. and Searle, S. R. (1981). The vec-permutation matrix, the vec operator and Kronecker products: a review. *Linear and Multilinear Algebra*, *9*(4), 271–288.

Hertz, H. and Jones, D. (1893). *Electric Waves: Being Researches on the Propagation of Electric Action with Finite Velocity Through Space*. Macmillan.

Householder, A. S. (1958). Unitary Triangularization of a Nonsymmetric Matrix. *J. ACM*, *5*(4), 339–342.

Hoydis, J., ten Brink, S., and Debbah, M. (2013). Massive MIMO in the UL/DL of Cellular Networks: How Many Antennas Do We Need? *IEEE Journal on Selected Areas in Communications*, *31*(2), 160–171.

Huawei (2017). Massive MIMO is the future of wireless networks. `https://www.huawei.com/en/about-huawei/publications/winwin-magazine/28/massive-mimo-2016`. [Online; accessed 21-June-2017].

Huawei (2018). Huawei deploys world's first commercial FDD Massive MIMO in Philippines. `http://www.telecomreviewasia.com/index.php/news/network-news/964-huawei-deploys-world-s-first-commercial-fdd-massive-mimo-in-philippines`. [Online; accessed 12-Mar-2017].

Hugl, K., Kalliola, K., and Laurila, J. (2002). Spatial Reciprocity of Uplink and Downlink Radio Channels in FDD Systems. In *COST / European Cooperation in Science and Technology*.

ICNIRP (2018). Guidelines for limiting exposure to time-varying electric, magnetic and electromagnetic fields (100 kHz to 300 GHz). `https://www.icnirp.org/cms/upload/consultation_upload/ICNIRP_RF_Guidelines_PCD_2018_07_11.pdf`. [Online; accessed 11-July-2018].

Imtiaz, S., Dahman, G. S., Rusek, F., and Tufvesson, F. (2014). On the directional reciprocity of uplink and downlink channels in Frequency Division Duplex systems. In *2014 IEEE 25th Annual International Symposium on Personal, Indoor, and Mobile Radio Communication (PIMRC)*, 172–176.

Instruments, N. (2018). Introduction to the NI mmWave Transceiver System Hardware. `http://www.ni.com/white-paper/53095/en/`. [Online; accessed 09-Jul-2018].

ITU (2009). Guidelines for evaluation of radio interface technologies for IMT-Advanced. Technical report, International Telecommunication Union.

Jaeckel, S., Raschkowski, L., Börner, K., and Thiele, L. (2014). QuaDGa: A 3-D Multi-Cell Channel Model With Time Evolution for Enabling Virtual Field Trials. *IEEE Transactions on Antennas and Propagation*, *62*(6), 3242–3256.

Ji, H., Kim, Y., Lee, J., Onggosanusi, E., Nam, Y., Zhang, J., Lee, B., and Shim, B. (2017). Overview of Full-Dimension MIMO in LTE-Advanced Pro. *IEEE Communications Magazine*, *55*(2), 176–184.

Jiang, Z., Molisch, A. F., Caire, G., and Niu, Z. (2015). Achievable Rates of FDD Massive MIMO Systems With Spatial Channel Correlation. *IEEE Transactions on Wireless Communications*, *14*(5), 2868–2882.

Jose, J., Ashikhmin, A., Marzetta, T. L., and Vishwanath, S. (2011). Pilot Contamination and Precoding in Multi-Cell TDD Systems. *IEEE Transactions on Wireless Communications*, *10*(8), 2640–2651.

Joung, J. and Sun, S. (2014). SCF: Sparse channel-state-information feedback using Karhunen-Loève transform. In *2014 IEEE Globecom Workshops (GC Wkshps)*, 314–319.

Kashyap, S., Mollén, C., Björnson, E., and Larsson, E. G. (2017). Performance analysis of (TDD) massive MIMO with Kalman channel prediction. In *2017 IEEE International Conference on Acoustics, Speech and Signal Processing (ICASSP)*, 3554–3558.

Keysight (2016). Examining the Challenges in Implementing and Testing Massive MIMO for 5G. `http://literature.cdn.keysight.com/litweb/pdf/5992-1448EN.pdf`. [Online; accessed 24-May-2016].

Kihei, B., Copeland, J. A., and Chang, Y. (2017). Cepstral Analysis for Classifying Car Collisions in LOS/NLOS Vehicle-to-Vehicle Networks. In *GLOBECOM 2017 - 2017 IEEE Global Communications Conference*, 1–6.

Kumar, S., Hamed, E., Katabi, D., and Erran Li, L. (2014). LTE Radio Analytics Made Easy and Accessible. *SIGCOMM Comput. Commun. Rev.*, *44*(4), 211–222.

Landron, O., Feuerstein, M., and Rappaport, T. (1996). A comparison of theoretical and empirical reflection coefficients for typical exterior wall surfaces in a mobile radio environment. *IEEE Transactions on Antennas and Propagation*, *44*(3), 341–351.

Larsson, E. G., Edfors, O., Tufvesson, F., and Marzetta, T. L. (2014). Massive MIMO for next generation wireless systems. *IEEE Communications Magazine*, *52*(2), 186–195.

Li, X., Batstone, K., Åstrom, K., Oskarsson, M., Gustafson, C., and Tufvesson, F. (2017). Robust phase-based positioning using massive MIMO with limited bandwidth. In *2017 IEEE 28th Annual International Symposium on Personal, Indoor, and Mobile Radio Communications (PIMRC)*, 1–7.

Liu, A., Lau, V., and Dai, W. (2016). Joint burst LASSO for sparse channel estimation in multi-user massive MIMO. In *2016 IEEE International Conference on Communications (ICC)*, 1–6.

Liu, L., Oestges, C., Poutanen, J., Haneda, K., Vainikainen, P., Quitin, F., Tufvesson, F., and Doncker, P. D. (2012). The COST 2100 MIMO channel model. *IEEE Wireless Communications*, *19*(6), 92–99.

Ljung, L. (1999). *System Identification: Theory for the User*. Prentice Hall information and system sciences series. Prentice Hall PTR.

Lorenz, R. G. and Boyd, S. P. (2005). Robust minimum variance beamforming. *IEEE Transactions on Signal Processing*, *53*(5), 1684–1696.

Love, D. J. and Heath, R. W. (2005). Limited feedback unitary precoding for spatial multiplexing systems. *IEEE Transactions on Information Theory*, *51*(8), 2967–2976.

Love, D. J., Heath, R. W., Lau, V. K. N., Gesbert, D., Rao, B. D., and Andrews, M. (2008). An overview of limited feedback in wireless communication systems. *IEEE Journal on Selected Areas in Communications*, *26*(8), 1341–1365.

Love, D. J., Heath, R. W., and Strohmer, T. (2003). Grassmannian beamforming for multiple-input multiple-output wireless systems. *IEEE Transactions on Information Theory*, *49*(10), 2735–2747.

Mahler, K., Keusgen, W., Tufvesson, F., Zemen, T., and Caire, G. (2015). Propagation of Multipath Components at an Urban Intersection. In *2015 IEEE 82nd Vehicular Technology Conference (VTC2015-Fall)*, 1–5.

Mai, H., Zakharov, Y. V., and Burr, A. G. (2007). Iterative Channel Estimation Based on B-splines for Fast Flat Fading Channels. *IEEE Transactions on Wireless Communications*, *6*(4), 1224–1229.

Malkowsky, S., Vieira, J., Liu, L., Harris, P., Nieman, K., Kundargi, N., Wong, I. C., Tufvesson, F., Öwall, V., and Edfors, O. (2017). The World's First Real-Time

Testbed for Massive MIMO: Design, Implementation, and Validation. *IEEE Access*, *5*, 9073–9088.

Marquardt, D. W. (1963). An algorithm for least-squares estimation of nonlinear parameters. *Journal of the society for Industrial and Applied Mathematics*, *11*(2), 431–441.

Marzetta, T. L. (2010). Noncooperative Cellular Wireless with Unlimited Numbers of Base Station Antennas. *IEEE Transactions on Wireless Communications*, *9*(11), 3590–3600.

Marzetta, T. L., Larsson, E. G., Yang, H., and Ngo, H. Q. (2016). *Fundamentals of Massive MIMO*. Cambridge University Press.

Mohammadi, A. and Ghannouchi, F. M. (2011). Single RF front-end MIMO transceivers. *IEEE Communications Magazine*, *49*(12), 104–109.

Molisch, A. F., Win, M. Z., and Winters, J. H. (2003). Reduced-complexity transmit/receive-diversity systems. *IEEE Transactions on Signal Processing*, *51*(11), 2729–2738.

Narandzic, M., Kaske, M., Schneider, C., Milojevic, M., Landmann, M., Sommerkorn, G., and Thoma, R. S. (2007). 3D-Antenna Array Model for IST-WINNER Channel Simulations. In *2007 IEEE 65th Vehicular Technology Conference - VTC2007-Spring*, 319–323.

Ngo, H. Q. and Larsson, E. G. (2017). No Downlink Pilots Are Needed in TDD Massive MIMO. *IEEE Transactions on Wireless Communications*, *16*(5), 2921–2935.

Ngo, H. Q., Larsson, E. G., and Marzetta, T. L. (2013). Energy and Spectral Efficiency of Very Large Multiuser MIMO Systems. *IEEE Transactions on Communications*, *61*(4), 1436–1449.

Noerpel, A. R., Krain, M. J., and Ranade, A. (1991). Measured scattered signals at 4 GHz confirm strong specular reflections off buildings. *Proc. IEEE International Conference on Communications (ICC)*, *1*, 473–477.

OpenStreetMaps (2004). OpenStreetMap is a map of the world, created by people like you and free to use under an open licence. `https://www.openstreetmap.org`. [Online; accessed 9-Aug-2004].

Orfanidis, S. J. (2014). *Electromagnetic Waves and Antennas*. Rutgers University New Brunswick, NJ.

Palleit, N. and Weber, T. (2009). Obtaining transmitter side channel state information in MIMO FDD systems. In *2009 IEEE 20th International Symposium on Personal, Indoor and Mobile Radio Communications*, 2439–2443.

Palleit, N. and Weber, T. (2010). Channel prediction in point-to-point MIMO-systems. In *2010 7th International Symposium on Wireless Communication Systems*, 91–95.

Prabhu, H., Rodrigues, J. N., Liu, L., and Edfors, O. (2017). 3.6 A 60pJ/b 300Mb/s 128x8 Massive MIMO precoder-detector in 28nm FD-SOI. In *2017 IEEE International Solid-State Circuits Conference (ISSCC)*, 60–61.

Qualcomm (2013). The 1000x Mobile Data Challenge. `https://www.qualcomm.com/media/documents/files/1000x-mobile-data-challenge.pdf`. [Online; accessed 01-Nov-2013].

Qualcomm (2018). Qualcomm unveils first mmWave 5G antennas for smartphones. `https://www.theverge.com/2018/7/23/17596746/qualcomm-mmwave-5g-antenna-smartphones-qtm052-networking-speeds-size`. [Online; accessed 23-Jul-2018].

Quitin, F., Oestges, C., Horlin, F., and Doncker, P. D. (2010). A Polarized Clustered Channel Model for Indoor Multiantenna Systems at 3.6 GHz. *IEEE Transactions on Vehicular Technology*, *59*(8), 3685–3693.

Raghavan, V., Heath, R. W., and Sayeed, A. M. (2007). Systematic Codebook Designs for Quantized Beamforming in Correlated MIMO Channels. *IEEE Journal on Selected Areas in Communications*, *25*(7), 1298–1310.

Rapoport, L. B., Tkachenko, M. Y., Mogil'nitskii, V. G., Khval'kov, A. A., and Pesterev, A. V. (2010). The GNSS/INS integrated system: Experimental results and its application in control of mobile robots. *Gyroscopy and Navigation*, *1*(2), 98–106.

Rappaport, T., Heath, R., Daniels, R., and Murdock, J. (2015). *Millimeter wave wireless communications*. Prentice Hall. Includes bibliographical references (pages 585-651) and index.

Rappaport, T. S., Sun, S., Mayzus, R., Zhao, H., Azar, Y., Wang, K., Wong, G. N., Schulz, J. K., Samimi, M., and Gutierrez, F. (2013). Millimeter Wave Mobile Communications for 5G Cellular: It Will Work! *IEEE Access*, *1*, 335–349.

Raschkowski, L., Kyösti, P., Kusume, K., and Jämsä, T. (2015). METIS Channel Models. Tech. rep., Ericsson AB.

Richter, A. (2005). *Estimation of Radio Channel Parameters: Models and Algorithms*. ISLE.

Roy, R. and Kailath, T. (1989). ESPRIT-estimation of signal parameters via rotational invariance techniques. *IEEE Transactions on Acoustics, Speech, and Signal Processing*, *37*(7), 984–995.

Rusek, F., Persson, D., Lau, B. K., Larsson, E. G., Marzetta, T. L., Edfors, O., and Tufvesson, F. (2013). Scaling Up MIMO: Opportunities and Challenges with Very Large Arrays. *IEEE Signal Processing Magazine*, *30*(1), 40–60.

Salmi, J., Richter, A., and Koivunen, V. (2009). Detection and Tracking of MIMO Propagation Path Parameters Using State-Space Approach. *IEEE Transactions on Signal Processing*, *57*(4), 1538–1550.

Samsung (2017). Samsung conducting Massive MIMO demo with Sprint at MWCA. `https://www.fiercewireless.com/wireless/samsung-conducting-massive-mimo-demo-sprint-at-mwca`. [Online; accessed 11-Sep-2017].

Samsung (2018). Specifications | Samsung Galaxy Note9 – The Official Samsung Galaxy Site. `https://www.samsung.com/global/galaxy/galaxy-note9/specs/`. [Online; accessed 15-Jan-2019].

Schmidt, R. (1986). Multiple emitter location and signal parameter estimation. *IEEE Transactions on Antennas and Propagation*, *34*(3), 276–280.

Schulz, B. (2015). White paper: LTE Transmission Modes and Beamforming. Technical report, Rohde-Schwarz.

Sesia, S., Toufik, I., and Baker, M. (2011). *LTE - The UMTS Long Term Evolution: From Theory to Practice*. Chichester: John Wiley & Sons Ltd.

Shahmansoori, A., Garcia, G. E., Destino, G., Seco-Granados, G., and Wymeersch, H. (2018). Position and Orientation Estimation Through Millimeter-Wave MIMO in 5G Systems. *IEEE Transactions on Wireless Communications*, *17*(3), 1822–1835.

Shamai, S. and Wyner, A. D. (1997a). Information-theoretic considerations for symmetric, cellular, multiple-access fading channels. I. *IEEE Transactions on Information Theory*, *43*(6), 1877–1894.

Shamai, S. and Wyner, A. D. (1997b). Information-theoretic considerations for symmetric, cellular, multiple-access fading channels. II. *IEEE Transactions on Information Theory*, *43*(6), 1895–1911.

Shannon, C. E. (1948). A mathematical theory of communication. *The Bell System Technical Journal*, *27*(3), 379–423.

Shepard, C., Yu, H., Anand, N., Li, E., Marzetta, T., Yang, R., and Zhong, L. (2012). Argos: Practical Many-antenna Base Stations. In *Proceedings of the 18th Annual International Conference on Mobile Computing and Networking*, Mobicom '12, New York, NY, USA, 53–64. ACM.

Sinclair, G. (1950). The Transmission and Reception of Elliptically Polarized Waves. *Proceedings of the IRE*, *38*(2), 148–151.

Sohrabi, F. and Yu, W. (2016). Hybrid Digital and Analog Beamforming Design for Large-Scale Antenna Arrays. *IEEE Journal of Selected Topics in Signal Processing*, *10*(3), 501–513.

Song, H., Seo, W., and Hong, D. (2010). Compressive Feedback Based on Sparse Approximation for Multiuser MIMO Systems. *IEEE Transactions on Vehicular Technology*, *59*(2), 1017–1023.

Stratton, J. A. (1941). *Electromagnetic theory / by Julius Adams Stratton* (1st ed. ed.). McGraw-Hill New York.

Swales, S. C., Beach, M. A., Edwards, D. J., and McGeehan, J. P. (1990). The performance enhancement of multibeam adaptive base-station antennas for cellular land mobile radio systems. *IEEE Transactions on Vehicular Technology*, *39*(1), 56–67.

Swindlehurst, A. L., Ottersten, B., Roy, R., and Kailath, T. (1992). Multiple invariance ESPRIT. *IEEE Transactions on Signal Processing*, *40*(4), 867–881.

Talvitie, J., Valkama, M., Destino, G., and Wymeersch, H. (2017). Novel Algorithms for High-Accuracy Joint Position and Orientation Estimation in 5G mmWave Systems. In *2017 IEEE Globecom Workshops (GC Wkshps)*, 1–7.

Telatar, I. E. (1999). Capacity of multi-antenna Gaussian channels. *EUROPEAN TRANSACTIONS ON TELECOMMUNICATIONS*, *10*, 585–595.

the 3rd Generation Partnership Project (2015). Study on 3D channel model for LTE. Tech. rep., Sophia Antipolis. 3GPP TR 36.873 V12.2.0.

Theofilakos, P. and Kanatas, A. G. (2006). Reduced Hardware Complexity Receive Antenna Subarray Formation for MIMO Systems Based on Frobenius Norm Criterion. In *2006 3rd International Symposium on Wireless Communication Systems*, 262–266.

Troje, N. F. (2002). Decomposing biological motion: A framework for analysis and synthesis of human gait patterns. *Journal of vision*, *2*(5), 2–2.

Tse, D. and Vishwanath, P. (2005). *Fundamentals of Wireless Communication*. Cambridge University Press.

Vasisht, D., Kumar, S., and Katabi, D. (2015). Sub-Nanosecond Time of Flight on Commercial Wi-Fi Cards. *SIGCOMM Comput. Commun. Rev.*, *45*(4), 121–122.

Vasisht, D., Kumar, S., Rahul, H., and Katabi, D. (2016). Eliminating Channel Feedback in Next-Generation Cellular Networks. In *Proceedings of the 2016 Conference on ACM SIGCOMM 2016 Conference*, SIGCOMM '16, New York, NY, USA, 398–411. ACM.

Veen, B. D. V. and Buckley, K. M. (1988). Beamforming: a versatile approach to spatial filtering. *IEEE ASSP Magazine*, *5*(2), 4–24.

Venkatesan, S. and Valenzuela, R. A. (2016). OFDM for 5G: Cyclic prefix versus zero postfix, and filtering versus windowing. In *2016 IEEE International Conference on Communications (ICC)*, 1–5.

Vieira, J., Malkowsky, S., Nieman, K., Miers, Z., Kundargi, N., Liu, L., Wong, I., Öwall, V., Edfors, O., and Tufvesson, F. (2014). A flexible 100-antenna testbed for Massive MIMO. In *2014 IEEE Globecom Workshops (GC Wkshps)*, 287–293.

Vieira, J., Rusek, F., Edfors, O., Malkowsky, S., Liu, L., and Tufvesson, F. (2017). Reciprocity Calibration for Massive MIMO: Proposal, Modeling, and Validation. *IEEE Transactions on Wireless Communications*, *16*(5), 3042–3056.

Welch, P. (1967). The use of fast Fourier transform for the estimation of power spectra: A method based on time averaging over short, modified periodograms. *IEEE Transactions on Audio and Electroacoustics*, *15*(2), 70–73.

Wikipedia contributors (2019a). List of multiple Olympic medalists — Wikipedia, The Free Encyclopedia. `https://en.wikipedia.org/w/index.php?title=List_of_multiple_Olympic_medalists&oldid=878792632`. [Online; accessed 21-January-2019].

Wikipedia contributors (2019b). LTE frequency bands — Wikipedia, The Free Encyclopedia. `https://en.wikipedia.org/w/index.php?title=LTE_frequency_bands&oldid=877941518`. [Online; accessed 12-January-2019].

Witrisal, K., Meissner, P., Leitinger, E., Shen, Y., Gustafson, C., Tufvesson, F., Haneda, K., Dardari, D., Molisch, A. F., Conti, A., and Win, M. Z. (2016). High-Accuracy Localization for Assisted Living: 5G systems will turn multipath channels from foe to friend. *IEEE Signal Processing Magazine*, *33*(2), 59–70.

Wong, I. C. and Evans, B. L. (2005). Joint channel estimation and prediction for OFDM systems. In *GLOBECOM '05. IEEE Global Telecommunications Conference, 2005.*, Volume 4, 5 pp.–2259.

Wyvill, G. and Trotman, A. (1990). Ray-Tracing Soft Objects. In T.-S. Chua and T. L. Kunii (Eds.), *CG International '90*, Tokyo, 469–476. Springer Japan.

Wyvill, G. and Trotman, A. (1992). Exact Ray Tracing of CSG Models by Preserving Boundary Information. In T. L. Kunii (Ed.), *Visual Computing*, Tokyo, 411–428. Springer Japan.

Yang, H. and Marzetta, T. L. (2013). Total energy efficiency of cellular large scale antenna system multiple access mobile networks. In *2013 IEEE Online Conference on Green Communications (OnlineGreenComm)*, 27–32.

Yang, L., Chen, Y., Li, X.-Y., Xiao, C., Li, M., and Liu, Y. (2014). Tagoram: Real-time Tracking of Mobile RFID Tags to High Precision Using COTS Devices. In

Proceedings of the 20th Annual International Conference on Mobile Computing and Networking, MobiCom '14, New York, NY, USA, 237–248. ACM.

Zaidi, A. A., Baldemair, R., Tullberg, H., Bjorkegren, H., Sundstrom, L., Medbo, J., Kilinc, C., and Silva, I. D. (2016). Waveform and Numerology to Support 5G Services and Requirements. *IEEE Communications Magazine*, *54*(11), 90–98.

Zhang, S., Harris, P., Doufexi, A., Nix, A., and Beach, M. (2016). Massive MIMO real-time channel measurements and theoretic TDD downlink throughput predictions. In *2016 IEEE 27th Annual International Symposium on Personal, Indoor, and Mobile Radio Communications (PIMRC)*, 1–6.

Zhou, S. and Giannakis, G. B. (2004). How accurate channel prediction needs to be for transmit-beamforming with adaptive modulation over Rayleigh MIMO channels? *IEEE Transactions on Wireless Communications*, *3*(4), 1285–1294.

Zhou, Z., Gao, X., Fang, J., and Chen, Z. (2015). Spherical Wave Channel and Analysis for Large Linear Array in LoS Conditions. In *2015 IEEE Globecom Workshops (GC Wkshps)*, 1–6.